Impact Ionisation in Wide Band-Gap III-V Quaternary Alloys

Harry Ian James Lewis

A thesis submitted for the degree of Doctor of Philosophy

Department of Electronic and Electrical Engineering

The University of Sheffield

September 2022

“If the fool would persist in his folly he would become wise.”

William Blake

Contents

Acknowledgements

I would firstly like to thank my supervisor, Professor John David, for his help and support throughout the duration of the project and for countless technical discussions. I would like to thank Dr James Green, not only for providing me with the opportunity to undertake the degree and for his supervision during the initial stages of the project, but for continuing to provide support and to answer endless tiresome questions long after his obligations had expired. I would like to thank the Engineering and Physical Sciences Research Council for funding this work and the technical and administrative staff of the EEE department for their support.

Thanks are due to my colleagues in the impact ionisation group, and elsewhere in the EEE department, for their support and training and for making the lab and the department a pleasant place to work. In particular I would like to express my gratitude to Xiao Jin for his friendship throughout the project, and for many fruitful discussions.

I would like to thank Dr Seunghyun Lee and my other co-authors at the Ohio State University, who provided the wafers reported in chapter 5, and who warmly hosted us when we visited Ohio. I would like to acknowledge Dr Liang Qiao, whose work was preliminary to that in chapter 4, and who made time for discussions of excess noise measurement. I would also like to acknowledge Dr Jeng Shiuh Cheong and Professor Beng Koon Ng for the code used in the modelling parts of this work. Thanks to Dr Baloai Liang for providing the wafers measured in chapter 6, and to Dr Aina Baharuddin and Dr Shiyu Xie for device fabrication.

I would like to thank my schoolteachers, in particular Dr Ransford Agyare-Kwabi, without whose influence my life would likely have taken an entirely different course.

I would, of course, like to thank my parents, my brother, and my grandparents, without whom I never could have begun.

Lastly, a great deal of thanks is due to my friends. The names of the people whose friendship and support have been invaluable to me are too many to list here – you know who you are, or at least I certainly hope you do. Without you all I would be entirely lost, and I only hope that I am able to give something back.

Abstract

This work is concerned with the investigation of the characteristics of two III-V quaternary alloy systems, $(Al_xGa_{1-x})_{0.52}In_{0.48}P$ and $Al_xGa_{1-x}As_{0.56}Sb_{0.44}$. These materials are studied primarily for their application as multiplication regions in SACM avalanche photodiodes for the detection of SWIR wavelengths.

The impact ionisation coefficients of $(Al_xGa_{1-x})_{0.52}In_{0.48}P$ have been extracted from multiplication and excess noise data for 7 PIN structures of different aluminium concentrations across the full composition range from $x = 0$ to $x = 1$. These coefficients are compared with those for the ternary alloy $Al_xGa_{1-x}As$, which change similarly with variations in alloy composition. Both alloys show a sharp reduction in hole-initiated impact ionisation at a similar threshold of aluminium content around $x = 0.65$, without a similar change in electron-initiated ionisation. This indicates that the advantages associated with a wide α/β ratio can be maintained in these alloys with a significant reduction in aluminium content. Possible mechanisms for the changes in the impact ionisation coefficients with alloy composition are discussed in terms of the material band-structures. It is suggested that the suppression of hole impact ionisation may be due to the Γ band-gap becoming sufficiently large that ionisation events scattering into the Γ valley do not generally occur.

$Al_{0.85}Ga_{0.15}As_{0.56}Sb_{0.44}$ PIN and NIP structures of various thicknesses have been studied in detail, with the objective of providing a comprehensive picture of the impact ionisation characteristics of this alloy. Multiplication and excess noise have been measured under a range of carrier injection conditions. Variations in excess noise factor and bandwidth between structures of different thicknesses are discussed, and impact ionisation coefficients have been extracted which agree with multiplication data for 10 different structures across a wide electric field range. Excess noise in this alloy is found to decrease with increasing structure thickness, and the measured noise characteristics are found not to agree with those predicted by local or RPL models for the extracted ionisation coefficients.

Complementary 1500nm PIN and NIP structures of $Al_{0.75}Ga_{0.25}As_{0.56}Sb_{0.44}$ and $Al_{0.55}Ga_{0.45}As_{0.56}Sb_{0.44}$ have been studied, in order to understand how the characteristics of the $Al_xGa_{1-x}As_{0.56}Sb_{0.44}$ system vary with alloy composition. Multiplication and excess noise data have been measured under a range of injection conditions, and these are compared with the reported data for the higher-aluminium compounds of the alloy system. Preliminary impact ionisation coefficients have also been extracted for these alloys from the multiplication data, and the variation of these coefficients with alloy composition is compared to that in $(Al_xGa_{1-x})_{0.52}In_{0.48}P$ and $Al_xGa_{1-x}As$. These results indicate that excess noise in the

$Al_xGa_{1-x}As_{0.56}Sb_{0.44}$ alloy system increases as aluminium content decreases, but the measured noise for each alloy is lower than that which would be expected given their respective α/β ratios. Possible sources of error in excess noise measurement are also discussed. The mechanisms considered include device series resistance, improper or insufficiently frequent setup calibration, and inaccurate determination of primary photocurrent. Example data are given to show how these factors may distort measured excess noise factor, particularly in the case of low-noise alloys for which it is desirable to measure this parameter to a high degree of accuracy.

List of publications

Journal papers

[1] Xiao Jin, Shiyu Xie, Baolai Liang, Xin Yi, **Harry I. J. Lewis**, Leh W. Lim, Yifan Liu, Beng Koon Ng, Diana L. Huffaker, Chee Hing Tan, Duu Sheng Ong, and John P. R. David, "Temperature Dependence of the Impact Ionization Coefficients in AlAsSb Lattice Matched to InP," *IEEE Journal of Selected Topics in Quantum Electronics*, vol. 28, no. 2, July 2021.

[2] **Harry I. J. Lewis**, Liang Qiao, Jeng Shiuh Cheong, Aina N. A. P. Baharuddin, Andrey B. Krysa, Beng Koon Ng, James E. Green, and John P. R. David, "Impact Ionization Coefficients in $(Al_xGa_{1-x})_{0.52}In_{0.48}P$ and $Al_xGa_{1-x}As$ Lattice-Matched to GaAs," *IEEE Transactions on Electron Devices,* vol. 68, no. 8, August 2021.

[3] Bingtian Guo, Xiao Jin, Seunghyun Lee, Sheikh Z. Ahmed, Andrew H. Jones, Xingjun Xue, Baolai Liang, **Harry I. J. Lewis**, Sri H. Kodati, Dekang Chen, Theodore J. Ronningen, Christoph H. Grein, Avik W. Ghosh, Sanjay Krishna, John P. R. David, and Joe C. Campbell, "Impact ionization coefficients of digital alloy and random alloy $Al_{0.85}Ga_{0.15}As_{0.56}Sb_{0.44}$ in a wide electric field range," *Journal of Lightwave Technology*, vol. 40 no. 14, April 2022.

[4] Seunghun Lee, Xiao Jin, Hyemin Jung, **Harry I. J. Lewis**, Yifan Liu, Bingtian Guo, Sri Harsha Kodati, Mariah Schwartz, Christopher H. Grein, Theodore J. Ronningen, John P. R. David, Joe. C. Campbell, and Sanjay Krishna, "High Gain, Low Noise, Room Temperature 1550 nm GaAsSb/AGaAsSb Avalanche Photodiodes," *Optica,* vol. 40, no. 2, January 2023.

Conference papers

[1] Xiao Jin, Shiyu Xie, Baolai Liang, Xin Yi, **Harry I. J. Lewis**, Leh W. Lim, Yifan Liu, Beng Koon Ng, Diana L. Huffaker, Chee Hing Tan, Duu Sheng Ong, and John P. R. David, "Comparison of the temperature dependence of impact ionization coefficients in AlAsSb, InAlAs, and InP," *Proceedings of SPIE 11997, Optical Components and Materials XIX, 119970B*, March 2022.

[2] Xiao Jin, Bingtian Guo, **Harry I. J. Lewis**, Seunghyun Lee, Baolai Liang, Sanjay Krishna, Joe Campbell, and John David, "Excess noise measurements in $Al_{0.85}Ga_{0.15}As_{0.56}Sb_{0.44}$ avalanche photodiodes," *Proceedings of SPIE 12139, Optical Sensing and Detection VII, 1213907*, May 2022.

[3] John P. R. David, Xiao Jin, **Harry I. J. Lewis**, Bingtian Guo, Seunghyun Lee, Hyemin Jung, Sri Harsha Kodati, Baolai Liang, Sanjay Krishna, Joe C. Campbell, "Avalanche multiplication and excess noise characteristics in antimony-based avalanche photodiodes," *Proceedings of SPIE 12274, Emerging Imaging and Sensing Technologies for Security and Defence VII, 122740A*, December 2022.

Conference presentations

[1] **Harry I. J. Lewis**, Xiao Jin, Bingtian Guo, Seunghyun Lee, Hyemin Jung, Sri Harsha Kodati, Baolai Liang, Sanjay Krishna, Joe C. Campbell, and John P. R. David, "Excess noise measurements and impact ionization coefficients in $Al_{0.85}Ga_{0.15}As_{0.44}Sb_{0.56}$ avalanche photodiodes." *Electronic Materials Conference,* Columbus, OH, United States, June 2022.

[2] **Harry I. J. Lewis**, Liang Qiao, Jeng Shiuh Cheong, Aina N.A.P. Baharuddin, Andrey B. Krysa, Beng Koon Ng, Xiao Jin, James E. Green, and John P. R. David, "Variation in Impact Ionisation Coefficients with Alloy Composition in Aluminium-Gallium Containing III-V Compounds," *UK Semiconductors Conference,* Sheffield, United Kingdom, July 2022.

[3] John P. R. David, Xiao Jin, Bingtian Guo, Seunghyun Lee, **Harry I. J. Lewis**, Hyemin Jung, Sri Harsha Kodati, Baolai Liang, Sanjay Krishna, and Joe C. Campbell, "Avalanche Multiplication and Excess Noise Characteristics in Antimony Based Avalanche Photodiodes," *SPIE Sensors + Imaging,* Berlin, Germany, September 2022.

[4] Seunghyun Lee, Hyemin Jung, Xiao Jin, **Harry I. J. Lewis**, John P. R. David, and Sanjay Krishna, "MBE growth optimization of thick random alloy $Al_{0.85}Ga_{0.15}AsSb$ avalanche photodiodes on InP," *International Conference on Molecular Beam Epitaxy,* Sheffield, United Kingdom, September 2022.

[5] John P. R. David, Xiao Jin, **Harry I. J. Lewis,** "High performance antimony-based avalanche photodiodes (APDs) for sensing applications," *10th NATO Military Sensing Symposium,* London, United Kingdom, April 2023.

In preparation for publication

[1] **Harry I. J. Lewis**, Xiao Jin, Bingtian Guo, Seunghyun Lee, Hyemin Jung, Sri Harsha Kodati, Baolai Liang, Sanjay Krishna, Duu Sheng Ong, Joe C. Campbell and John P. R. David, "Anomalous excess noise behaviour in thick $Al_{0.85}Ga_{0.15}As_{0.56}Sb_{0.44}$ avalanche photodiodes," under review at *Scientific Reports* as of April 2023.

[2] **Harry I. J. Lewis**, Xiao Jin, Shiyu Xie, Baolai Liang, Xin Yi, Diana L. Huffaker, Manoj Kesaria, Gerald Buller, and John P. R. David, "Avalanche Multiplication and Excess Noise in $Al_{0.75}Ga_{0.25}As_{0.56}Sb_{0.44}$ and $Al_{0.55}Ga_{0.45}As_{0.56}Sb_{0.44}$ Avalanche Photodiodes"

Chapter 1: Introduction

1.1 Overview

The primary objective of this work is to investigate the impact ionisation properties of wide band-gap III-V alloys that can be combined with narrow band-gap absorbers to produce fast, high sensitivity, low noise avalanche photodiodes for short-wave infrared detection. There is a need for such detectors for use in LiDAR systems and for both fibre-optic and free-space optical communications.

This thesis is concerned with the characteristics of two wide band-gap III-V semiconductor alloys systems, $(Al_xGa_{1-x})_{0.52}In_{0.48}P$ and $Al_xGa_{1-x}As_{0.56}Sb_{0.44}$. These alloys have the advantages of being lattice-matched to GaAs and InP, respectively, which allows them to be combined with narrow band-gap absorption materials that can be grown on these substrates. Various alloy compositions have been studied in this work and the variations in behaviour with changing ratios of aluminium and gallium are reported on. Of key interest are the electron and hole impact ionisation coefficients, and the ratio between them, which is closely related to the performance metrics of excess noise factor and bandwidth. As well as avalanche photodiodes, $(Al_xGa_{1-x})_{0.52}In_{0.48}P$ is used in a variety of other applications such as in LEDs and photovoltaic cells. Knowledge of the impact ionisation characteristics of this alloy is therefore useful in order to prevent avalanche breakdown as a failure mechanism in these devices.

Understanding the changes in impact ionisation behaviour with variations in alloy composition is also useful from a more fundamental perspective, and may inform the development of new materials with optimal characteristics for avalanche multiplication.

This chapter presents the structure of the thesis and a brief discussion of the photoelectric effect and various electro-optical detectors, moving on to the principle of operation of APDs, their applications, and the limitations of current technology.

1.2 Organisation of the thesis

This chapter describes a basic overview of the motivations for the work presented in this thesis, including the applications of APDs, the need for improved technology, and means by which this can be achieved using new materials and device designs.

Chapter 2 describes the theory of photodetection technology and impact ionisation, including more detailed discussions of the processes of avalanche gain and excess noise. It also describes mathematical and computational models that can be used to predict multiplication and excess noise factor if material and device parameters are known.

Chapter 3 describes the techniques and methods used to fabricate and characterise the devices examined in this work and includes a discussion of possible sources of error in the measurement of excess noise.

Chapter 4 is an analysis of the impact ionisation characteristics of the quaternary alloy system $(Al_xGa_{1-x})_{0.52}In_{0.48}P$, reporting impact ionisation coefficients based on multiplication and excess noise data for PIN structures of seven different compositions from $x = 0$ to $x = 1$. The variations in the impact ionisation coefficients with alloy composition are discussed and compared with those of $Al_xGa_{1-x}As$.

Chapters 5 and 6 are analyses of specific alloys within the $Al_xGa_{1-x}As_{0.56}Sb_{0.44}$ quaternary system. Chapter 5 presents multiplication and excess noise measurements for various PIN and NIP structures of the alloy $Al_{0.85}Ga_{0.15}As_{0.56}Sb_{0.44}$. This chapter discusses how the noise, multiplication, and bandwidth characteristics vary between these structures, comparing between material grown as a digital and as a random alloy and between devices of different thicknesses. Impact ionisation coefficients for this alloy have also been extracted from the multiplication data.

Chapter 6 presents multiplication and excess noise data for PIN and NIP structures of the alloys $Al_{0.75}Ga_{0.25}As_{0.56}Sb_{0.44}$ and $Al_{0.55}Ga_{0.45}As_{0.56}Sb_{0.44}$. Impact ionisation coefficients for these alloys have been extracted from the multiplication data, and these are compared with those for $AlAs_{0.56}Sb_{0.44}$ and $Al_{0.85}Ga_{0.15}As_{0.56}Sb_{0.44}$ to provide a broader picture of how the characteristics of the $Al_xGa_{1-x}As_{0.56}Sb_{0.44}$ system change with alloy composition.

Chapter 7 provides a summary of the work and suggestions for further research.

1.3 The photoelectric effect

By the end of the 19th century, physicists had not been able to assemble a complete theory accounting for the emission and absorption of light. Maxwell's wave theory of light had been wholly accepted by the scientific community, but certain experimental observations were inconsistent with the representation of electromagnetic waves as continuous phenomena. One specific problem was the calculation of the energy distribution of radiation produced by a black body. Classical theory implies a limitless increase in the energy of black body emission as frequency increases, which contradicts experimental results. This was reconciled in 1900 by Max Planck, who proposed that electromagnetic energy was not continuous but in fact consisted of discrete quanta. The energy of a quantum is related to its frequency by equation 1.1:

$$E = hv \qquad (1.1)$$

Where h is Planck's constant and v is frequency.

Planck's ideas were further developed by Albert Einstein. The photoelectric effect was first documented by Einstein in 1905, and it was primarily for this work that he received his 1921 Nobel Prize. The experimental setup that was used to demonstrate the photoelectric effect consists of two metal surfaces held in high vacuum, acting as electrodes. Light incident on the cathode produces free electrons that travel to and are collected on the anode, referred to as cathode rays. Observations from this experiment led Einstein to postulate that each individual quantum of electromagnetic energy, or photon, is absorbed by a single electron in the cathode metal. This allows the electron to escape from its bound state in the metal, and any surplus of energy in the photon is acquired by the electron as kinetic energy. The transfer of energy is related by equation 1.2:

$$hv = E_k + W_0 \ (1.2)$$

Where E_k is the kinetic energy of the cathode ray and W_0 is the work function of the metal, which is the minimum energy required to free an electron from its bound state.

If a sufficient voltage is applied across the electrodes then the electrons will not travel to the anode, but will instead cluster around the cathode. This voltage, referred to as the stopping potential, can be treated as a measure of the energy of the cathode rays, as given in equation 1.3:

$$qV = E_k \ (1.3)$$

Where q is the electronic charge. This can be combined with equation 1.2 to give equation 1.4**:**

$$V = (h/e)v - W_0/q \quad (1.4)$$

It is found that stopping potential is related linearly to the frequency of incident light, with a constant of proportionality of *h/e*. It is also observed that current flows instantaneously when light is incident on the cathode and is directly proportional to its intensity, provided that the frequency of the light is greater than a particular frequency which is characteristic to each metal.

These observations support the theory that the absorption of energy from electromagnetic radiation occurs instantaneously and of a fixed quantity, rather than continuously over time. If the energy of each photon is less than W_0 then no photoelectric current will flow regardless of the intensity of the light source or the time for which it is incident on the cathode, as opposed to a case by which electrons could accumulate energy over time until they could escape the bound state.

1.4 Electro-optical detectors

1.4.1 Photomultiplier tubes

Knowledge of the photoelectric effect permitted the development of the photomultiplier tube (PMT), the primary device for detecting weak light signals prior to the advent of solid-state technology for optical detection. A PMT consists of a vacuum tube containing a photosensitive cathode, a series of several dynodes, and an anode. Photons incident on the cathode will produce electrons due to the photoelectric effect. Electrons will travel to the first of the dynodes, which consist of a metal coated in a secondary emission material. Electrons absorbed by the dynode will lead to the emission of more electrons, with a gain of the order of 10 to 100. A series of dynodes in a circular cage configuration can produce gains of up to 10^7. After multiplication by the dynodes, electrons will arrive at the anode and flow as current. PMTs were the first devices capable of single photon detection and are still generally preferred over semiconductor photodiodes in some photon-starved applications due to their very high gain and low noise. Their disadvantages are high operating voltages (often in excess of 1kV), low quantum efficiencies, and bulk compared to solid-state alternatives.

1.4.2 Photoconductors

A photoconductor consists solely of a piece of semiconductor with ohmic contacts. The conductivity of the semiconductor increases in the presence of light due to the photoelectric effect. If a DC current is passed through the device, the voltage generated will vary depending on the intensity of an incident light signal. Mercury Cadmium Telluride photoconductors are available for wavelengths up to 22μm

[1]. These devices are highly sensitive but limited by high noise and low bandwidth. Cryogenic cooling can reduce noise significantly, but this adds additional system complexity and cost.

1.4.3 Phototransistors

A phototransistor operates similarly to a bipolar junction transistor (BJT) with an optically generated base current, which is multiplied by the h_{FE} of the transistor. Phototransistors are inexpensive but suffer from non-linear response characteristics, high dark currents and slow switching speeds.

1.4.4 Photodiodes

Solid-state photodiodes have superseded vacuum technology in most applications due to their low cost, small size, ruggedness and high quantum efficiencies. A photodiode consists of p^+ doped, nominally intrinsic, and n^+ doped regions of semiconductor grown on an appropriate substrate. The thickness of the intrinsic region can be varied for different device specifications, with a thicker region yielding higher sensitivity but an increased carrier transit time, as well as a higher operating voltage. Photodiodes are operated under reverse bias such that the intrinsic region is fully depleted and maintains a fairly uniform electric field, which is high enough to maintain the saturated carrier drift velocity but not high enough for impact ionisation to occur. Carriers that are optically generated in the intrinsic region will be swept to the cladding regions by the electric field, generating a current. Minority carriers that are generated in the cladding regions may also contribute to the current, but they must first diffuse into the high-field region to be collected by the electric field. Three-region structures are designated as PIN or NIP structures depending on the order of growth of the layers. PIN structures are grown with the n^+ cladding as the ‘bottom’ cladding region, closest to the substrate, and the p^+ cladding region at the top of the device. NIP structures are opposite, with the p^+ cladding at the bottom and the n^+ cladding at the top. The difference between these structure types is important for device characterisation because incident light will, in most cases, reach the top cladding layer first. This means that high-energy light will be absorbed entirely, or almost entirely, in the top cladding. A schematic diagram showing the electric field profile of a standard PIN photodiode is shown in figure 1.1.

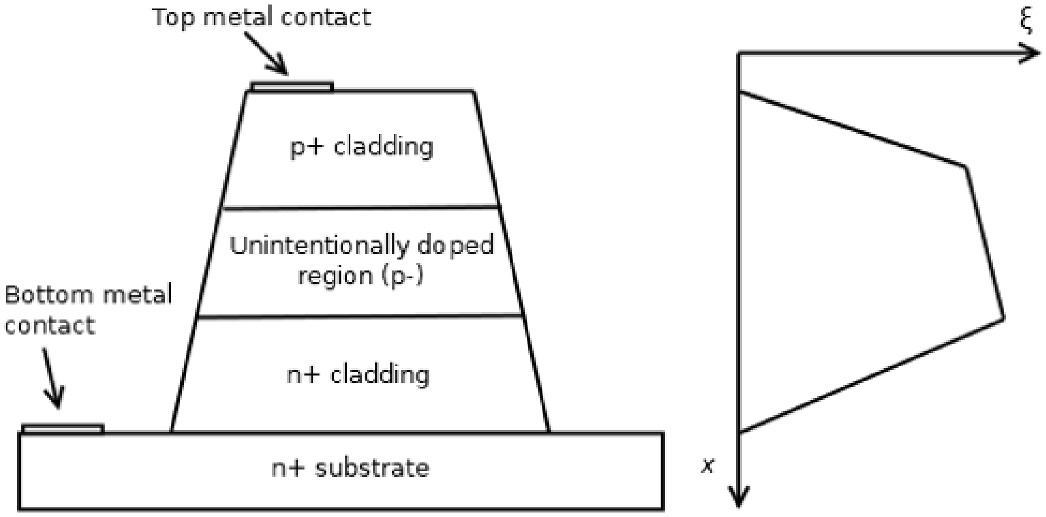

Figure 1.1: Diagram showing the structure of a standard PIN mesa diode, with *p*-type background doping, and a typical electric field profile.

1.5 Avalanche photodiodes

1.5.1 Introduction to avalanche photodiodes

If a photodiode is reverse biased with a voltage such that a sufficiently high electric field is elicited, impact ionisation will occur and carriers will be multiplied by an avalanche gain effect. The mechanism of this process is described in section 2.3. A photodiode that is biased with the intention of operating in this regime is known as an avalanche photodiode (APD).

APDs find use in a diverse range of applications including optical communications, LiDAR, astronomy, and medical and other imaging across the UV, visible, and infrared wavelength ranges. The central characteristic of an APD is its internal gain, which is produced by applying a sufficiently high electric field across the device that carriers are generated by impact ionisation. In optoelectronic systems designed to detect weak optical signals, some form of amplification is likely be required. At low bandwidths, this can be achieved straightforwardly using electronic amplification circuitry, but for high-speed applications, the noise associated with this circuitry will be significant. A receiver system can achieve higher signal to noise ratio (SNR) by incorporating an APD. This is illustrated by equations 1.5 and 1.6, which give the SNR for a receiver system utilising a preamplifier and, respectively, a non-multiplying photodiode and an APD:

$$\mathrm{SNR} = \frac{P_S}{N_S + N_e} \quad (1.5)$$

$$\mathrm{SNR} = \frac{P_S}{FN_S + N_e/M^2} \quad (1.6)$$

Where P_s is the signal power, N_s is the shot noise power in the photodiode or APD at unity gain, N_e is the noise due to the preamplifier circuitry, F is the excess noise factor of the APD, and M is the multiplication factor of the APD. In high-frequency circuitry N_e will significantly outweigh N_s and is the main limiting factor for SNR. In the second case, operating the APD at high gain values increases the SNR significantly. However, the F term – excess noise factor – increases with multiplication and will ultimately limit the useful gain of the APD [2]. As is discussed in detail in chapter 2, the most significant factor in determining F in an APD is generally the disparity between the rates of impact ionisation of electrons and holes. These rates are quantified as the impact ionisation coefficients – denoted by α for electrons and β for holes – and are properties of the semiconductor material. Identifying materials in which $\alpha >> \beta$ (or $\beta >> \alpha$) is an area of significant research interest and a key objective of this work. Excess noise factor is often quantified by comparison to the noise predicted by McIntyre's local noise model for a given β/α (α/β) ratio, with a figure of merit referred to as k. The denominator is the ionisation coefficient for the more readily ionising carrier type, and a smaller k indicates better noise performance. This model is described in section 2.7. As bias voltage is increased the multiplication factor of an APD will increase asymptotically, and the voltage at which it tends towards infinity is referred to as the avalanche breakdown voltage, V_{bd}. APDs are operated at bias voltages close to V_{bd} to maximise gain. This type of operation, in which an incident optical signal is multiplied to provide a proportional continuous electrical output, is referred to as *linear mode* operation.

APDs may also be operated in *geiger mode,* as single photon avalanche detectors (SPADs). Single photon detection has a wide range of applications including fundamental research [3], quantum key distribution [4], spectroscopy [5], and astronomy [6]. They are also applicable in similar domains as linear APDs, such as free-space optical communications [7] and ranging [8]. The device is biased above its breakdown voltage such that a single incident photon can trigger an avalanche breakdown event. Unlike a linear mode device, which generate a response proportional to the incident optical signal, breakdown events will be indistinguishable from each other regardless of the amplitude of the triggering signal. The switching speed of a SPAD can be improved by quenching. A resistor is used to produce a voltage which under-biases the device in response to the breakdown current. This will be limited by the RC time constant of the resistor and the capacitance of the SPAD device junction, and more complex circuitry may be employed for faster quenching.

SPADs will be subject to dark counts, which are breakdown events triggered by non-optically generated carriers. Their dark current rate per unit of device area is several orders of magnitude greater than for PMTs, which necessitates small device area, but solid-state SPADs are significantly cheaper and can more easily be made mechanically robust.

1.5.2 SAM-APD Structures

SAM-APDs incorporate a heterojunction between the absorption and multiplication regions, which allows an “absorption” material that absorbs at desired wavelengths to be combined with a different “multiplication” material that exhibits low dark currents, high avalanche gain and low noise. This configuration will often involve a narrow band-gap absorber combined with a wider band-gap multiplier of a material which is known to have characteristics advantageous to avalanche multiplication. It is necessary to maintain a high electric field in the multiplication region while maintaining a sufficiently low field to avoid high dark currents and band-to-band tunnelling in narrow band-gap absorbers. This may be achieved by increasing the thickness of the multiplication region, decreasing the overall electric field in the device. Alternatively, and generally preferably, a charge region may be incorporated between the absorption and multiplication regions (in which case the structure is denoted as SACM) to grade the electric field between the absorption and multiplication regions. Precise control of the doping in the charge region is necessary to maintain the desired electric fields in the multiplication and absorption regions. A SAM structure will have a lower breakdown voltage than a three-region structure of the same thickness because the high field is applied across a smaller proportion of the device, meaning that a given bias voltage will elicit a higher electric field. Carrier feedback effects will also be reduced due to the shorter transit time in the thinner multiplication region. Additionally, because there is a low field in the absorption region which reaches close to the optical window of the device, carrier collection and velocity will be increased because carriers do not have to diffuse into the high field region. SAM-structures may suffer from low bandwidth if the band offset between the narrow band-gap absorber and the wide band-gap multiplier is too large, resulting in charge carriers becoming trapped at the heterojunction [9], [10]. This can be mitigated by using ternary or quaternary structures in the charge region such that it is possible to gradually vary the alloy composition, and therefore the band-gap, such that the band offset between the multiplication region and the widest band-gap part of the charge region is minimised. A schematic diagram showing the electric field profile in a typical SACM structure is given in figure 1.2.

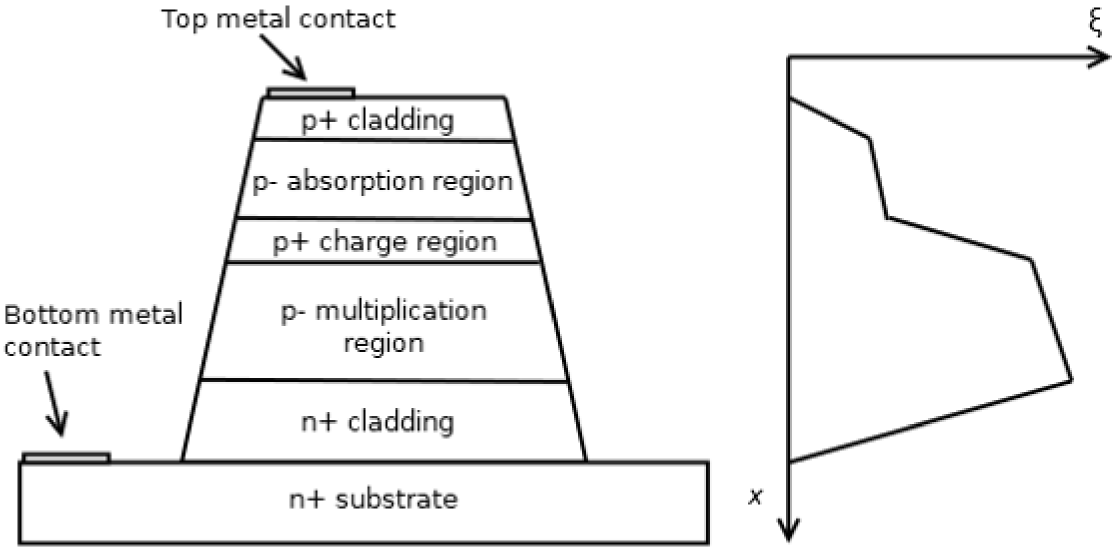

Figure 1.2: Diagram showing the structure of an SACM mesa diode and a typical electric field profile. The background doping in the absorption and multiplication regions is *p*-type.

1.5.3 Materials for APDs

1.5.3.1 Silicon

Silicon is the longstanding material of choice for detection of visible and near infrared (NIR) wavelengths due to its low cost, extremely mature technology, and low excess noise characteristics due to its very wide α/β ratio [11]. The primary limitation of silicon photodiodes is the absorption cutoff at approximately 1µm, which means that alternative absorption materials are required to detect wavelengths in the range of short-wavelength infrared (SWIR) and longer. Additionally, achieving low excess noise in silicon requires thick reach-through structures, which require high operating voltages in excess of 300V. The impact ionisation characteristics of silicon also vary significantly with temperature, making Si APDs unsuitable for high-temperature applications [12], [13]. Silicon substrates are very inexpensive - the cost of 8-inch Si wafer is up to three orders of magnitude lower than that of an equivalent GaAs wafer, the next most mature technology. Substrate wafers are also available in large sizes, which is advantageous for producing sensor arrays. These advantages have limited the uptake of III-V technologies in cases where a silicon alternative is possible.

1.5.3.2 Materials for infrared detection

Current generation APDs for short-wavelength infrared (SWIR) applications utilise germanium or $In_{0.53}Ga_{0.47}As$ (InGaAs), which can absorb up to 1605nm and 1655nm respectively [14], [15]. However, the band-gaps of these materials are too narrow to be used for avalanche multiplication without large tunnelling currents, requiring them to be combined with wider band-gap alloys in a SAM structure.

Si/Ge SAM detectors have been reported with high quantum efficiency [16], but dark currents of up to tens of μA prevail due to the lattice mismatch between the materials. Most commercial SWIR APDs consist of an InGaAs absorber combined with an InP [17] or $In_{0.52}Al_{0.48}As$ (InAlAs) multiplication region, grown on an InP substrate. InP, which was the first material utilised in SAM structures with InGaAs and is still the material found in most commercial devices, has very similar electron and hole impact ionisation coefficients [18]. This results in high excess noise, which limits the useful gain of a device. The lowest excess noise factor reported for InGaAs/InP SAM-APD structures is equivalent to a k of 0.3 to 0.4, using thin multiplication regions to take advantage of the effects of the carrier dead space [19]. Improvements on this technology have been made by replacing InP with InAlAs [20], and InGaAs/InAlAs SAM-APDs have been reported with excess noise factors equivalent to k values of 0.12-0.2 and a gain-bandwidth product of up to 320GHz [21], [22]. There is evidence that the excess noise factor of InAlAs APDs may be reduced further by utilising digital alloy superlattice structures [23], [24].

More advanced materials for IR APDs include the ternary alloy $Hg_{x-1}Cd_xTe$. Most research on this alloy system is concentrated on $Hg_{0.7}Cd_{0.3}Te$, which has a cutoff wavelength of 4.3μm and shows extremely low excess noise, lower than that expected for a k of zero. This results from aspects of the bandstructure which result in hole impact ionisation becoming negligible – devices exhibiting this behaviour are referred to as electron-APDs (e-APDs) [1], [25]. $Hg_{x-1}Cd_xTe$ is difficult to grow and process, however, and its narrow band-gap (0.25eV) means that it must be cooled cryogenically in order to reduce dark currents. Mercury also causes damage to human and environmental health, and it is desirable to discontinue its use in new products [26]. Another material that demonstrates e-APD properties is the binary III-V alloy InAs, which absorbs up to 3.5μm [27]. This alloy is of significant interest due to the ready availability and relative ease of growth of III-V materials, though InAs substrates remain costly. InAs APDs demonstrate extremely high gain and low excess noise [27], equivalent to a k of zero, but are limited by high dark currents. Bulk dark currents must be reduced by cooling, and surface dark currents remain problematic even at low temperatures. Recent research has shown that it may be possible to mitigate surface dark currents using device planarisation [28], but it is unlikely that InAs APDs will become feasible for room-temperature use.

There has recently been significant research interest in antimonide III-V alloys for avalanche multiplication [29]. $Al_xIn_{1-x}As_ySb_{1-y}$ devices grown on GaSb substrates can absorb at a range of wavelengths from 1-5μm, depending on alloy composition [30]. $Al_{0.7}In_{0.3}As_{0.3}Sb_{0.7}$ PIN diodes display extremely low excess noise, equivalent to a k of approximately 0.015 [31]. The cutoff wavelength of this composition is similar to silicon, but it is possible to grade the alloy composition and combine an $Al_{0.7}In_{0.3}As_{0.3}Sb_{0.7}$ multiplier with a narrower band-gap $Al_xIn_{1-x}As_ySb_{1-y}$ alloy absorber. A device based on this principle has been reported with a cutoff wavelength of >3 µm [32]. Excess noise results were not included, but it is a reasonable assumption that they would be similarly low to those reported for the equivalent PIN structure. The disadvantage of this alloy system is the relatively high cost of GaSb substrates. This could be mitigated with improved technological maturity or by heteroepitaxy of GaSb layers on silicon substrates [33], making this a promising alloy for next-generation APDs.

$Al_{0.79}In_{0.21}As_{0.74}Sb_{0.26}$ APDs have also been grown on InP substrates, and show similarly low excess noise equivalent to a k value of 0.018 [34]. The use of InP substrates is highly desirable due their low cost and technological maturity relative to more exotic III-V materials, and the possibility of lattice-matching with absorbing materials such as InGaAs. InP substrates are also available with diameters up to 6in, which opens the possibility of large-area detector arrays. The $Al_xGa_{1-x}As_{0.56}Sb_{0.44}$ alloy system, which can also be grown on InP substrates, has recently been of considerable research interest. This initially followed studies showing an extremely wide α/β ratio and excess noise equivalent to a k value of 0.005 in a 1550nm $AlAs_{0.56}Sb_{0.44}$ PIN structure [35], [36]. Study of lower-aluminium $Al_xGa_{1-x}As_{0.56}Sb_{0.44}$ alloys is the subject of chapters 5 and 6 of this work, and a more detailed review of the literature on this alloy system is given in chapter 5. The mechanism by which the presence of antimony suppresses hole impact ionisation to such an extent is unclear. The incorporation of heavier group V atoms increases the energy of the spin-orbit split off band, from which holes generally initiate impact ionisation events in III-V alloys [37]. Increasing the energy of this band may decrease the likelihood of holes being scattered into a sufficiently energetic state to initiate impact ionisation. This effect is observed in GaAsBi, for which it has been reported that the incorporation of Bi significantly decreases β even at very low concentrations [38]. It has also been suggested that the decrease in β may be due to relatively higher effective masses for holes or due to phonon scattering that affects holes disproportionally [31]. Another possible mechanism is increased spin-orbit coupling, which may cause alloy scattering to become the dominant scattering mechanism [29].

There is also interest in GaAs-based APDs for infrared detection. GaAs substrates carry the lowest cost and highest technological maturity of an III-V material. Dilute nitrides such as GaInNAsSb can be grown on GaAs substrates and can absorb at 1.55µm [39]. Proof-of-concept structures incorporating GaAs or AlGaAs multipliers with GaSb absorbers have been reported with absorption up to 1.7µm and noise equivalent to a k of 0.2. The possible use of $(Al_xGa_{1-x})_{0.52}In_{0.48}P$ as the multiplication region for a GaAs-based SAM structure is discussed in chapter 4 of this work.

1.5.4 Applications of infrared-detecting APDs

1.5.4.1 Optical communications APDs

Optical communications have been a rapidly growing sector since the development of low-loss glass optical fibres in 1970 [40]. Optical transmission networks incorporating high-speed semiconductor laser diodes and photodiodes now account for 95-99% of internet traffic and optical communications has been highlighted as a key growth area for the UK's photonics industry. By 2035 the photonics industry in the UK is anticipated to be worth £50 billion, up from £14.5 billion in 2020, and to be one of the three most productive manufacturing sectors in the country [41]. Optical fibres are now capable of transmitting at tens of Tbit/second [42] and next generation ethernet networks will necessitate faster and more sensitive detectors, to permit fast data transfer rates and reduce the need for signal repeaters in optical communications networks. An APD for optical communications must be able to absorb at SWIR wavelengths of 1300 and 1550nm, which allow for minimal attenuation in optical fibres. The maximum possible gain-bandwidth product and low noise will be required to maximise data throughput and minimise bit error rates. Current-generation InGaAs/InP optical communications APDs are limited to around 10Gb/s [43]. There is significant demand for new APD technologies that can meet the requirements of next-generation networks operating at 100 and 400GHz.

1.5.4.2 Free-space optical communications

Free-space optical (FSO) networks can provide high-data rate communications at distances up to the kilometres range. These provide an advantage over conventional radio communications due to the wide bandwidths available and the lack of licensing requirements at optical wavelengths. FSO systems which could transmit data over tens of miles using LEDs and early lasers were developed in the 1960's [44]. These did not see widespread adoption due to the divergence of laser beams and the transmission-disrupting effects of the atmosphere, and attention moved to optical fibre communications following the development of low-loss optical fibres. However, interest in FSO communication has been maintained by military [45] and a variety of space applications, such as inter-satellite and satellite-to-ground links [46]–[48]. Space applications require very high-sensitivity detectors as they require signals to be transmitted over long distances without intermediate amplifiers [47]. Systems transmitting data over distances greater than 400000km have been demonstrated [49], [50]. More recently, FSO systems have been investigated for next-generation broadband and 5G networks, and systems transmitting at 40Gb/s have been reported [51] using a wavelength of 1550nm. IR wavelengths are desirable for both terrestrial and space FSO applications, as longer wavelengths will propagate further under vacuum conditions and will be less affected by turbulence when transmitting through the atmosphere [52]. The required optical window size for these systems is relatively large, at around 80-200μm [53]. This is due to dispersion of laser beams in the atmosphere, which results in increased spot size. Larger devices will have a reduced bandwidth due to higher capacitance, and thicker APD structures may be useful to compensate for this. In this case it would be necessary to make an appropriate compromise with the transit time-limited bandwidth, which is lower in thicker devices.

1.5.4.3 LiDAR

Another application for APDs, which is currently of great research interest, is Light Detection and Ranging (LiDAR). LiDAR works by emitting pulsed light from lasers and measuring the backscattered light to image the surrounding environment, in a similar fashion to radar [54]. Ranges are determined by time-of-flight, using photon return time and the speed of light. LiDAR systems can determine range many times more accurately than conventional radar due to the shorter wavelength of the radiation used [55]. LiDAR has the potential to be transformative across a vast range of applications, such as 3-D imaging for self-driving cars, autonomous or remotely controlled robots and drones, or structural observation. The concept was initially developed for atmospheric probing and could be used for meteorological applications such as mapping wind directions and velocities from satellites [54]–[57], and gas sensing [58]. Visible light LiDAR cameras have also been demonstrated using SPAD arrays. Systems have been reported that can produce 3-D images using approximately 1 signal photon per pixel [59], [60], resolving the image using photon time-of-flight. Current LiDAR systems commonly use wavelengths in the 850-950nm NIR range and incorporate silicon APDs as detectors. This is advantageous due to ready availability of lasers at this wavelength, and the mature technology and low excess noise of Si APDs. However, the low absorption in water means that the maximum eye-safe power at these wavelengths is relatively low. 1550nm light is readily absorbed by water in the cornea, and the eye-safe limit for optical power is 20X higher than that at 905nm [61]. It has been shown that 1550nm light is not more attenuated by fog than 905nm light, meaning that 1550nm would be preferable for use in adverse weather conditions due to the higher optical power available within a threshold of eye-safety [61]. This is desirable for applications such as environment mapping for self-driving cars, for which some exposure of the eye to the light output of the system is difficult to completely avoid. SWIR wavelengths are also subject to less attenuation by the atmosphere than NIR wavelengths [62], and lower levels of background radiation in daylight. Current generation LiDAR systems utilise high-powered lasers, which come with high cost, operating power, size, and weight. The use of lower powered lasers is therefore desirable, but this requires detectors with increased sensitivity [63].

Chapter 2: Background theory

2.1 Optical absorption in semiconductors

The energy of a photon, E, is related to its wavelength, λ, by equation 2.1, which is equivalent to equation 1.1:

$$E = \frac{hc}{\lambda} \text{ (2.1)}$$

Where c is the speed of light in a vacuum. Semiconductors can absorb photons that have an energy greater than or equal to their minimum energy band-gap. Photons with sufficient energy will be absorbed by an electron in the semiconductor crystal if there is an available state in the conduction band for the electron to occupy. This means that a higher-energy photon will be absorbed more readily as it can promote an electron to a higher-energy state in the conduction band, meaning that there are a higher number of available destination states. Conversely, photons that have energies only slightly greater than the minimum band-gap of the semiconductor can promote electrons only to the lowest states in the conduction band, meaning that they may have to travel further through the semiconductor crystal before being absorbed. If the semiconductor band-gap is direct, meaning that the maximum point of the valence energy band is aligned with the minimum point of the conduction energy band at the Γ point of the Brillouin zone, momentum is conserved in the absorption process. However, if the band-gap is not direct, a phonon interaction must occur in the absorption process in order to conserve momentum. This means that the probability of absorption across an indirect band-gap is significantly lower than across a direct band-gap.

An ideal semiconductor is transparent to photons with wavelengths lower than the minimum energy band-gap. It is possible, however, for defects or dopants to create additional energy states in the forbidden gap, which makes absorption of lower-energy photons possible [64], [65]. It is also possible for electrons to tunnel into the conduction band in the presence of an electric field, which causes the band-gap to be effectively narrowed [66], [67].

How readily light is absorbed by a semiconductor is described by the absorption coefficient, γ. This is a wavelength-dependent property of the semiconductor material and is defined as the inverse of the average distance travelled by a photon through the semiconductor crystal before being absorbed. The intensity of light travelling through a semiconductor, denoted by φ, is described by equation 2.2:

$$\frac{d\varphi}{dx} = -\gamma\varphi(x) \text{ (2.2)}$$

Where x is the distance travelled through the semiconductor. This can be solved to give equation 2.3:

$$\varphi = \varphi_0 \exp(-\gamma x) \quad (2.3)$$

Where φ_0 is the initial intensity of the light.

2.2 Quantum efficiency

The quantum efficiency of a photodiode, η, is the ratio of electron carrier pairs that flow as current to incident photons with sufficient energy to be absorbed. An ideal photodiode has a η of 1, but real device values will be significantly lower. This may be due to non-absorption of photons due to reflection at the semiconductor/air interface, or carrier recombination within the device or at the device surface. Reflection can be almost eliminated in commercially produced devices by the use of anti-reflection coatings. Surface recombination occurs immediately upon absorption of a photon at the device surface and will prevent carriers from being collected by the electric field. This may occur due to dangling bonds or other surface defects [68] and can be reduced by surface passivation [69]. Carriers may also recombine before being collected by the electric field if they are absorbed further from the edge of the high field region than the average minority carrier diffusion length. This is more likely to be the case if the incident photons have higher energy and are more readily absorbed, as they will be absorbed closer to the device surface. Higher photocurrent will therefore result from the use of longer-wavelength light, which will be more likely to be absorbed in the depletion region of the device and be immediately collected by the electric field. However, this will result in a mixed carrier injection characteristic that may reduce device performance as described in section 2.4.

2.3 Impact ionisation

If a voltage is applied to a photodiode such that it is reverse biased, an electric field will be developed. Minority carriers that are generated outside the electric field will diffuse until they are collected by it or they recombine. Carriers generated within the electric field will be collected by it immediately.

Charge carriers that are swept by the electric field can acquire sufficient kinetic energy to ionise atoms in the lattice, promoting an electron from the valence band to the conduction band to produce a free carrier pair. The primary carrier will lose energy in the process but can gain energy from the electric field again and trigger another impact ionisation event. Impact ionisation can be initiated by either an electron or a hole. Secondary carriers, those produced by impact ionisation, can also become sufficiently energised by the field to impact ionise. This means that a cascade effect occurs as carriers traverse the high-field region. By this mechanism, a small number of free charge carriers, or even a single carrier, can multiply to produce a significant current. This process is known as avalanche multiplication. The minimum energy required for impact ionisation to occur is referred to as the ionisation threshold energy, E_{th}, and is related to the minimum energy band-gap of the material, E_g. Using simple models of semiconductor band-structures, assuming parabolic bands and equal effective masses for electrons and holes, Wolff *et al.* approximated E_{th} as $1.5E_g$ [70]. An improved model was developed by Anderson and Crowell, assuming a direct band-gap, spherical constant energy surfaces and constant electron effective masses m_c^* and m_v^* for electrons in the conduction and valence bands respectively. m_c^* and m_v^* are related by a ratio γ such that $m_v^* = \gamma m_c^*$. The threshold energies for electron and hole initiated ionisation events are then given by equations 2.4 and 2.5 respectively [71].

$$E_{the} = E_g\left(\frac{2+\gamma}{1+\gamma}\right) \quad (2.4)$$

$$E_{thh} = E_g\left(\frac{1+2\gamma}{1+\gamma}\right) \quad (2.5)$$

In practice, this model does not take into account the complexities of semiconductor band-structures and the varying nature of electron and hole effective masses. The electron and hole ionisation threshold energies for a given semiconductor material may be inferred empirically from experimental data, generally using data from various different device structures of the same material [72]–[74]. The ionisation process is also complicated because phonon interactions may be required in order to conserve momentum in materials with an indirect band-gap. Phonon interactions may also impede impact ionisation by reducing the energy of carriers, preventing them from acquiring sufficient kinetic energy to impact ionise.

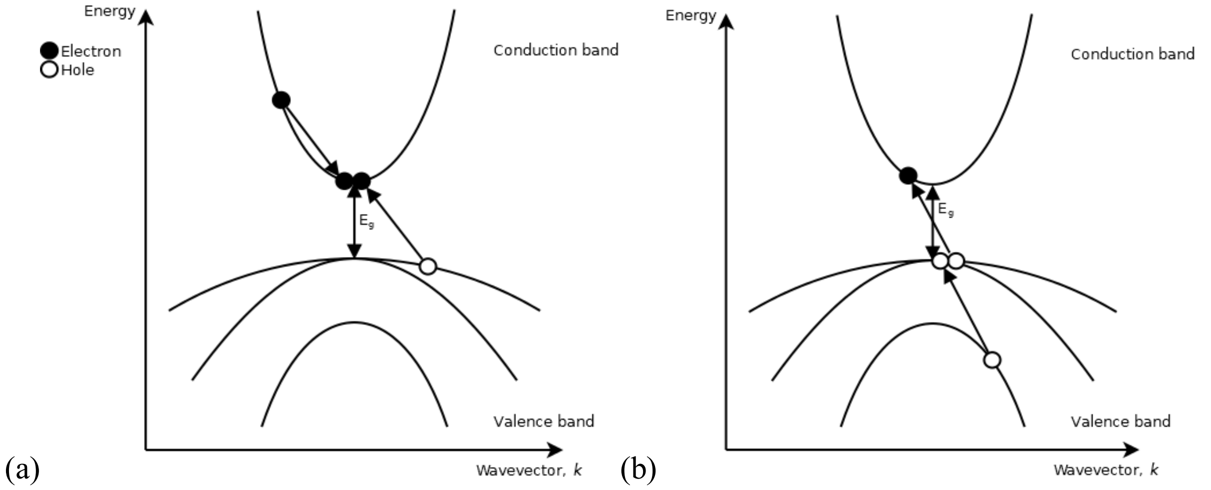

Figure 2.1: Energy-wavevector diagrams showing (a) electron and (b) hole initiated impact ionisation events.

The probability of impact ionisation events is characterised by quantities known as the electron and hole impact ionisation coefficients (also referred to as ionisation coefficients), denoted by α and β for electrons and holes respectively. These are defined as the reciprocal of the mean distance that a carrier will travel between ionisation events, and are a function of electric field at a given temperature. If α and β are similar, then carriers of both types will be similarly likely to initiate ionisation events. If $\alpha >> \beta$ or $\beta >> \alpha$, ionisation events initiated by the more readily ionising carrier type will dominate. This causes the multiplication process to be more deterministic. Band diagrams showing electron and hole initiated impact ionisation events are shown in figure 2.1, and schematic diagrams showing impact ionisation are shown in figures 2.2 and 2.3. Figure 2.2 shows impact ionisation in a material where α and β are similar, and carrier feedback is significant. Figure 2.3 shows a hypothetical example where β tends to zero, and therefore no hole-initiated impact ionisation events occur. α and β tend to converge as electric field increases, meaning that thicker structures will generally display more disparate α/β ratios.

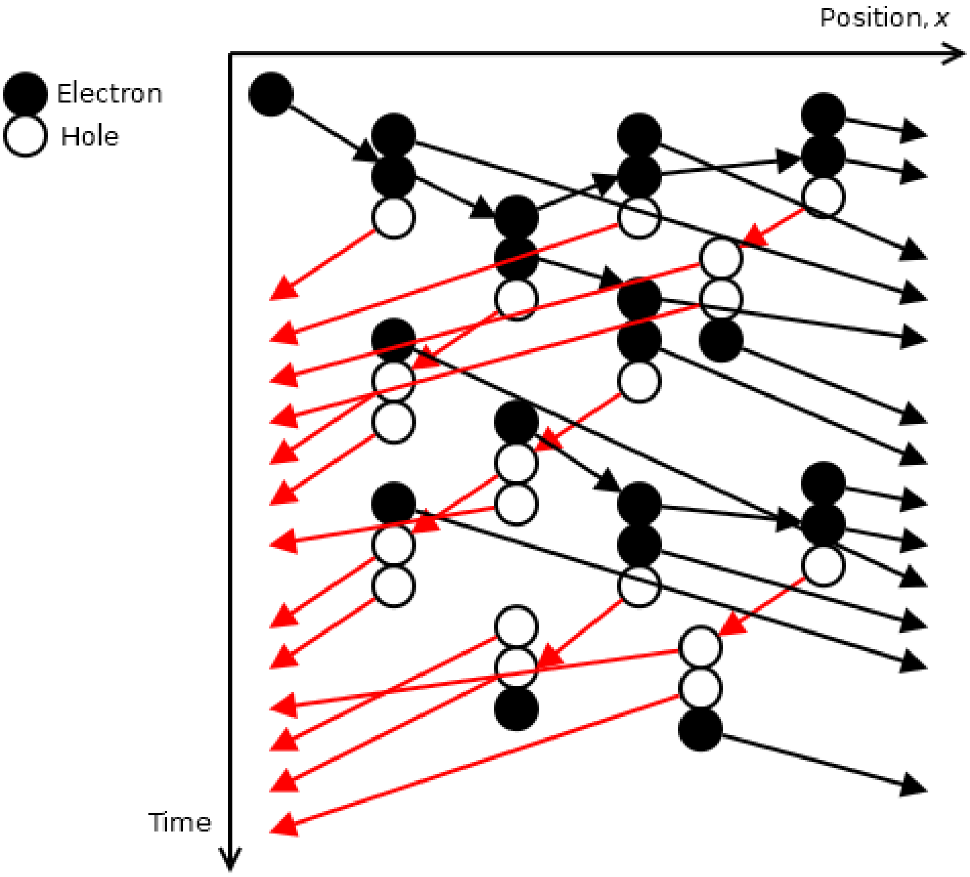

Figure 2.2: Schematic diagram showing avalanche multiplication in the case where α and β are similar. Electrons move in the x direction and holes move in the $-x$ direction.

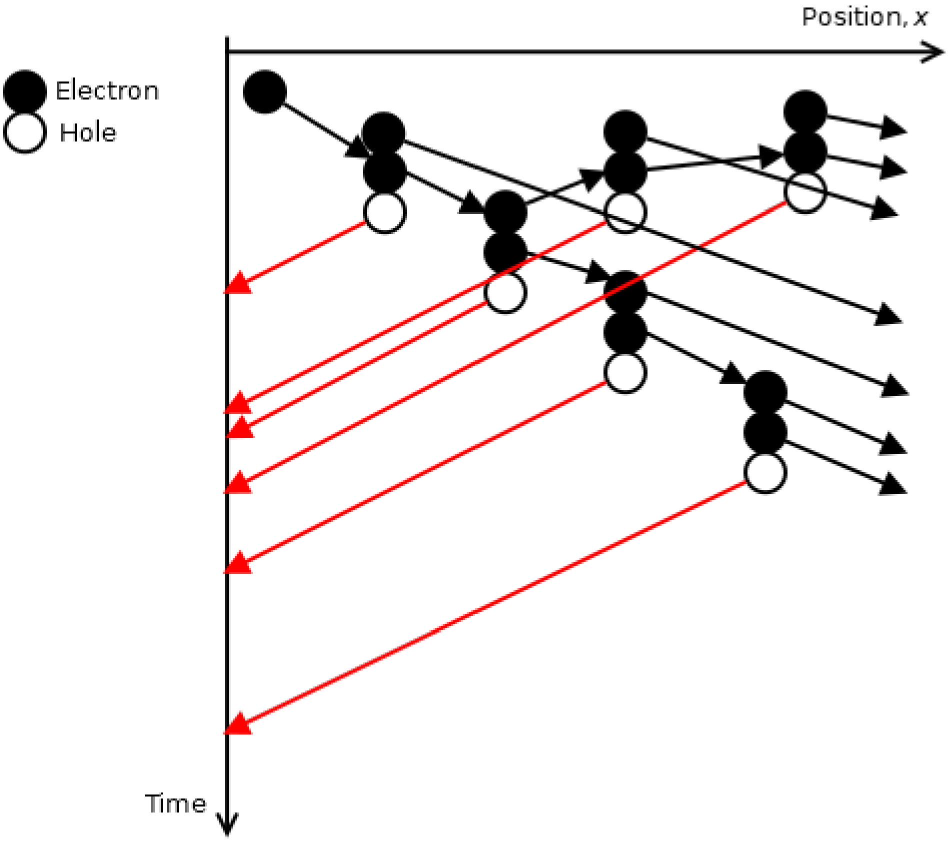

Figure 2.3: Schematic diagram showing avalanche multiplication in the case where α is significant and β tends to 0. Electrons move in the x direction and holes move in the $-x$ direction.

2.4 Carrier injection conditions

Injection conditions refer to which carrier types initiate the impact ionisation process. Pure electron injection conditions arise when all primary carriers are electrons, and pure hole injection conditions when all primary carriers are holes. Mixed injection conditions arise when there are primary carriers of both types.

Pure electron injection will occur in a PIN structure, with the light incident on the top $p+$ layer, if the light is of a sufficiently short wavelength that it is absorbed entirely in the $p+$ layer. Conversely, pure hole injection will occur in a NIP structure if the light is absorbed entirely in the top $n+$ layer. It is not generally possible to achieve pure electron injection in a NIP structure, or pure hole injection in a PIN structure. It is usual to use complementary PIN and NIP structures of a given material, with region widths and doping concentrations as similar as possible, to investigate the multiplication and excess noise behaviour under both pure electron and pure hole injection conditions. This allows the characteristics of the material to be cross-checked and modelled with less ambiguity. In general, pure injection conditions of the more readily ionising carrier type will yield the lowest possible excess noise, and pure injection conditions of the less readily ionising type will yield the highest possible excess noise.

Mixed injection will arise when carriers are generated in the intrinsic region. This will occur when incident light is of a longer wavelength that is more weakly absorbed. This will cause some photons to pass through the top layer before being absorbed. The longer the wavelength of light, the more uniform the absorption profile throughout the device will be. Ionisation events initiated by electrons will have the characteristics of pure electron injection conditions, and those initiated by holes will have the characteristics of pure hole injection conditions. The multiplication and excess noise characteristics developed by mixed injection will therefore be between the pure injection characteristics and determined by the relative numbers of electron-initiated and hole-initiated ionisation events. This means that if α and β are disparate, a uniform absorption profile will still produce multiplication and noise characteristics that are skewed towards the more readily ionising carrier type. This is because a generated carrier of the dominating carrier type will have many more ionisation events associated with it. It is therefore important to maintain very pure injection conditions, particularly if α and β differ significantly, when a small number of primary carriers of the opposite type may have a large effect on results.

2.5 Bandwidth of APDs

The bandwidth of an APD will be limited by either the carrier transit time or the RC time constant of the device, whichever is the longer. Device capacitance will be lower in structures with smaller areas and wider depletion regions, and series resistance can be minimised by optimising metal contacts.

Transit time will be determined by the width of the high-field region (it is notable that a wider high-field region may either: increase, through decreased capacitance; or decrease, through reduced transit time, device bandwidth.) and by carrier feedback effects. In cases where both carrier types impact ionise readily, secondary carriers of the opposite type to a primary carrier will traverse the electric field in the opposite direction to the primary carrier. For example: an electron traverses the high field region in the x direction. An impact ionisation event will produce a secondary electron and a secondary hole; the electron will travel in the x direction and the hole will travel in the $-x$ direction. If the hole does not impact ionise, the chain of ionisation events giving rise to multiplication will be due solely to carriers moving in the x direction, and the overall transit time will not be more than the time taken for a single carrier to traverse the high field region. If, however, ionisation events are triggered by both carrier types, the chain will incorporate carriers moving in both the x and $-x$ directions. This means that multiple transversals of the high-field region will occur and the transient response time will be increased, and increase further with increasing multiplication. Single-carrier multiplication is therefore desirable to yield the highest possible bandwidth, and true single carrier multiplication will yield bandwidth that does not decrease with gain, because the time for all carriers to leave the high-field region will be equal to the sum of the transit times for each carrier. This would result in an APD which is not limited by gain-bandwidth product [75].

2.6 The local model for avalanche multiplication

The simplest way to model avalanche multiplication is to assume that the probability of ionisation for a carrier of a given type, in a given material and at a known temperature, is a function only of the electric field at that carrier's current position. Using this assumption, a general relationship between the mean multiplication factor in an APD and the impact ionisation coefficients of the material can be expressed approximately in terms of the carrier pair generation rate, $U(x)$, with x representing the position in the high field region of the device. Electrons are considered to travel in the x direction, and holes in the $-x$ direction. Injection of all carriers at $x = 0$ then indicates pure electron injection, and injection of all carriers at $x = W_T$ indicates pure hole injection, where W_T represents the width of the high field region. This relationship is shown in equation 2.6 [76]:

$$1-\frac{1}{M}=\frac{(1-R_p)\int_0^{W_T}\alpha z(x)dx+R_p\int_0^{W_T}\beta z(x)dx-\int_0^{W_T}v(x)dx+\int_0^{W_T}v(x)z(x)dx}{1-R_p+R_p z(W_T)-\int_0^{W_T}v(x)dx+\int_0^{W_T}v(x)z(x)dx} \quad (2.6)$$

Where $R_p = J_{pi}/J_0$, $v(x) = qU(x)/J_0$, $J_0 = J_{ni}+J_{pi} + \int_0^{W_T} qU(x)dx$, q is the electronic charge, $J_{ni}(J_{pi})$ is the injected electron (hole) current at the edge of the high field region, and $z(x) = \exp\left(-\int_0^x(\alpha-\beta)dx'\right)$.

As electric field increases, multiplication will tend asymptotically towards infinity. The electric field at which multiplication becomes infinite in a given structure is referred to as the breakdown field, and the corresponding voltage as the breakdown voltage, V_{bd}.

Setting $v(x)$ and R_p to zero provides a simplified expression for the case of pure electron injection, shown in equation 2.7:

$$M_e=\frac{1}{1-\int_0^{W_T}\left[\alpha\exp\left(-\int_0^x\alpha-\beta\,dx'\right)\right]dx} \quad (2.7)$$

Similarly, setting $v(x)$ and R_p to 1 provides a simplified expression for the case of pure hole injection, shown in equation 2.8.

$$M_h=\frac{1}{1-\int_0^{W_T}\left[\beta\exp\left(\int_x^{W_T}\alpha-\beta\,dx'\right)\right]dx} \quad (2.8)$$

If the electric field in the high field region is uniform, these can be simplified further still to give equations 2.9 and 2.10.

$$M_e=\frac{1}{1-\frac{\alpha}{\beta-\alpha}\{\exp[(\beta-\alpha)W_T]-1\}} \quad (2.9)$$

$$M_h=\frac{1}{1-\frac{\beta}{\alpha-\beta}\{\exp[(\alpha-\beta)W_T]-1\}} \quad (2.10)$$

These can be rearranged to give equations 2.11 and 2.12, which allow the analytical calculation of α and β from multiplication data [77].

$$\alpha = \frac{1}{W_T}\left(\frac{M_e-1}{M_e-M_h}\right)\ln\left(\frac{M_e}{M_h}\right) \quad (2.11)$$

$$\beta = \frac{1}{W_T}\left(\frac{M_h-1}{M_e-M_h}\right)\ln\left(\frac{M_e}{M_h}\right) \quad (2.12)$$

These equations are valid only in structures that closely approximate an ideal PIN structure, with very low doping in the intrinsic region and high doping in the p^+ and n^+ regions. If this is not the case, then the electric field will extend significantly into the p^+ and n^+ regions. Additionally, the electric field will taper through the intrinsic region if the doping in it is not sufficiently low. A perfect PIN approximation will be more valid for thicker structures, in which the doped cladding regions make up a smaller proportion of the device. Given accurate measured data for M_e and M_h, it is possible to numerically infer α and β using equations 2.11 and 2.12 employing the method of Grant *et al.* [78], which transforms these equations into functions of electric field and allows a non-uniform electric field profile to be accommodated. Ionisation coefficients calculated using this method are referred to as effective ionisation coefficients, and should be considered as an empirical approximation of impact ionisation behaviour. This is because the equations listed thus far assume that the probability of impact ionisation for a carrier at a given position within a device depends only on the electric field at that position – the 'local' electric field. The limitations of this assumption are discussed in section 2.8.

2.7 Excess noise

Individual impact ionisation events occur stochastically, which means that the gain of an APD fluctuates around a mean value. This variation can be modelled as a noise source, and is referred to as excess noise. Excess noise increases with gain, and is often the factor which limits the maximum useful gain of APDs. Minimising excess noise is critical for all APD applications, and seeking new materials with characteristics conducive to low excess noise is the primary objective of the research described in this thesis.

All diodes produce noise proportional to the current flowing through them. This is referred to as shot noise, and is related to current by equation 2.13, where N is noise power spectral density in A^2/Hz, q is the electronic charge, I is the current, and B is the bandwidth across which the noise is being measured.

$$N = 2qIB \quad (2.13)$$

Excess noise is described by a quantity referred to as excess noise factor, *F.* The total mean square noise generated by an APD is given by equation 2.14:

$$\langle i^2 \rangle = 2qI_{pr}FM^2B_w \text{ (2.14)}$$

Where I_{pr} is primary photocurrent and B_w is the measurement bandwidth. *F* is defined by equation 2.15:

$$F = \langle M_i^2 \rangle / \langle M_i \rangle^2 \text{ (2.15)}$$

Seminal work on excess noise was undertaken by McIntyre [2], who described equations for excess noise factor as a function of impact ionisation coefficients for all cases of carrier injection conditions. It was shown that excess noise factor depends on the effective β/α ratio, referred to as *k.* Materials with more disparate ionisation coefficients will have lower excess noise factor, given pure injection conditions of the more readily ionising carrier type. This can be seen from equation 2.16 [2], which relates excess noise factor to multiplication factor and *k* under pure injection conditions. It can also be clearly seen that *F* is highly dependent on multiplication factor.

$$F = k_{eff}M + \left(2 - \frac{1}{M}\right)(1 - k_{eff}) \text{ (2.16)}$$

Where $k_{eff} = k = \beta/\alpha$ under pure electron injection conditions and $k_{eff} = 1/k$ under pure hole injection conditions. This equation predicts lower excess noise factor for thicker device structures, as α and β generally to diverge as electric field decreases. Although cases of very disparate ionisation coefficients can give the lowest possible noise, they can also give the highest possible noise if multiplication is initiated by carriers of the more weakly ionising type. The local model predictions for excess noise factor as a function of multiplication factor for different values of k_{eff} are shown in figures 2.4 and 2.5.

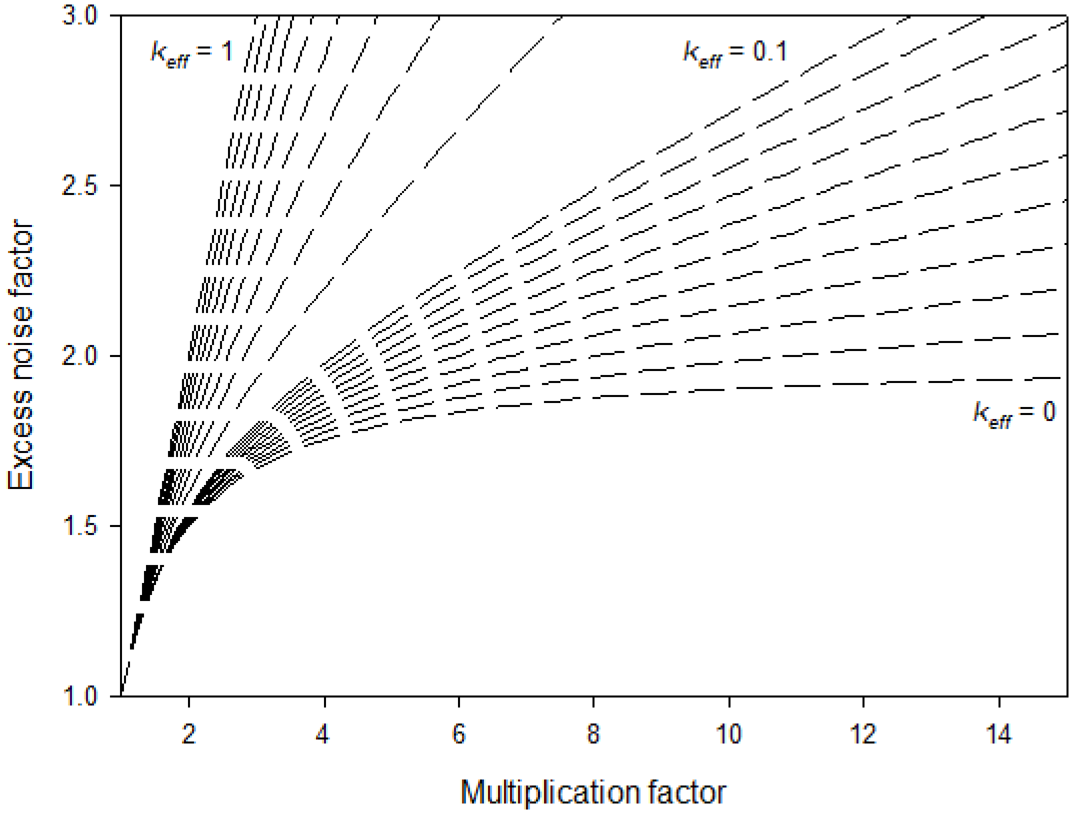

Figure 2.4: Theoretically predicted excess noise factor as a function of multiplication factor, for effective *k* values of 0 to 0.1 in steps of 0.01, and 0.1 to 1 in steps of 0.1 [2].

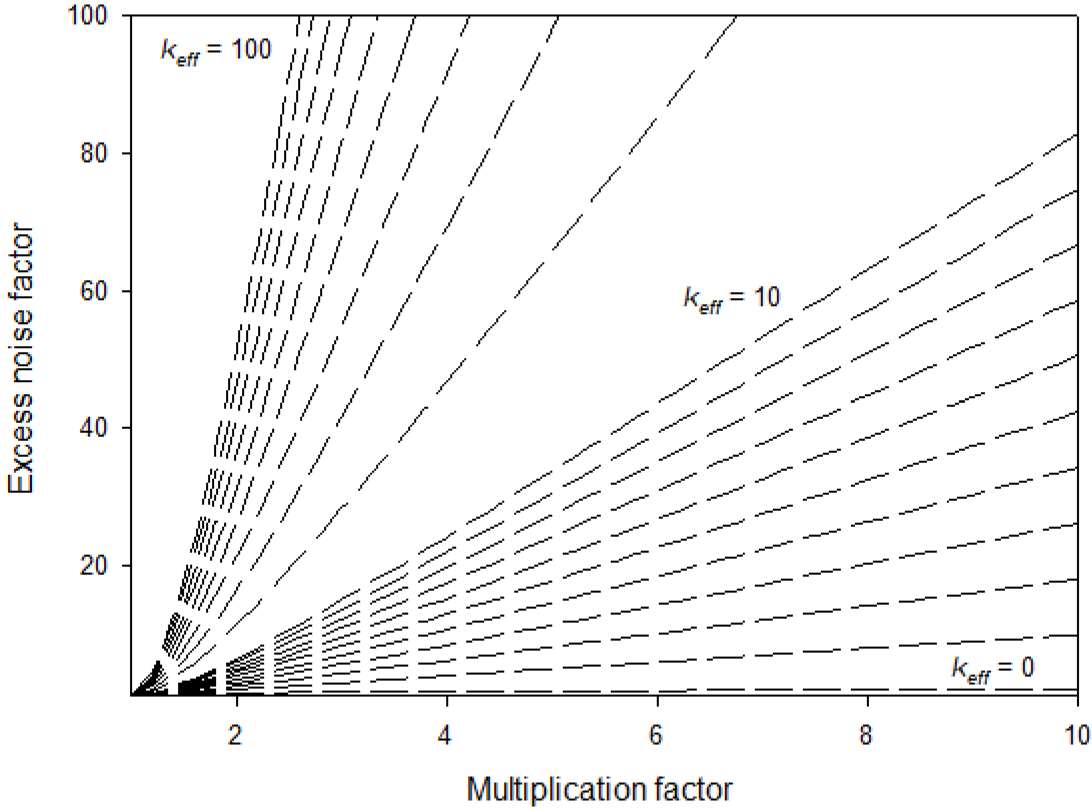

Figure 2.5: Theoretically predicted excess noise factor as a function of multiplication factor, for effective *k* values of 0 to 10 in steps of 1, and 1 to 10 in steps of 1 [2].

2.8 Limits of the local model

The local model described above is an approximation that assumes that the impact ionisation probability for a given carrier at a given position within a device is dependent only on the electric field at that position. A more accurate picture is given by considering the history of the carrier – the point at which the carrier was generated, either optically or by impact ionisation, and the electric field at this point and at all points which it has traversed to reach its current position [79]. A critical quantity for non-local modelling of impact ionisation is the carrier dead space. This term refers to the minimum distance that a carrier must travel through the high-field region before it gains sufficient kinetic energy for impact ionisation to occur. Dead space has a significant effect in structures in which it makes up a significant proportion of the high-field region. This is true in thinner structures and for materials with a wider band-gap, which have a larger dead space. Dead space is generally measured indirectly by considering the ionisation threshold energy.

Where dead space is significant, the history of the interactions of each carrier with the lattice and the electric field must be considered in order to accurately model multiplication and noise. In these cases, the local model will become less accurate. This is particularly significant for excess noise, as large dead space means that the impact ionisation process has fewer degrees of freedom for a structure of a given thickness at a given electric field. This means that the process is less random, and noise is reduced. Multiplication is also limited by dead space, and a large dead space will cause the avalanche breakdown voltage to increase. The dead space lengths for electrons and holes are related to their respective ionisation threshold energies by equations 2.18 and 2.19:

$$d_e = \frac{E_{the}}{q\xi} \quad (2.18)$$

$$d_h = \frac{E_{thh}}{q\xi} \quad (2.19)$$

Where ξ electric field, and E_{the} and E_{thh} are the electron and hole threshold energies respectively. The threshold energies represent the minimum energy required for a carrier of a given type to impact ionise, and take into account the requirements of energy and momentum conservation as well as any relevant scattering mechanisms. Once a carrier has traversed the dead space it is considered to be 'enabled,' and its subsequent probability of impact ionising is represented by the enabled ionisation coefficients, α^* and β^* for electrons and holes respectively. α^* and β^* are related to the effective ionisation coefficients (α and β), that would be inferred from a local model, by equations 2.20 and 2.21:

$$\frac{1}{\alpha} = \frac{1}{\alpha^*} + d_e \quad (2.20)$$

$$\frac{1}{\beta} = \frac{1}{\beta^*} + d_h \quad (2.21)$$

α and β will be smaller than α^* and β^* because they represent the probability of ionisation over the full path length of the carrier, whereas α^* and β^* represent the probability of ionisation only once the carrier has traversed the dead space.

Additionally, if α or β tends towards zero, one carrier type will be entirely responsible for the avalanche multiplication process. This is referred to as single carrier multiplication. The case of single carrier multiplication provides a lower number of possible multiplication values for a given electric field. This leads to decreased excess noise, which can be lower than the minimum noise permitted by McIntyre's local model. Additionally, in a thin device operating at a high electric field, the average ionisation path length can become short enough that it is similar to the dead space. In this case a carrier may ionise almost immediately upon traversing the dead space, resulting in a multiplication process that is highly deterministic. In this case it is possible for the excess noise factor to be lower than 2, which is the theoretical minimum of the local model at high multiplication values [80].

The significance of dead space effects was brought to light by research on thin GaAs structures in the late 1990s, which were found to have noise characteristics which differed from those predicted by McIntyre [73], [81]. This has preceded significant developments in the design of device structures which take advantage of nonlocal effects to produce a new generation of low-noise, high-speed APDs [82]. Most III-V semiconductor alloys have similar impact ionisation coefficients for electrons and holes, leading to high excess noise in thick structures. Utilising thin structures to take advantage of the effects of dead space is therefore generally seen as necessary to produce low-noise devices.

2.9 Non-local modelling of avalanche multiplication and noise

2.9.1 Recursive and random path length modelling

The first model to accurately incorporate the dead space was the recursive technique of Hayat *et al.*[83]. This method models the ionisation path length of a carrier as a probability density function (PDF), $h(x)$. The ionisation PDFs assumed by various models are shown in figure 2.6.

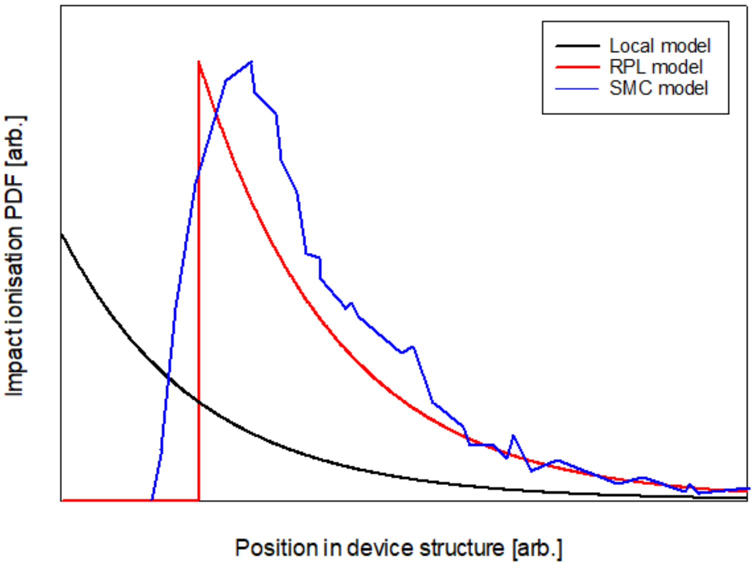

Figure 2.6: Diagram showing examples of ionisation PDFs assumed by the local, RPL, and SMC models. The shape of the PDF used by the RPL model is that assumed by the recursive technique of Hayat *et al.* [83].

The PDF is zero when the distance that the carrier has travelled is less than the dead space and is represented by an exponential decay after the carrier has traversed the dead space. For an electron-hole pair injected at position x_0 in a device with uniform electric field, the probabilities of ionisation at position x are given by equations 2.22 and 2.23:

$$h_e(x|x_0) = \begin{cases} 0 & \text{for } x-x_0<d_e \\ \alpha^*\exp[-\alpha^*(x-x_0-d_e)] & \text{for } x-x_0\geq d_e \end{cases} \quad (2.22)$$

$$h_h(x|x_0) = \begin{cases} 0 & \text{for } x_0-x<d_e \\ \beta^*\exp[-\beta^*(x_0-x-d_h)] & \text{for } x_0-x\geq d_e \end{cases} \quad (2.23)$$

Where electrons travel in the x direction and holes travel in the $-x$ direction. These expressions can be generalised for devices which do not approximate a uniform electric field profile to equations 2.24 and 2.25 [79], [84]:

$$h_e(x|x_0) = \alpha(x|x_0)\exp\left(-\int_{x_0}^{x} \alpha(x'|x_0)\,dx'\right)dx \quad (2.24)$$

$$h_h(x|x_0) = \beta(x|x_0)\exp\left(-\int_x^{x_0} \beta(x'|x_0)\,dx'\right)dx \quad (2.25)$$

Where $\alpha(x|x_0)$ and $\beta(x|x_0)$ are the position dependent impact ionisation coefficients at position x for a carrier generated at position x_0. These are zero before the carrier has traversed the dead space. The exponential term represents the probability that the carrier will travel from its generation point to position x without impact ionising. The dead space lengths for electrons and holes can be calculated using equations 2.26 and 2.27:

$$E_{the} = \int_{x_0}^{x_0+d_e} q\xi(x')dx' \quad (2.26)$$

$$E_{thh} = \int_{x_0-d_h}^{x_0} q\xi(x')dx' \quad (2.27)$$

$z(x_0)$ and $y(x_0)$ are respectively the average number of electrons and holes generated by a given primary carrier pair, and are expressed by equations 2.28 and 2.29:

$$z(x_0) = \left[1 - \int_{x_0}^{W} h_e(x|x_0)dx\right] + \int_{x_0}^{W}[2z(x) + y(x)]h_e(x|x_0)dx \quad (2.28)$$

$$y(x_0) = \left[1 - \int_0^{x_0} h_h(x|x_0)dx\right] + \int_0^{x_0}[2y(x) + z(x)]h_h(x|x_0)dx \quad (2.29)$$

Where W is the width of the high-field region. The first term in each of these equations represents the probability that the carrier travels to end of the high-field region without impact ionizing, and the second term represents the probability that the carrier ionises to produce an additional electron-hole pair. The expressions can be solved numerically. The mean multiplication and excess noise factor are given by equations 2.30 and 2.31:

$$M(x_0) = \frac{z(x_0)+y(x_0)}{2} \quad (2.30)$$

$$F(x_0) = \frac{\langle M(x_0)^2\rangle}{\langle M(x_0)\rangle^2} = \frac{z_2(x_0)+2z(x_0)y(x_0)+y_2(x_0)}{\left(z(x_0)+y(x_0)\right)^2} \quad (2.31)$$

Where $z_2(x_0)$ and $y_2(x_0)$, the second moments of $z(x_0)$ and $y(x_0)$, are expressed by equations 2.32 and 2.33:

$$z_2(x_0) = \left[1 - \int_{x_0}^{w} h_e(x|x_0)dx\right] + \int_{x_0}^{w} [4z^2(x) + y^2(x) + 4z(x)y(x)]h_e(x|x_0)dx \quad (2.32)$$

$$y_2(x_0) = \left[1 - \int_{0}^{x_0} h_e(x|x_0)dx\right] + \int_{0}^{x_0} [4y^2(x) + z^2(x) + 4z(x)y(x)]h_e(x|x_0)dx \quad (2.33)$$

The random path length (RPL) model of Ong *et al.* [85] uses the PDF expressions listed above, but calculates multiplication and noise using a Monte Carlo method rather than through a numerical iteration.

For a carrier generated at position x_0, the probability of impact ionising before reaching position *x* can be calculated by integrating equations 2.22 and 2.23 to give equations 2.34 and 2.35:

$$P_e(x_0 < y < x|x_0) = \begin{cases} 0 & \text{for } x - x_0 < d_e \\ 1 - \exp[-\alpha^*(x - d_e)] & \text{for } x - x_0 \geq d_e \end{cases} \quad (2.34)$$

$$P_h(x < y < x_0|x_0) = \begin{cases} 0 & \text{for } x_0 - x < d_h \\ 1 - \exp[-\beta(d_h - x)] & \text{for } x_0 - x \geq d_h \end{cases} \quad (2.35)$$

The survival probabilities, which are the probabilities that the carrier does not ionise before reaching position *x*, are given by equations 2.36 and 2.37:

$$S_e(x_0 < y < x|x_0) = 1 - P_e(x_0 < y < x|x_0) = \begin{cases} 1 & \text{for } x - x_0 < d_e \\ \exp[-\alpha^*(x - d_e)] & \text{for } x - x_0 \geq d_e \end{cases} \quad (2.36)$$

$$S_h(x_0 < y < x|x_0) = 1 - P_h(x < y < x_0|x_0) = \begin{cases} 1 & \text{for } x_0 - x < d_h \\ \exp[-\beta^*(d_h - x)] & \text{for } x_0 - x \geq d_h \end{cases} \quad (2.37)$$

If S_e and S_h are denoted by the symbols r_e and r_h, equations x and y can be rearranged to give equations 2.38 and 2.39:

$$x_e = d_e - \frac{\ln(r_e)}{\alpha^*} \quad (2.38)$$

$$x_h = d_h - \frac{\ln(r_h)}{\beta^*} \quad (2.39)$$

Where x_e and x_h are the distances that a given electron or hole will travel before it impact ionises.

In the RPL model, a pseudo-random-number generator is used to produce a uniformly distributed random number between 0 and 1, and these values are used for r_e and r_h to calculated to ionisation paths for carriers. Beginning with a primary carrier at position x_0 , the positions of all electrons and holes in the device, and the positions of each impact ionisation event, are tracked until all carriers have exited the high-field region. This constitutes one trial. This is repeated for several thousand trials to provide an average multiplication value. The average multiplication value is expressed by equation 2.40:

$$M(x_0) = \frac{M_1+M_2+M_3+\cdots+M_{n}{}_{th}}{N} = \sum_{N=1}^{N} M_N \text{ (2.40)}$$

Where N is the number of trials and M_N is the multiplication value calculated for a given trial. Excess noise factor can then be calculated using equation 2.41:

$$F(x_0) = \frac{1}{NM^2(x_0)} \sum_{N=1}^{N} M_N^2 \text{ (2.41)}$$

2.9.2 Monte-Carlo modelling

Full-band Monte-Carlo (FBMC) modelling has been used to model carrier transport in various semiconductors at high electric fields [80], [86]–[89]. These models can predict multiplication and noise to a high degree of accuracy, even in very thin structures, by incorporating the details of the semiconductor band-structure and the rates of scattering mechanisms such as acoustic, optical, and polar optical phonon scattering, and alloy scattering. An FBMC model uses a more realistic ‘soft’ representation of dead space. This means that the probability of a carrier ionising before it has traversed the dead space is low but non-zero, and that the probability of a carrier ionising continues to increase as its energy increases above the threshold energy. This contrasts against the ‘hard’ dead space approximation used by the RPL model, which assumes that the probability of a carrier ionising before it has traversed the dead space is zero and that the peak probability of ionisation is immediately after the dead space has been traversed. Studies using FBMC models have shown that the majority of carriers that initiate impact ionisation events do so from higher-energy bands, meaning that the secondary carriers that they generate have significant initial energy [90]. FBMC models represent the ‘gold standard’ for modelling of impact ionisation processes but require detailed knowledge of the band-structure and scattering rates, which is generally only available for materials that have been widely studied. FBMC models are also highly computationally intensive.

The simple Monte-Carlo (SMC) model was developed by Plimmer *et al.* [90]. It operates on a similar principle to the FBMC model, but using a simplified band-structure. Rather than taking into account the details of the Γ, X, and L valleys, it is assumed that the valence and conduction bands each consist of a single parabolic band only. Scattering rates for phonon absorption and emission are given by equation 2.42:

$$R_{ph} = \begin{cases} C_{ph} N \sqrt{E + h\omega} & \text{for phonon absorption} \\ C_{ph}(N+1)\sqrt{E - h\omega} & \text{for phonon emission} \end{cases} \quad (2.42)$$

Where $C_{ph} = \sqrt{(\frac{2}{m^*})}/[(2N+1)\lambda_i]$, $N = \left[\exp\left({}^{h\omega}/_{k_B T}\right) - 1\right]^{-1}$ is the phonon occupation factor, k_B is the Boltzmann constant, T is the temperature, $h\omega$ is the phonon energy, λ_i is the phonon mean free path, $m^*$is the effective mass of the carrier, and E is the energy of the carrier. The scattering rate from impact ionisation is given by equation 2.43:

$$R_{ii} = C_{ii}\left(\frac{E - E_{th}}{E_{th}}\right)^{\theta} \quad (2.43)$$

Where C_{ii} is a 'softness' factor, which describes the rise in the ionisation probability above the threshold energy, $E_{th}$is the threshold energy for the given carrier type and θ is a power index which is also related to the softness of the threshold energy. More recent SMC models also incorporate other scattering mechanisms such as self-scattering [91] and alloy scattering [92], [93]. SMC models have been used to accurately model avalanche multiplication and excess noise in devices of a wide range of thicknesses. Parameter sets are available for various semiconductor materials [91] including silicon [94], GaAs [90], $In_{0.48}Ga_{0.52}P$ [95], and InAlAs [93].

2.10 Dark current

Dark current refers to any current in a photodiode that does not result from optically generated primary carriers. There are various possible sources of dark current, which may be broadly categorised into surface and bulk dark currents. Of these, bulk dark current is the most detrimental to device performance. This is because it will be multiplied by any avalanche gain in the device, and noise power associated with it will be multiplied by the square of the avalanche gain factor. This means that multiplied bulk dark current can significantly reduce signal-to-noise ratio.

Bulk dark currents generally result from the properties of the semiconductor crystal, either due to the characteristics of the semiconductor alloy or the defect concentration in the specific wafer. The theoretical minimum for bulk dark current in a diode is the saturation current, J_0. This is related to the carrier diffusion lengths by equation 2.44 [96]**:**

$$J_0 = \frac{qD_h n_i^2}{L_h N_D} + \frac{qD_e n_i^2}{L_e N_A} \quad (2.44)$$

Where q is the electronic charge, n_i is the intrinsic carrier concentration of the semiconductor, D_e and D_h are the electron and hole diffusion coefficients respectively, L_e and L_h are the electron and hole diffusion lengths respectively, and N_D and N_A are the donor and acceptor concentrations respectively. Bulk dark current may be due to band-to-band tunnelling, which is higher in narrower band-gap alloys [97]. Current density due to band-to-band tunnelling is related to the band-gap by equation 2.45**:**

$$J_{tunn} = \frac{(2m^*)^{\frac{1}{2}} q^3 \xi}{h^2 E_g^{\frac{1}{2}}} \exp\left(-\frac{2\pi \sigma_T m^{*\frac{1}{2}} E_g^{\frac{3}{2}}}{q h \xi}\right) \quad (2.45)$$

Where m^* is the electron effective mass, h is Planck’s constant, ξ is the electric field across the junction, E_g is the semiconductor band-gap, and σ_T is a constant that depends on the shape of the tunnelling barrier [98]. Tunnelling current is higher in thinner device structures due to the higher electric fields to which they are subjected. Tunnelling current is significantly lower in indirect band-gap semiconductors because phonons or other scattering agents must be involved in the tunnelling process in order to conserve momentum [99].

Another mechanism of bulk dark current is Shockley-Read-Hall generation-recombination, which results from defects or dopants that create additional energy states in the forbidden gap. Carriers may then gain enough energy to reach this additional energy state, and then move further into the conduction band in a two-step process. In the case that the defect state exists at $E_g/2$, which gives the highest generation and recombination rates, the current due to this mechanism is given by equation 2.46 [64], [65]**:**

$$J_{SRH} = \frac{q n_i w}{2\tau_{eff}} \left[\exp\left(-\frac{qV}{2k_b T}\right)\right] \quad (2.46)$$

Where w is the depletion width and τ_{eff} is the effective carrier generation rate.

Surface dark currents often dominate in wide band-gap semiconductors, and may result from carrier generation-recombination or reduced resistivity on the surface of the device. Defect concentrations on the device surface may be increased due to dangling bonds or if the semiconductor alloy is prone to oxidisation. Surface dark currents will also be increased by un-optimised etching and can be reduced by improving this and other fabrication techniques, such as surface passivation or use of planarised device structures.

2.11 Temperature dependence of impact ionisation

The avalanche multiplication process is temperature dependent because the probability of each impact ionisation event is determined by various factors that are themselves temperature dependent.

In wider band-gap semiconductors the most significant of these factors is phonon scattering, which will prevent carriers from acquiring sufficient energy to impact ionise and increases with temperature. This means that, in general, avalanche multiplication will decrease and breakdown voltage will increase as temperature increases [100]. This is the dominant mechanism in silicon [12] and GaAs as well as most wider band-gap III-V alloys. In narrower band-gap semiconductors, the dominant mechanism is the decrease in the energy band-gap with temperature [101]. In narrow, direct band-gap materials such as InGaAs [102] and InAs [103], the ionisation threshold energy is closely related to the minimum energy band-gap [104]. This causes avalanche multiplication to increase, and breakdown voltage to decrease, with increasing temperature [101]. The change in breakdown voltage with temperature is denoted by the temperature coefficient of breakdown, C_{bd}, which is defined in equation 2.47:

$$C_{bd} = \frac{\Delta V_{bd}}{\Delta T} \quad (2.47)$$

Where ΔV_{bd} is the change in breakdown voltage and ΔT is the change in temperature. A low C_{bd} is desirable to maintain stability of device performance across a range of temperatures. Thinner structures will generally exhibit lower C_{bd} as carriers will be subject to higher electric fields, meaning that they will gain energy across a shorter distance and be less likely to interact with phonons before gaining sufficient energy to impact ionise [105]. C_{bd} is also lower in materials with higher alloy disorder potential, ΔE_a, because alloy scattering becomes the dominant scattering mechanism and this is not a temperature dependent process [104]. Materials with high ΔE_a also show a reduced change in C_{bd} with device thickness [106]. It has also been suggested that materials with larger phonon energies will also show reduced C_{bd} as the change in phonon scattering rates with temperature will be decreased [107].

Chapter 3: Fabrication and measurement techniques

3.1 Introduction

Various electrical and optical characterisation techniques were used to measure the APD structures described in this work. This chapter describes the process of fabricating the devices and will discuss the purpose of each measurement, as well as the experimental setup used. Measurements include standard electrical diode characterisation such as current-voltage and capacitance-voltage, and more specific techniques for the measurement of photocurrent, avalanche multiplication and excess noise factor. The measurement of excess noise is of particular importance to this work and is described in detail, and possible sources of error in this measurement are also described. All measurements were carried out at room temperature.

3.2 Device fabrication

All samples were fabricated as standard mesa diodes. Devices were fabricated at Sheffield, Cardiff University, and Ohio State University (OSU). The processes used for fabrication at each facility are broadly similar. The fabrication process first involves cleaning using n-butyl acetate, acetone, and isopropyl alcohol. For samples grown on doped substrates, back contact metallisation is then performed using a thermal evaporator. Top contact metallisation is performed using thermal evaporation and standard UV photolithography techniques. For the samples fabricated at OSU, electron beam evaporation was used instead of thermal evaporation. For the $(Al_xGa_{1-x})_{0.52}In_{0.48}P$ devices described in chapter 4, In/Ge/Au or Au/Zn/Au was used to form ohmic contacts. These structures were annealed at 420°C following metallisation to promote metal diffusion. The $Al_xGa_{1-x}As_{0.56}Sb_{0.44}$ devices in chapters 5 and 6 used Ti/Au Schottky contacts. For structures grown on semi-insulating substrates, a grid contact was deposited on the bottom cladding layer after mesa etching.

Standard wet etching was used to fabricate mesa structures. $(Al_xGa_{1-x})_{0.52}In_{0.48}P$ devices were etched using the universal etchant of hydrobromic acid, acetic acid, and potassium dichromate in a 1:1:1 ratio. The GaAs caps on these devices were removed using an etchant of sulphuric acid, hydrogen peroxide, and deionised water in a 1:8:80 ratio. The etchant used for the $Al_xGa_{1-x}As_{0.56}Sb_{0.44}$ devices consisted of citric acid, orthophosphoric acid, hydrogen peroxide, and deionised water in a ratio of 4:1:1:24. Mesas were of various diameters depending on the photolithography mask used – either 440, 240, 140, and 70µm, 420, 220, 120, and 60µm, or 400, 200, 100, and 50µm. Different masks were used at different fabrication facilities and the details of specific devices are given in the relevant chapters.

Mesa sidewalls were passivated using SU-8, a photoresist produced by Microchemicals which is mechanically and thermally stable once cured. Photolithography is used to ensure that the SU-8 covers the sidewalls only. The SU-8 may then be coated with gold, to ensure that light does not enter the sidewalls and cause unintended optical injection.

The specific details of each sample measured, including the device diameters used and the location of fabrication, are described in the relevant results chapters.

3.3 Dark current-voltage measurement

Dark current-voltage (I-V) measurements provide an outline of the basic characteristics of a semiconductor device. The forward and reverse bias characteristics of a diode shed light on different aspects of its behaviour. Forward I-V characteristics indicate whether the device in question obeys the Shockley equation, and therefore how closely it behaves like an 'ideal' diode. The forward I-V characteristic of a diode is approximately represented by equation 3.1 [96]:

$$I = I_s \exp\left(\frac{qV_f}{n_{id}k_BT}\right) \quad (3.1)$$

Where I_s is saturation current, V_f is forward bias voltage, and n_{id} is the ideality factor of the diode, which generally has a value between 1 and 2.

An ideality factor of 1 indicates that the dominating current mechanism is diffusion of carriers across the junction, and an ideality factor of 2 indicates that the dominating mechanism is carrier generation and recombination. Higher values generally indicate the presence of defects and poorer crystal quality.

The forward I-V characteristic can also be used to infer series resistance. When a non-negligible series resistance is present, equation 3.1 becomes:

$$I = I_s \exp\left(\frac{q(V_f - IR_s)}{n_{id}k_BT}\right) \quad (3.2)$$

High series resistance will cause current to be suppressed when it becomes high enough to produce a significant voltage drop across the series resistance. This will distort photocurrent measurements and limit the maximum possible multiplication. High series resistance also distorts excess noise measurements, as described in section 3.8.

The effect of series resistance on the forward I-V characteristic of a diode is shown in figure 3.1:

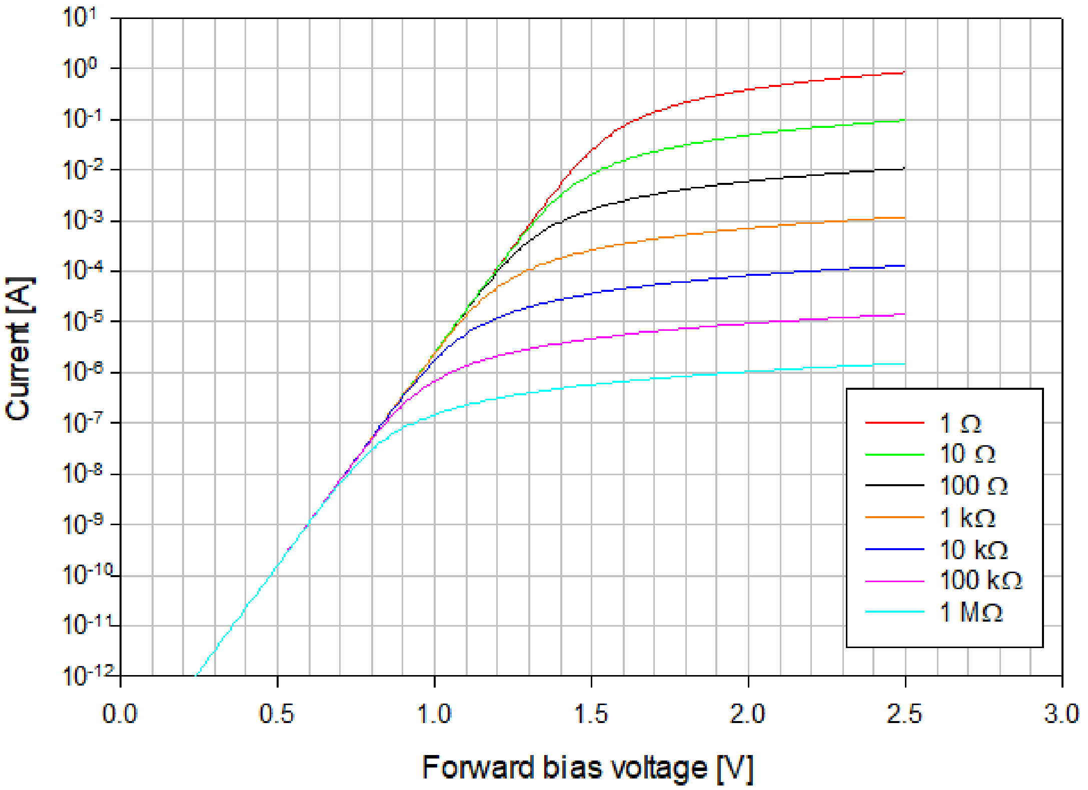

Figure 3.1: Theoretical forward bias current-voltage characteristics for a diode with I_s of 1x10^{-14}A, n_{id} of 2, and varying R_s for T = 300K.

The modified Shockley equation can be rearranged in terms of I only using Lambert's Omega function, as shown in equation 3.3**:**

$$I = -\frac{-n_{id}kT\mathrm{W}\left(\frac{qR_S I_S \exp\left(\frac{q(V_a+R_S I_S)}{n_{id}kT}\right)}{n_{id}kT}\right)+qR_S I_S}{qR_S} \quad (3.3)$$

It is possible to determine n_{id}, I_s, and R_s by using this expression to produce simulated forward IV data which can be compared to measured data using the above quantities as fitting parameters.

Reverse I-V characteristics indicate the voltage at which a device breaks down. It may be possible to determine the nature of breakdown – bulk avalanche breakdown, where the electric field across the device causes impact ionisation to such an extent that the current multiplication is infinite, is preferable. The maximum electric field that a device can tolerate without breaking down is a property of the semiconductor material at a given temperature. Breakdown may also occur when the device structure is such that localised high electric fields are manifest, generally at the edge of a mesa structure. This is referred to as 'edge breakdown.' Edge breakdown will cause the device to break down at a lower bias voltage than that required for bulk breakdown. Low dark current before breakdown is desirable. High dark currents may result from surface leakage or from tunnelling, which is particularly prevalent in materials with narrower band-gaps. Different mechanisms of dark current are discussed in chapter 2.

I-V measurements on devices of different sizes can also be used to infer the nature of current flow. If the current scales with device area, this indicates that bulk current is dominating. If, however, it scales with device perimeter, this indicates that most of the current is flowing along the surface of the devices. If dark current scales with neither area nor perimeter, this indicates that both bulk and surface dark currents are significant. Non-uniformity in dark current characteristics between devices on the same wafer may be due to non-uniformity in the semiconductor crystal or in the etching process.

Dark I-V measurements in this work were taken using an HP4140B pico-ammeter, unless stated otherwise.

3.4 Capacitance-voltage measurement

Capacitance-voltage (C-V) measurements of a semiconductor device under reverse bias provide information about the device structure and doping concentrations. The capacitance of a diode can be modelled using the Poisson equation, which relates the total charge concentration on either side of the junction to the electric field gradient. The equation for the *p*-doped side is:

$$-\frac{d^2\Psi}{dx^2} = \frac{d\xi}{dx} = \frac{\rho(x)}{\varepsilon_0\varepsilon_r} = -\frac{q[N_a(x)+p_p(x)]}{\varepsilon_0\varepsilon_r} \quad (3.4)$$

The equation for the *n*-doped side of the junction is:

$$-\frac{d^2\Psi}{dx^2} = \frac{d\xi}{dx} = \frac{\rho(x)}{\varepsilon_0\varepsilon_r} = -\frac{q[N_d(x)+n_n(x)]}{\varepsilon_0\varepsilon_r} \quad (3.5)$$

Where $\Psi = V_t+V_{bi}$ is the total voltage across the junction, $\rho(x)$ is the total charge concentration, $N_a(x)$ is the acceptor dopant concentration, $p(x)$ is the hole concentration, N_d is the donor dopant concentration, and $n(x)$ is the electron concentration. As the total charge in the depleted regions either side of the junction is equal, these equations can be solved analytically using the expressions in appendix I to give the total depletion width given the dopant densities in each region of the device. The depletion distance in a semiconductor junction is approximately related to the capacitance by equation 3.6:

$$C = \frac{\varepsilon_0\varepsilon_r A}{W_T} \quad (3.6)$$

Where C is capacitance, ε_0 is the permittivity of free space, ε_r is the dielectric constant of the semiconductor, A is the area of the diode junction, and W_T is the total depletion width of the junction.

The reverse C-V characteristic can therefore be used to estimate the widths and doping densities of a device by adjusting region dopings and widths in a Poisson solver to produce simulated data that matches the measured data. Derivations for the equations used by the Poisson solver are given in appendix I. Doping profiles for the PIN and NIP structures investigated in this work were assumed to be abrupt and to consist of three regions only. Static dielectric constants were used, as the relative permittivity of III-V materials generally remains constant up to frequencies of several GHz or more [108]. This method also requires knowledge of the built-in potential of the junction. This can be calculated using equation 3.7 [109]:

$$\frac{1}{C^2} = \frac{2}{q\varepsilon_0\varepsilon_r A^2 N}\left(V_{bi} - V - \frac{2k_B T}{q}\right) \qquad (3.7)$$

Where V is positive for forward bias and negative for reverse bias. V is approximately equal to V_{bi} when $\frac{1}{C^2} = 0$, so V_{bi} can be approximated by taking the value at which a plot of $\frac{1}{C^2}$ against voltage crosses the voltage axis.

Capacitance-voltage data presented in this work were, unless stated otherwise, measured using an HP4175B LCR meter. Devices were biased with a DC voltage signal, superimposed with an AC test signal at a frequency of 1MHz and an amplitude of approximately 65mV. The capacitance of the device at a given bias voltage is calculated using the measured impedance and phase angle. A phase angle which deviates significantly from 90° is considered to invalidate the measurement, as the device is not behaving as an ideal resistor-capacitor circuit. Capacitance is expected to scale with device area, and this can be used to confirm that the nominal device radii are correct.

3.5 Spectral response measurement

Spectral response measurements are used to determine the relative responsivity of a photodetector to different wavelengths. The measurement setup used for the spectral response measurements in this work consisted of a tungsten lamp light source, a Horiba Scientific iHR320 monochromator a Keithley 236 SMU, an SR830 lock-in amplifier, and a desktop computer with data acquisition software. A diagram of the measurement setup is shown in figure 3.2.

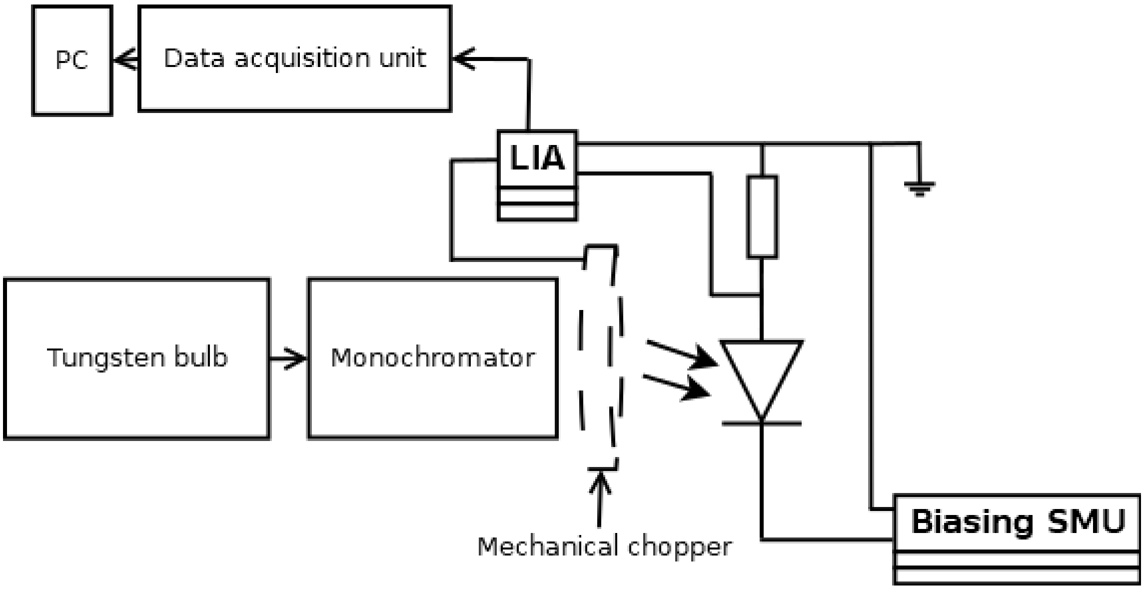

Figure 3.2: Diagram showing measurement setup for spectral photocurrent response.

The light from the lamp was modulated at 180Hz using a mechanical chopper and passed through the monochromator, the output of which was focused onto the DUT using a microscope objective. The device was biased using the SMU and the output current was passed through a resistor to convert it into a voltage signal. The output due to the photocurrent was separated from that due to the dark current using the lock-in amplifier. Data acquisition software was used to perform a sweep of wavelengths using the monochromator and record the relative output of the lock-in amplifier for each.

The relative optical power output of the monochromator at each wavelength is calculated using a commercial photodiode with known responsivity, by dividing the measured response of the commercial device by the spectral responsivity given on the datasheet.

3.6 Multiplication measurement

3.6.1 Methodology

Avalanche multiplication factor, M, is calculated by dividing the device photocurrent, I_{ph} to the unmultiplied photocurrent (the primary photocurrent, I_{pr}), as shown in equation 3.8:

$$M = \frac{I_{\mathrm{ph}}}{I_{\mathrm{pr}}} \qquad (3.8)$$

This first necessitates measurement of the photocurrent. The simplest form of photocurrent measurement is identical to dark I-V measurement, but with the device illuminated. This measurement does not separate the photocurrent from the dark current and is inaccurate unless the photocurrent is significantly larger than the dark current. It is possible to perform I-V sweeps both in the dark and under illumination, and subtract the dark current from the overall current in order to calculate the photocurrent. However, this method is also inaccurate unless the photocurrent is comparable in amplitude to the dark current. In most cases it is preferable to use phase-sensitive detection to differentiate between the components of the current. This is done by modulating the optical input signal electronically or using a mechanical chopper. The controller of the modulator provides a reference signal for a lock-in amplifier, which detects signals of the same frequency and phase. A resistor is placed in series with the device to produce a voltage signal proportional to the device current. Larger resistors produce a larger voltage signal but introduce more thermal noise. They can also limit current if it becomes sufficiently high. Photocurrent can also be measured using a transimpedance amplifier, as described in the section 3.7.

3.6.2 Calculation of primary photocurrent

In order to calculate avalanche multiplication factor, the value of the unmultiplied photocurrent (the primary photocurrent, I_{pr}) must also be known. Primary photocurrent generally increases with increasing reverse bias, and it is necessary to differentiate this increase from that due to impact ionisation. As reverse bias voltage increases, the depletion region of a PIN diode extends into the doped cladding layers. This means that charge carrier pairs generated outside the depletion region have a higher chance of diffusing into it and being collected by the electric field. This increases the primary photocurrent. The increase due to the movement of the depletion edge can be determined using the equation of Woods *et al.* [76], shown as equation 3.9 below.

$$J_{pr} = \frac{qG_0}{\cosh(L - L_{\mathrm{pn}})} \quad (3.9)$$

Where J_{pi} is the primary photocurrent density, q is the electronic charge, G_0 is the minority carrier generation rate per unit area at one edge of the device, L_{pn} is the minority carrier diffusion length, and L is the distance between the edge of the device, where carriers are injected, and the edge of the depletion region. L is given by equation 3.10:

$$L = L_0 - W = L_0 - \sqrt{\left(\frac{2\varepsilon}{qN_D}\right)(V + V_D)} \qquad (3.10)$$

Where L_0 is the thickness of the device, ε is the permittivity of the semiconductor, N_D is the net donor density in the region under consideration, V is the reverse bias voltage, and V_D is the built-in voltage of the device. It should be noted that this equation assumes a one-sided junction with a single semiconductor region of uniform doping, and deviations from this must be accounted for when using it. It also assumes that carriers are injected uniformly at one edge of the device.

If the intrinsic region of a PIN device is already depleted at the electric field at which impact ionisation starts, only the depletion continuing into the highly doped cladding layers is considered. In this case the primary photocurrent increases approximately linearly with increasing reverse bias voltage and can be calculated by regressing the linear part of the photocurrent characteristic at bias voltages, where impact ionisation has not begun. The straight line calculated thus can then be extrapolated to give the primary photocurrent at voltages where avalanche multiplication is occurring. This method is preferable where possible as the primary photocurrent can be empirically calculated from the data without necessitating additional calculation or assumptions. However, for devices in which impact ionisation occurs at electric fields lower than that at which the intrinsic region becomes fully depleted, it is necessary to calculate primary photocurrent using the complete form of the Woods equation. This is necessary in structures which have thick intrinsic regions or high background doping. In this case it is possible to use the capacitance-voltage characteristic of a device to infer the depletion width as a function of bias voltage. This can be used as the W term in equation 3.10, which maintains the validity of the equation in a device with multiple regions of different doping concentrations. The quantities involved in this calculation are illustrated diagrammatically in figure 3.3.

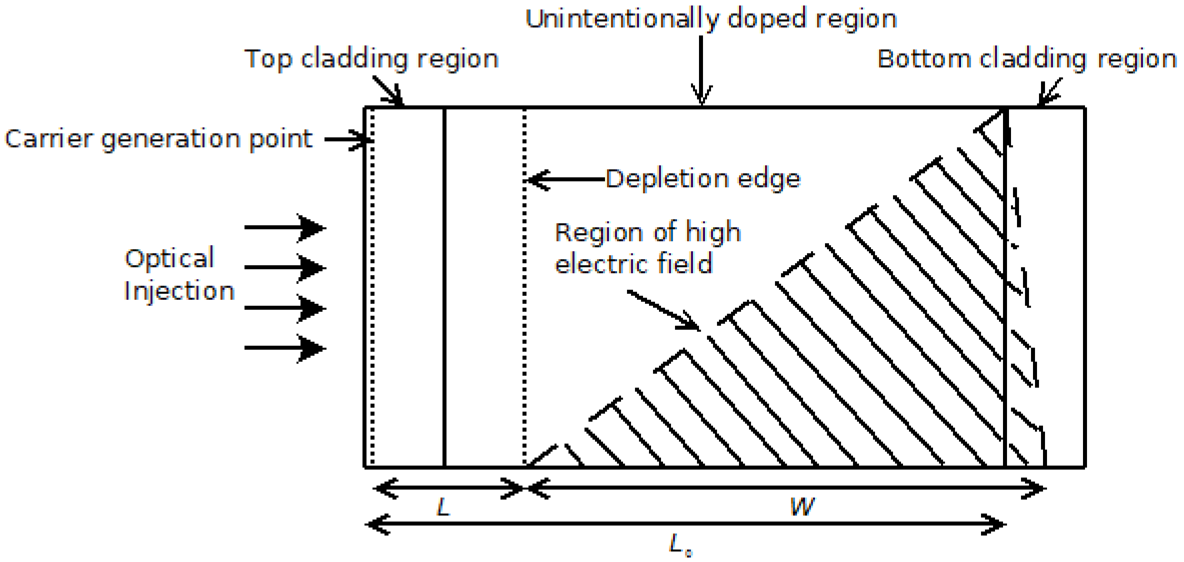

Figure 3.3: Diagram showing a partially depleted PIN diode, with parameters used for Woods equation calculation labelled.

The distance from the carrier injection point to the p-n junction is used as L_0, and G_0 and L_{pn} are used as fitting parameters to fit the calculated primary photocurrent to the initial part of the measured photocurrent characteristic, where impact ionisation is not occurring. This method relies on assuming that all optical absorption occurs close to the edge of the device, and the light of the shortest possible wavelength must be used to ensure that this is approximately correct. This means that it is not possible to calculate the primary photocurrent for mixed carrier injection conditions using this method. The photocurrent signal will also be reduced due to carrier recombination, resulting in reduced measurement accuracy at low gain. Depending on the structure and region dopings of the device, it may be necessary to neglect depletion into one of the cladding layers. This assumption can only be used if the doping of the cladding layer in question is sufficiently high. The caveats involved in calculating the primary photocurrent in this way emphasise that it is preferable to infer I_{pr} empirically from the data if possible.

3.7 Excess noise measurement

3.7.1 System after Li

The system used for the majority of the excess noise measurements in this work is based on that developed by Li [110] and reported on by Lau *et al.* [111]. The light signal on the device is modulated by a mechanical chopper or by electronic control at a frequency of 180Hz. A transimpedance amplifier (TIA) based on the AD9631A op-amp is used to convert the APD current into a voltage.

This voltage signal is then amplified using an initial gain stage, which for the measurements in this work was either a commercial voltage amplifier (Minicircuits ZFL-1000LN+) or an op-amp based amplifier using an LMH6624 configured with an inverting voltage gain of 24. The signal is then passed through a precision stepped attenuator, which prevents saturation of any of the amplification components when the noise signal is high. The noise component of the signal is then separated from the low-frequency photocurrent using a Minicircuits SBP-10.7 +LC 1 band-pass filter, which has a centre frequency of 10MHz and a bandwidth of 4.2MHz. It then goes through further amplification stages, which for the measurements in this work consisted of a Minicircuits ZFL-1000LN+ voltage amplifier and an op-amp based amplifier using an OPA695 configured with an inverting voltage gain of 120. The amplified signal is then passed through squaring and averaging circuit which produces a DC output proportional to the noise power in the pass band of the filter, acting as a power meter. The squaring circuit is based on an AD834 analogue multiplier, and the averaging circuit is a first order RC filter with a time constant of approximately 100us.

The output of this circuit is fed into an SR830 lock-in amplifier with a reference provided by the chopper controller or electronic modulator. The TIA output is also measured directly by a second lock-in amplifier, which is also fed a reference signal from the optical modulator, to give a reading for photocurrent. The voltage signal measured by the lock-in is related to current by the feedback resistance value of the TIA, which is 2.2kΩ. This means that 1µA of photocurrent is represented by a voltage output of 2.2mV. The feedback resistor value is selected to give the highest possible transimpedance gain without limiting the circuit bandwidth. The transimpedance gain of the op-amp is frequency dependent, and will be halved by the 50Ω termination at the output of the TIA stage. The effective transimpedance gain of the TIA at 10MHz is given by Li as 788 [110]. The relationship between the voltage signal output of the noise power lock-in amplifier and the actual noise power will vary slightly depending on fluctuations the overall system gain, and this must be regularly calibrated for as described below. As excess noise factor represents a ratio of quantities, the voltage readings for photocurrent and noise power can generally be considered as representative arbitrary units. A diagram of the measurement setup is shown in figure 3.4.

LEDs and He-Ne lasers were used to illuminate devices for excess noise measurement. Excess noise measurement with semiconductor lasers is not generally possible due to their associated random intensity noise. LEDs are considered preferable to He-Ne lasers as they provide a more stable output, which increases the precision of the measurement. He-Ne lasers were used for some measurements in this work, when increased optical power density was required. This is generally in cases where the device under test has poor responsivity at the desired wavelength. All optical signals were modulated at a frequency of 180Hz. LEDs were modulated using a digital waveform generator and lasers were modulated using a mechanical chopper.

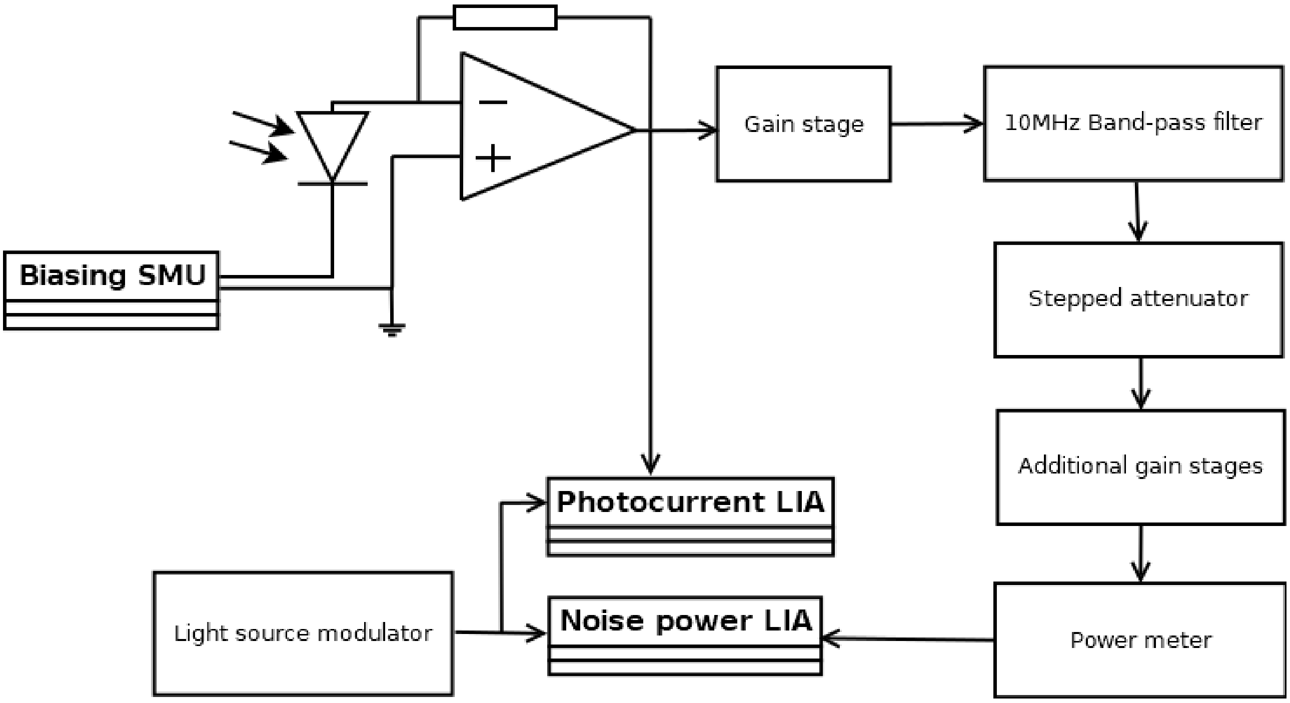

Figure 3.4: Diagram showing excess noise measurement setup after Li.

3.7.2 Noise setup calibrations

Excess noise factor is determined from the noise power data by using a commercial PIN photodiode as a reference. The noise developed by a PIN diode should be shot noise only and directly proportional to the photocurrent. The photocurrent through the reference device is controlled by varying the amplitude of the optical input signal. Any PIN diode may be used as shot noise is a function of photocurrent only at a given bandwidth. In this work, shot noise calibrations were performed with either a BPX65 or SFH2701 silicon PIN photodiode. Several calibration characteristics are shown in figure 3.5:

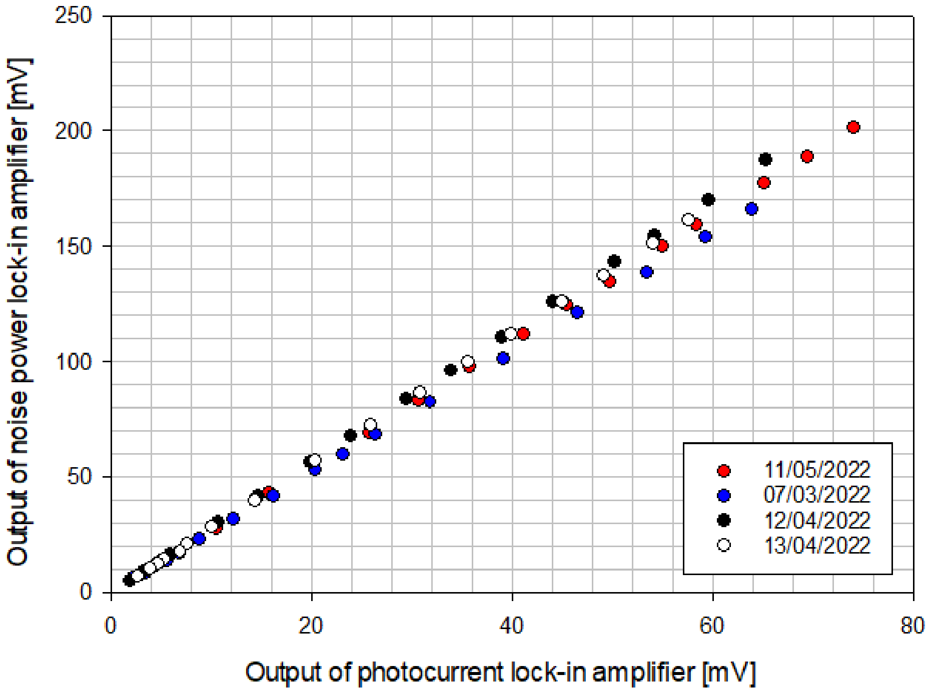

Figure 3.5: Shot noise characteristics used for noise setup calibration. The reference device used was an SFH2701 silicon PIN photodiode.

The shot noise data are regressed and the gradient of the line is used to give a value of shot noise per unit photocurrent, which is referred to as k_{ref}. It can be observed that there is some variation in the calibration characteristics. This results from a change in the overall gain of the system, which may be due to variations in temperature. It is therefore necessary to perform a shot noise calibration immediately before or after an important measurement in order to ensure accuracy.

For an APD with excess noise factor F, the measured noise power output is given by equation 3.11.

$$N_{APD} = 2qI_{pr}FM^2B \quad (3.11)$$

Where q is the electronic charge and B is the measurement bandwidth. This can be rearranged to give equation 3.12:

$$F = \frac{N_{APD}}{2qI_{pr}M^2B} \quad (3.12)$$

The denominator of equation 3.12 is equivalent to the diode shot noise multiplied by the square of the avalanche gain. This can therefore be simplified to equation 3.13:

$$F = \frac{N_{APD}}{I_{pr}k_{ref}M^2} \qquad (3.13)$$

This requires further refinement as the frequency dependent gain of the transimpedance amplifier will vary slightly with device capacitance. This dependence is characterised in Hz as effective noise bandwidth (ENBW), a function of capacitance which is calibrated for by using a network analyser to measure the frequency response of the TIA with different capacitances at the input. This is incorporated as shown in equation 3.14:

$$F = \frac{N_{APD}B(C_{\mathrm{APD}})}{I_{pr}k_{ref}M^2B(C_{ref})} \qquad (3.14)$$

Where B is the ENBW as a function of capacitance, C_{APD} is the capacitance of the APD under test, and C_{ref} is the capacitance of the reference device used for the shot noise calibration. The photocurrent signal is taken from the output of the TIA, which provides a 180Hz square wave proportional to the device photocurrent. This signal is measured using a second lock-in amplifier. This is used to calculate multiplication as described above.

The change in the frequency response of the system with device capacitance is shown in figure 3.6. This shows the relative gain of the TIA stage, first gain stage, and the band-pass filter. The first gain stage is incorporated in the calibration as it is built into the same PCB as the TIA stage. To perform the calibration, a resistor chain PCB is soldered onto the input of the TIA to simulate a diode. Capacitors of different values are soldered onto the PCB to simulate varying junction capacitance and the frequency response is measured using a network analyser.

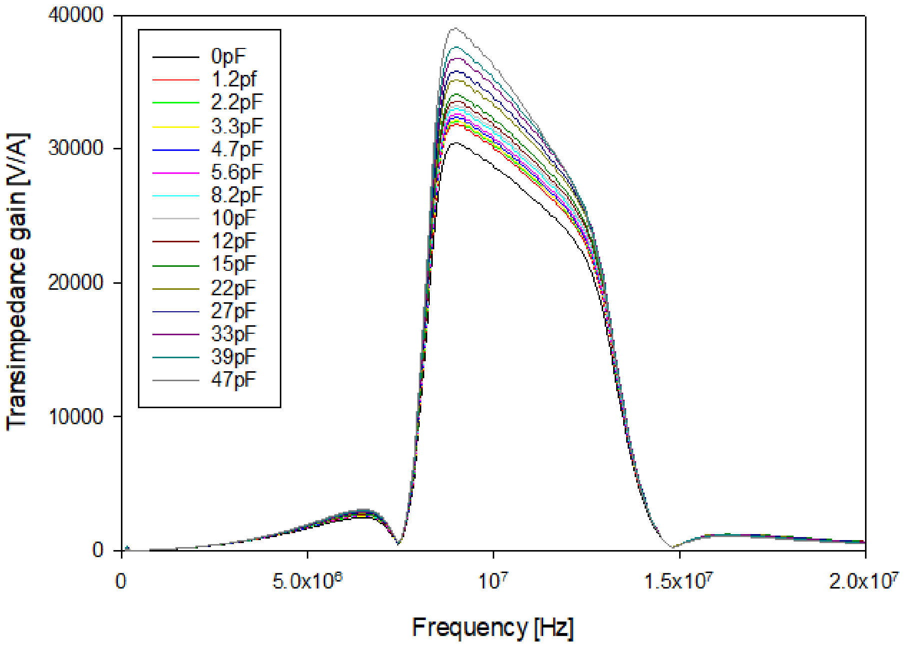

Figure 3.6: Measured relative frequency response of the TIA, first gain stage, and 10MHz band pass filter in series with varying capacitance at the TIA input.

The ENBW for each capacitance is calculated by normalising the area of the gain-frequency characteristic to the gain at 10MHz with a capacitance of 0pF. ENBW is shown as a function of junction capacitance in figure 3.7. This was fitted linearly to give an expression for ENBW, shown in equation 3.15:

$$ENBW(C_j) = 42290C_j + 4558428 \quad (3.15)$$

Where C_j is junction capacitance in pF and ENBW is in Hz.

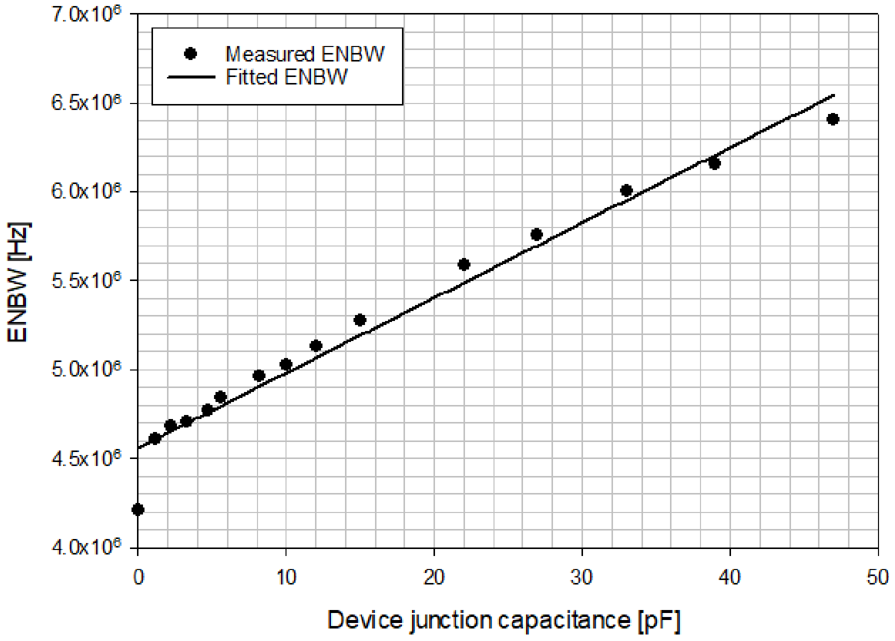

Figure 3.7: Measured and fitted ENBW as a function of device junction capacitance.

3.7.3 Limits of the system after Li

The noise floor of the system is reached when the lock-in amplifier can no longer extract the noise power signal from the system noise. The noise signal to noise ratio (NSNR) of this system can be approximated from the specifications of the AD9631 operational amplifier, on which the TIA is based, and was calculated by Li as -25.7dB [110], [112]. The voltage noise, V_n, of the AD9631 is given as 7nVHz$^{-1/2}$. A simple approximate calculation of the NSNR of this system is given in equation 3.16, assuming full shot noise at a photocurrent of 1µA:

$$NSNR = 20\log\left(\frac{788\sqrt{2qI_{ph}}}{V_n}\right) = -23.92\text{dB} \ (3.16)$$

In practice, the precise limit is difficult to quantify as it varies dependent on the noise introduced by the electromagnetic characteristics of the surrounding environment. Under normal experimental conditions, the shot noise developed by 0.5-1uA represents the lower limit of what is measurable using this system. The maximum device junction capacitance is 28pf, beyond which the change in ENBW cannot be effectively corrected for [110].

3.7.4 System after Qiao

For excess noise measurement at photocurrents below the limits of the Li system, the circuit of Qiao *et al.* [113] is used. This is necessary for devices with low responsivity, and also permits the use of light sources with a lower optical power density for device illumination. This system was used for the measurements of $(Al_xGa_{1-x})_{0.52}In_{0.48}P$ structures in chapter 4.

The system is based on the Li system, but the transimpedance amplifier is based on the OPA656 op-amp. It can measure shot noise on photocurrents as low as 10nA. The maximum tolerated junction capacitance is slightly lower than the Li system, at approximately 22pf. This system also operates with a centre frequency of 1MHz rather than 10MHz, which can be problematic due to higher background electromagnetic activity in this range. The gain stages are a Minicircuits ZFL-500LN+ and an op-amp based circuit using an AD829. Between these stages are a stepped attenuator and a cascade of single tuned Friend band-pass filters with a centre frequency of 1MHz and a bandwidth of 0.2MHz. The power meter circuit is identical to that used in the Li system.

3.8 Possible sources of error in excess noise measurement

3.8.1 Calibration and accurate calculation of primary photocurrent

The excess noise measurement is highly sensitive to a number of factors, all of which must be accounted for in order to obtain accurate data. The first and most critical is ensuring that the setup is appropriately calibrated – figure 3.5 shows that the variation in system gain can be significant, and using an incorrect calibration result may result of errors in data of 20% or more. As stated above, it is crucial to perform a calibration immediately before or after a measurement if the data is to be used for anything more than a rough approximation.

Also critical is accurate determination of primary photocurrent. It is not unusual for gain to be calculated on the assumption that the primary photocurrent does not increase further once the intrinsic region of a device is fully depleted. In this case a single data point from the photocurrent characteristic, at a bias voltage where the intrinsic region is fully depleted but impact ionisation has not started, is selected and used as a 'unity-gain value.' Figures 3.8-3.10 show photocurrent and multiplication data for a PIN structure (PIN851 in chapter 5), with gain calculated using both this method and a linear approximation to the Woods equation:

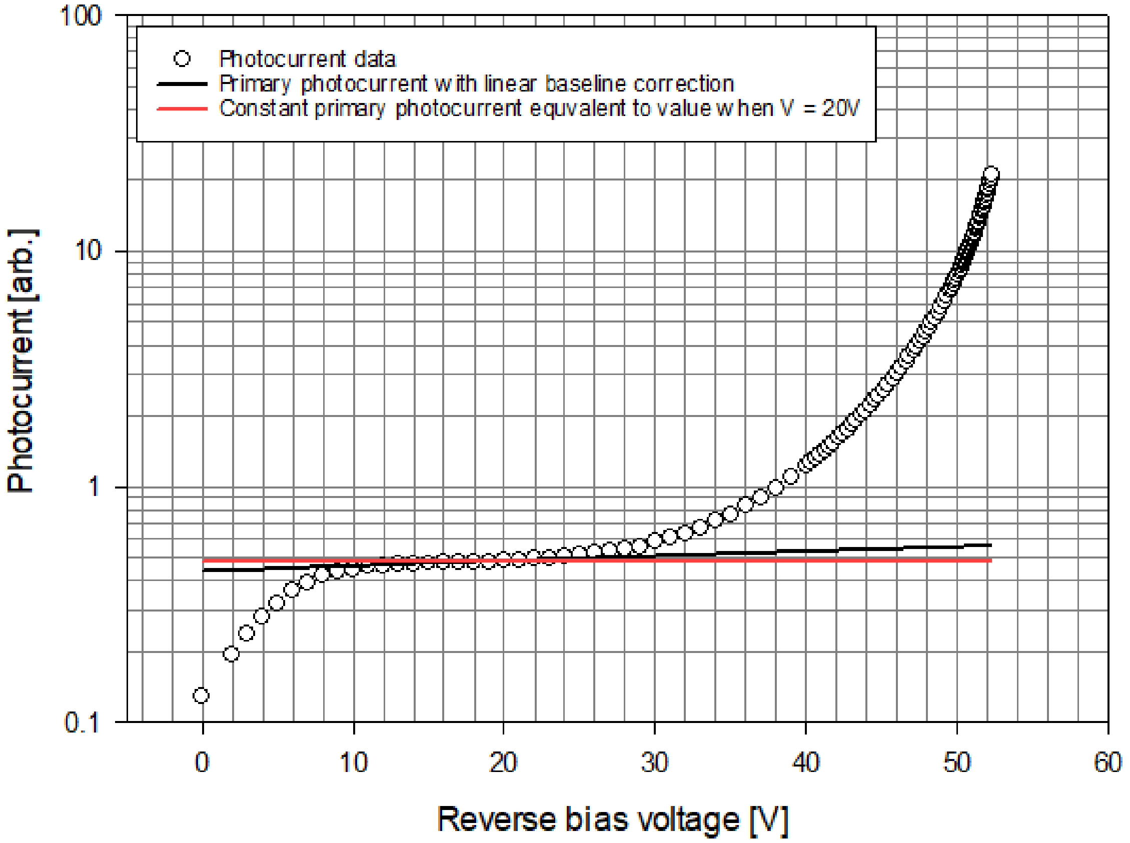

Figure 3.8: Photocurrent-voltage characteristic for a PIN APD structure (PIN851) shown with a primary photocurrent calculated using a linear baseline and a primary photocurrent calculated by normalising to a fixed unity gain point.

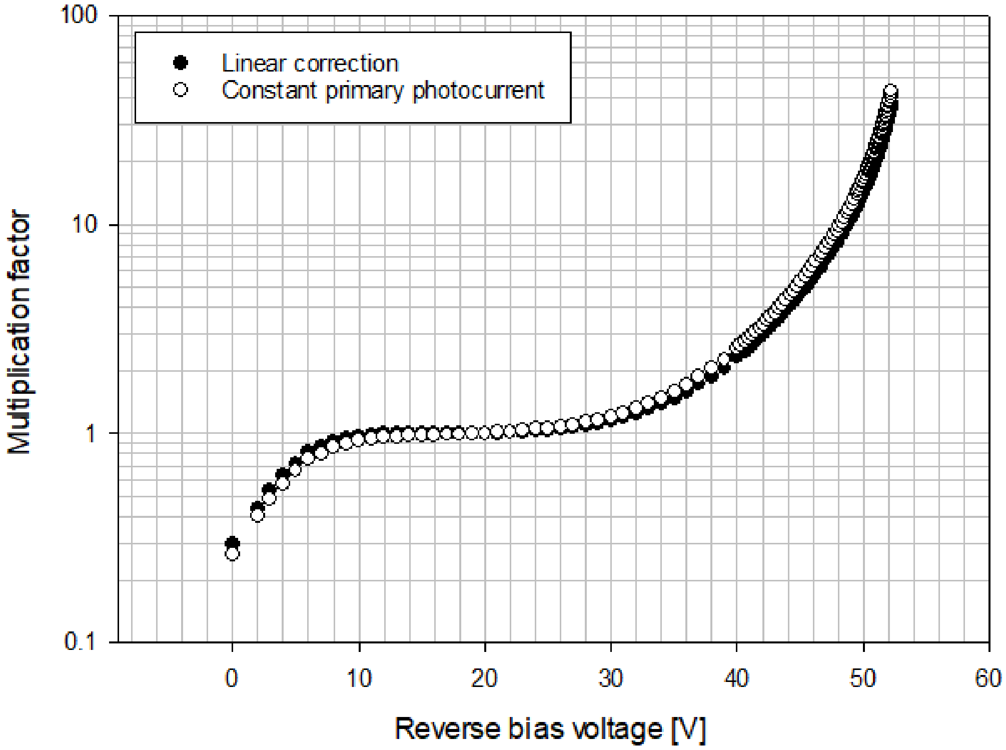

Figure 3.9: Multiplication characteristics for a PIN APD structure (PIN851) showing the multiplication calculated using a linear baseline primary photocurrent and that calculated using a primary photocurrent resulting from normalisation to a fixed unity gain point.

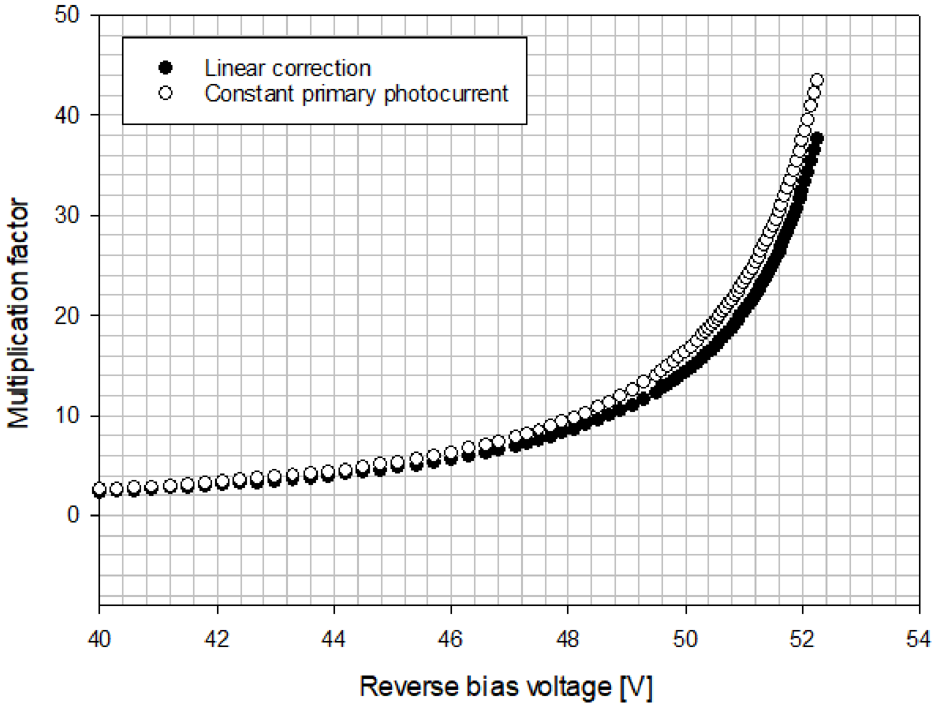

Figure 3.10: Multiplication characteristics for a PIN APD structure (PIN851) showing the multiplication calculated using a linear baseline primary photocurrent and that calculated using a primary photocurrent resulting from normalisation to a fixed unity gain point, scaled to show values from 40-54V.

The change in calculated multiplication is small, and the approximation of a constant photocurrent may be considered acceptable if the end purpose of the experiment is to measure gain. However, it can be observed that the multiplication values deviate non-negligibly as the device approaches breakdown. The effect of this on calculated excess noise factor can be seen in figure 3.11:

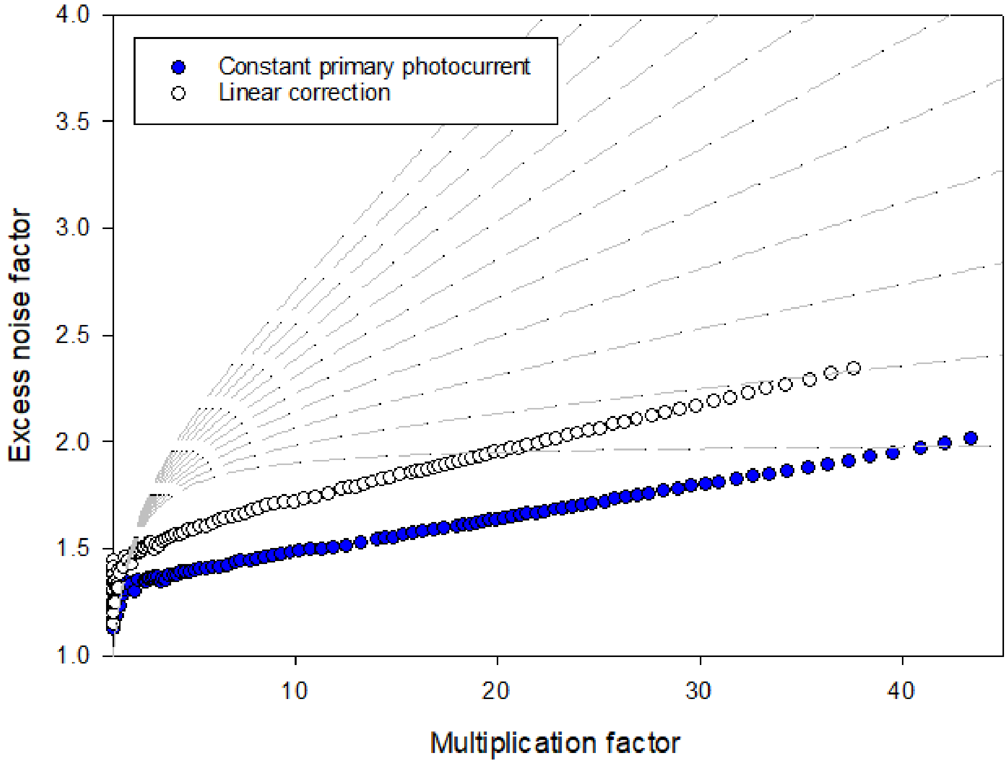

Figure 3.11: Excess noise characteristics for a PIN APD structure (PIN851) showing the excess noise factor calculated using a linear baseline primary photocurrent and that calculated using a primary photocurrent resulting from normalisation to a fixed unity gain point.

This change is observably significant. It is notable that the calculated excess noise factor for a constant primary photocurrent is entirely dependent on the value selected as the unity gain point – this means that any error in this data point will have a significant effect. Error in photocurrent measurement around the unity gain point may also be more likely as the photocurrent signal at this point will be weak compared to that in the presence of significant avalanche gain. It should therefore be considered critical to use an accurate regression of data points to infer an accurate value of primary photocurrent across the full range of bias voltages. It is important to note that, in some cases, primary photocurrent will not increase with bias past a certain point – this will be true in a SAM structure where optical absorption occurs separately in a dedicated device region, or in a device where the doping in the cladding layers is sufficiently high that any increase in collection efficiency due to their depleting is genuinely negligible. However, in these cases, it is still necessary to calculate primary photocurrent by averaging several data points, to reduce the error associated with using a single data point.

3.8.2 Effects of series resistance

High device series resistance may also affect excess noise measurement as it can limit the bandwidth of the diode by increasing the RC time constant [114]. If the bandwidth is sufficiently reduced that signals around the 10MHz centre frequency of the measurement are attenuated, the measured noise power will be suppressed. This effect will be more significant in devices with high capacitance. If the capacitance and series resistance of a device are known precisely, it is possible to calibrate for the effects of this reduction in bandwidth. However, due to the difficulty in determining the series resistance of a device to a high degree of precision, it is preferable to use devices with low series resistance where possible. Depending on the variation in series resistance in device size, this effect may be avoided by measuring a smaller device with lower capacitance. Variation in measured excess noise factor due to series resistance is illustrated in figures 3.12 and 3.13, which show forward IV curves and measured excess noise factor for two different fabrication rounds of an $Al_{0.85}Ga_{0.15}As_{0.56}Sb_{0.44}$ PIN structure (PIN852 in chapter 5), one of which had high contact resistance. It can be seen from figure 3.13 that the apparent excess noise factor of the high-series resistance sample is significantly suppressed.

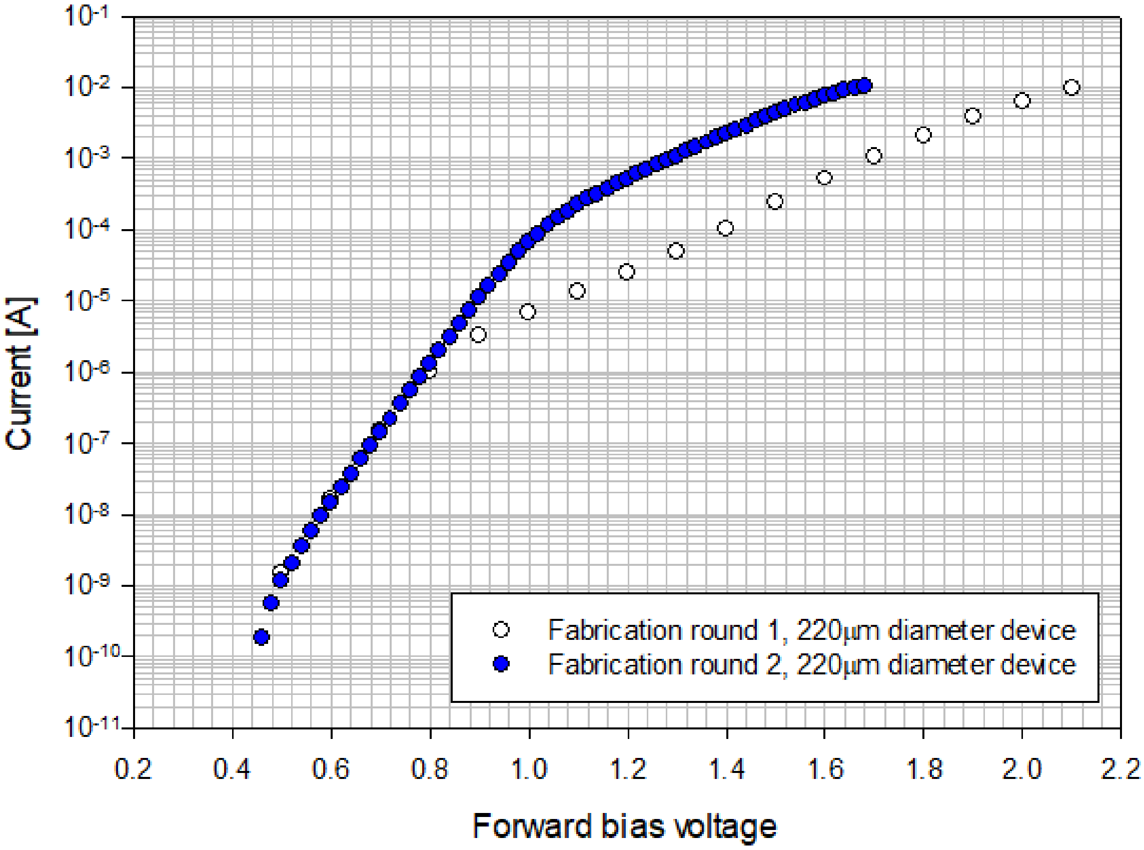

Figure 3.12: Forward current-voltage characteristics for two different fabrication rounds of a PIN APD structure (PIN852), indicating high series resistance for fabrication round 2.

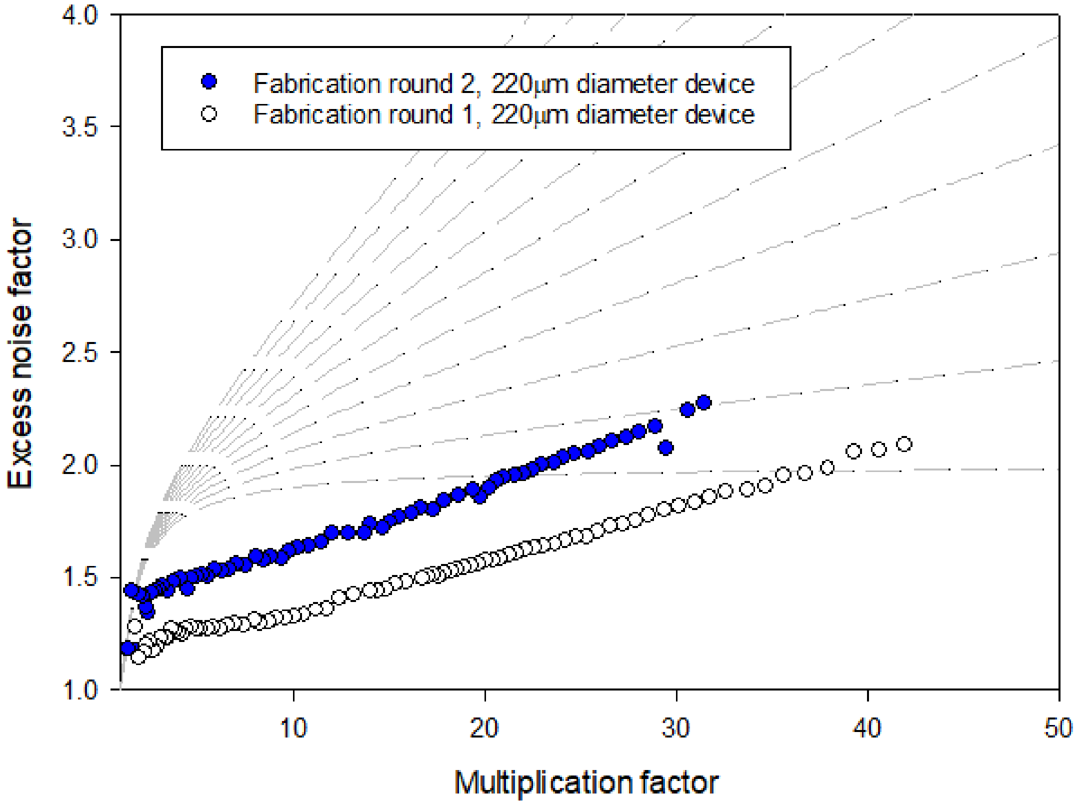

Figure 3.13: Excess noise characteristics for devices of each of the two fabrication rounds detailed in figure 3.12.

3.9 Summary

This chapter has described the methods used to fabricate and characterise the APDs in this work. In summary, mesa structure APDs were fabricated using standard photolithography and wet etching techniques. Basic electrical characterisation, incorporating I-V and C-V measurements, is used to determine the basic parameters of the devices and the wafer. A photocurrent spectrum measurement can be used to determine the optical characteristics of the semiconductor and provides information about the minimum band-gap. APD-specific measurements of multiplication and excess noise can be used to determine the impact ionisation characteristics of the devices and the material. Care must be taken when performing these measurements, and in processing the data, to ensure accuracy.

Chapter 4: Impact ionisation coefficients in $(Al_xGa_{1-x})_{0.52}In_{0.48}P$

4.1 Introduction

The objective of this chapter is to study the change in the ionisation coefficients of $(Al_xGa_{1-x})_{0.52}In_{0.48}P$ (referred to hereafter as AlGaInP) with alloy composition. It presents experimentally determined impact ionisation coefficients across the full composition range of the alloy system. These coefficients have been extracted using an RPL model from excess noise and photomultiplication data for a series of seven PIN diodes with different compositions. AlGaInP is notable for having the widest band-gap of any alloy system that can be grown lattice-matched to GaAs, at 2.2eV when $x = 1$. This is the largest band-gap of any non-nitride III-V alloy. Devices which incorporate wider band-gap alloys can operate at higher powers and with reduced leakage currents [115]. Reducing the aluminium content reduces the band-gap, to a minimum of 1.8eV when $x = 0$ [116]. The band-gap is direct at low aluminium concentrations but becomes indirect when $x \geq 0.48$ [117], with the lowest conduction band edge in the X valley. This occurs because the Γ energy gap increases with aluminium concentration while the X energy gap remains constant [117].The impact ionisation coefficients have been compared with those of $Al_xGa_{1-x}As$ (referred to hereafter as AlGaAs) and found to change similarly with varying alloy composition.

4.2 Motivations

Currently, AlGaInP is widely used in high-brightness red, orange, and yellow LEDs, being the only direct band-gap semiconductor suitable for operating at these wavelengths. AlGaInP LEDs with efficiency greater than 50% were developed in the 1990's, replacing inefficient indirect band-gap alternatives [118]. They now replace conventional lamps in a wide range of lighting and signing applications. The wide band-gap of AlGaInP also makes it an attractive material for the top sub-cell of multi-junction solar cells. The efficiency of current-generation 3-4 junction cells is approaching practical limits, necessitating the development of top-cells which can absorb at shorter wavelengths. Current development is promising, and it has been reported that multi-junction cells incorporating AlGaInP have the capacity to have efficiencies higher than 50% [119]. The absorption coefficients of AlGaInP have been comprehensively reported across the composition range [117]. Avalanche breakdown is a mechanism of failure in solar cells, particularly in cases where one cell in a chain fails or becomes 'shadowed [120].'A comprehensive understanding of the impact ionisation characteristics of this alloy is therefore useful for the design of robust solar cells.

AlGaInP has also been investigated as a material for optical detection. AlInP APDs have been reported for use as blue-green detectors, which may be useful for underwater communications. In this application the narrow absorption band removes the need for optical filters, which provides a further advantage [121]. This is achieved because the short minority carrier length in aluminium-containing alloys means that carriers produced by short-wavelength light will recombine before being collected by the electric field and will therefore not contribute to avalanche multiplication. The tuneable band-gap of AlGaInP would allow for selective detection at a range of wavelengths. AlInP APDs have also been studied for high-temperature x-ray detection, as the impact ionisation properties of AlInP have been demonstrated to be very stable at high temperatures [104], [122]. This is attributed to its high alloy disorder potential, which increases alloy scattering rates and decreases the dominance of temperature dependent phonon scattering [104]. Intermediate compositions of AlGaInP will have higher disorder potential due to further mismatch of the sizes of the different group III atoms, and may display improved temperature stability over AlInP. This has been reported in AlGaAs, for which the optimal temperature stability occurs when $x = 0.6$ [123]. The temperature stability and extremely low dark currents seen in AlInP APDs are comparable to recently reported GaN devices [124], but with the advantage of being grown lattice-matched to GaAs. Temperature stability reduces the need for cooling systems, which are required for silicon APDs operating at high temperatures and increase the bulk, weight, and cost of a detector module [125].

From the perspective of infrared detection and optical communications, AlGaInP is of interest as a multiplication region material for GaAs-based SACM structures using GaNAsSb and GaSb absorption regions. These materials can absorb at up to 1.6μm, making them ideal for optical communications use [126], and heterojunction structures using GaAs and AlGaAs multiplication regions have been reported [127]. AlGaInP is a promising alternative to these materials as its wide indirect band-gap means that it can operate in thinner structures with negligible tunnelling current [99], which results in higher speed devices with reduced excess noise due to the effects of dead space. The bulk multiplication characteristics demonstrated by AlInP are not ideal for APD use due to its relatively narrow α/β ratio [128]. However, good performance has been demonstrated with thin multiplication regions in both PIN and SAM [121] structures, yielding noise equivalent to k values as 0.11 for a 40nm structure [128]. A GaAs-based optical communications APD would be extremely useful due to the very high technological maturity and low cost of GaAs substrates. In practice, the availability of low cost, high quality substrates is a highly significant factor in the eventual uptake of a technology. Current-generation InP-based SWIR APDs remain considerably more expensive than visible/NIR silicon APDs, in large part due to the high cost of InP substrates. Attempts have been made to avoid this problem using heteroepitaxy of InP on silicon substrates [129], [130], but this process is technically complex. GaAs substrates are available at lower cost and in larger wafer sizes than InP, and are more mechanically robust [131].

Although the majority of research into AlGaInP for optical detection has been focused on the ternary alloy AlInP, high-quality wafer growth of aluminium-containing alloys is made difficult by the strong affinity between aluminium and oxygen. Residual oxygen during growth leads to the formation of deep traps, reducing minority carrier lifetimes [132]. This is the mechanism responsible for the highly selective photoresponse of AlInP, but has a significant negative impact on the overall responsivity of minority carrier devices such as APDs and x-ray detectors. In AlGaInP, the number of deep-level traps caused by oxygen increases superlinearly with aluminium concentration, possibly by a factor of more than five between $x = 0.7$ and $x = 1$ [133]. Reducing aluminium content and decreasing the density of traps would improve responsivity, and the overall electrical quality of devices, but would reduce the selectivity of the photoresponse by increasing minority carrier lifetimes. In a heterojunction SACM structure with a narrower band-gap absorber, as would be used for infrared detection, the selectivity of the photoresponse would not be relevant and the priority would be on minimising the concentration of traps. Additionally, AlInP undergoes photoelectrochemical oxidation that is accelerated in the presence of light and heat, and this is particularly problematic for applications in rugged environments [134]. For these reasons it may be advantageous to replace AlInP with lower-aluminium AlGaInP alloys where possible, and even a small reduction in aluminium content may have a significant positive affect. A comprehensive study of the impact ionisation characteristics across the full composition range of the alloy system is therefore necessary.

4.3 Review of research into impact ionisation in $(Al_xGa_{1-x})_{0.52}In_{0.48}P$

Research into impact ionisation in AlGaInP has largely been limited to the ternary end-points of the alloy system. The impact ionisation coefficients for AlInP have been reported by Ong *et al.* [135]. It was found that the electron ionisation coefficient was greater than the hole ionisation coefficient, and the breakdown voltage was found to be 2.5 times larger than in GaAs. β/α was reported as 0.4 - 1.0 over the electric-field range of 400-1300 kV/cm, which is a relatively narrow ratio. The dark currents were also found to be very low, with less than 6nA cm^{-2} at 95% of breakdown voltage. No evidence of tunnelling current was evident, which means that it is possible to produce extremely thin AlInP APDs without the high dark currents normally associated with such structures. Cheong *et al.* reported an AlInP SAM-APD with extremely low dark current; 8nA cm^{-2} at 99.9% of the breakdown voltage [121]. The multiplication was accurately predicted using the previously established ionisation coefficients.

Excess noise data have been reported for AlInP PIN and NIP structures of varying thicknesses, and a SAM structure [128]. The relatively small difference between the electron and hole ionisation coefficients would be expected to yield poor excess noise performance, but the wide band-gap of

AlInP means that the effects of dead space become very significant in thinner structures. The SAM structure, which had a multiplication region thickness of 0.2um, was reported to have excess noise factor equivalent to an effective k of 0.3. The thinnest PIN structure, with a thickness of 0.04um, was reported to have excess noise factor equivalent to an effective k of 0.11, which is competitive with commercial silicon APDs. This indicates that thin AlInP structures would be a promising option for a low noise GaAs-based photodetector.

The impact ionisation coefficients of GaInP are also known, having been first reported by Fu *et al.* in 1995 [136] and later corroborated by Ghin *et al.*[137]. It was observed that β is greater than α, and that the β/α ratio converges to unity as breakdown is approached. Ghin *et al.* have also performed measurements on thin GaInP structures [138]. It was seen that breakdown voltage could be accurately modelled using the parameterised form of α and β in all but the thinnest structures. This implies that dead space effects do not significantly affect ionisation behaviour in GaInP.

Studies of across the full composition range have been limited to a 1996 work by David *et al.,* which measured the avalanche breakdown voltages of AlGaInP diodes with x = 0.24,0.5, and 0.7, and reported that the breakdown voltage increased linearly with x [139].

4.4 Wafer and device details

A series of homojunction PIN $(Al_xGa_{1-x})_{0.52}In_{0.48}P$ wafers with x = 0, 0.31, 0.47, 0.61, 0.64, 0.78 and 1 were grown by atmospheric pressure Metal-Organic Chemical Vapour Phase Epitaxy on 2" GaAs substrates. These are the same wafers which are described in [117]. Each wafer had a nominal intrinsic region thickness, w, of 1µm and p^+ and n^+ cladding layers of 1.0 and 0.3µm respectively. The wafers were capped with 50nm thick p^+ GaAs, to ensure a good ohmic contact, and were grown on n^+ GaAs substrates. Circular mesa diode structures with optical windows were fabricated at Sheffield on these wafers using standard photolithography and wet chemical etching. Device radii were between 35 and 210µm. The GaAs cap was removed by wet etching in the optical window regions. The mesa sidewalls were passivated with SU-8 and covered with gold to ensure that light could only enter the device through the top optical window. A schematic diagram of the wafer structures is shown in figure 4.1. The depletion region widths and the doping densities of each layer were obtained using capacitance-voltage measurements. Dielectric constants were interpolated from those of GaP, InP, and AlP [140],[141],[142]. The measurement results and model fits are shown in figure 4.4. The calculated region widths and dopings are shown in table 4.1.

TABLE 4.1

PARAMETERS OF $(AL_xGA_{1-x})_{0.52}IN_{0.48}P$ WAFERS USED IN THIS STUDY

Al fraction, x	Intrinsic region width, w [µm]	N_i [x10^{15}cm^{-3}] ± 1x10^{15}cm^{-3}	N_p [x10^{17}cm^{-3}] ± 1x10^{17}cm^{-3}
0	0.94	2	18
0.31	0.99	3.5	8
0.47	0.94	3	7.5
0.61	1.00	2	8
0.64	0.96	3.5	6
0.78	0.94	4.5	6
1	0.96	3	3.5

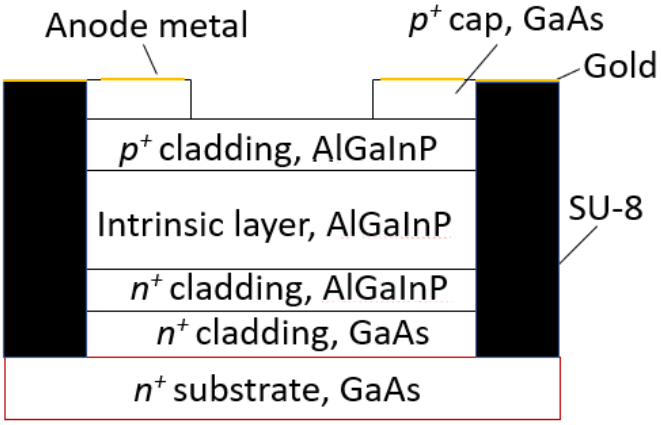

Figure 4.1: Schematic diagram of $(Al_xGa_{1-x})_{0.52}In_{0.48}P$ diodes used in this study.

4.5 Dark I-V and C-V measurements

4.5.1 Dark I-V measurements

Dark current-voltage measurements were performed using the method described in chapter 3. Reverse dark current-voltage data for each wafer are shown in figure 4.2. At 95% of breakdown voltage the reverse dark currents were below 1nA for all devices, except for the $x = 0$ wafer. The increase in dark current prior to avalanche breakdown is attributed to mid-band traps in the material, meaning that it is due to defects in the wafers we have measured rather than the bulk characteristics of each alloy. These traps are known to occur in AlGaInP [143]. Dark currents did not scale with device size and in some cases smaller devices exhibited higher dark currents, indicating that these traps occur non-uniformly in each wafer.

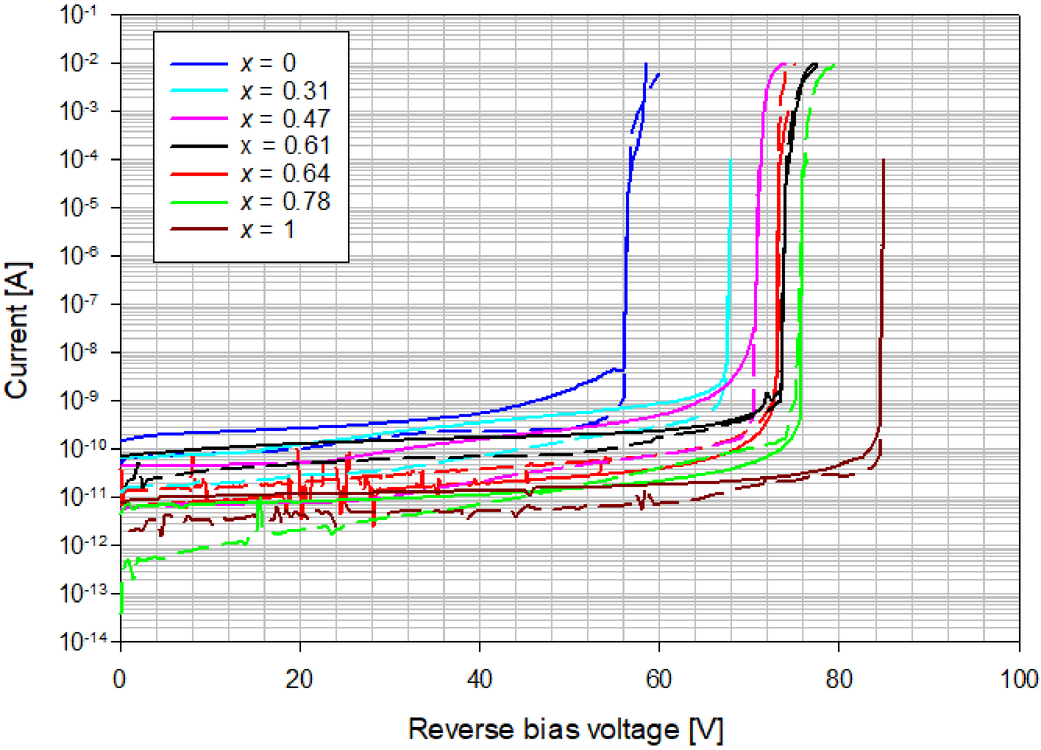

Figure 4.2: Reverse dark current characteristics for devices used in this study. Solid lines indicate 220µm diameter devices and dashed lines indicate 120µm diameter devices.

Forward dark current-voltage data for each wafer are shown in figure 4.3. This data indicates that the series resistance in these samples was of a sufficiently low order of magnitude to avoid distorting excess noise measurements by reducing the effective bandwidth of the measurement system, which would lead to error of the type discussed in section 3.8.2.

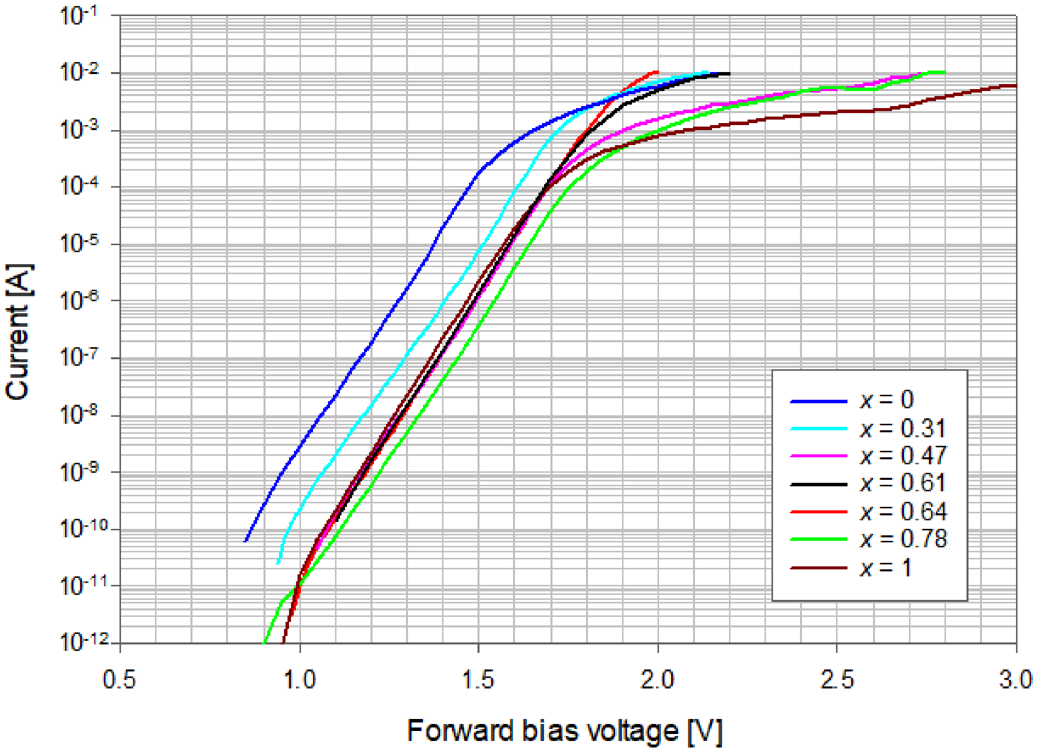

Figure 4.3: Forward dark current characteristics for devices used in this study. Data shown are for 220μm diameter devices.

4.5.2 C-V measurements

Capacitance-voltage data for each wafer are shown in figure 4.4, with model fits using the region widths and dopings shown in table 4.1.

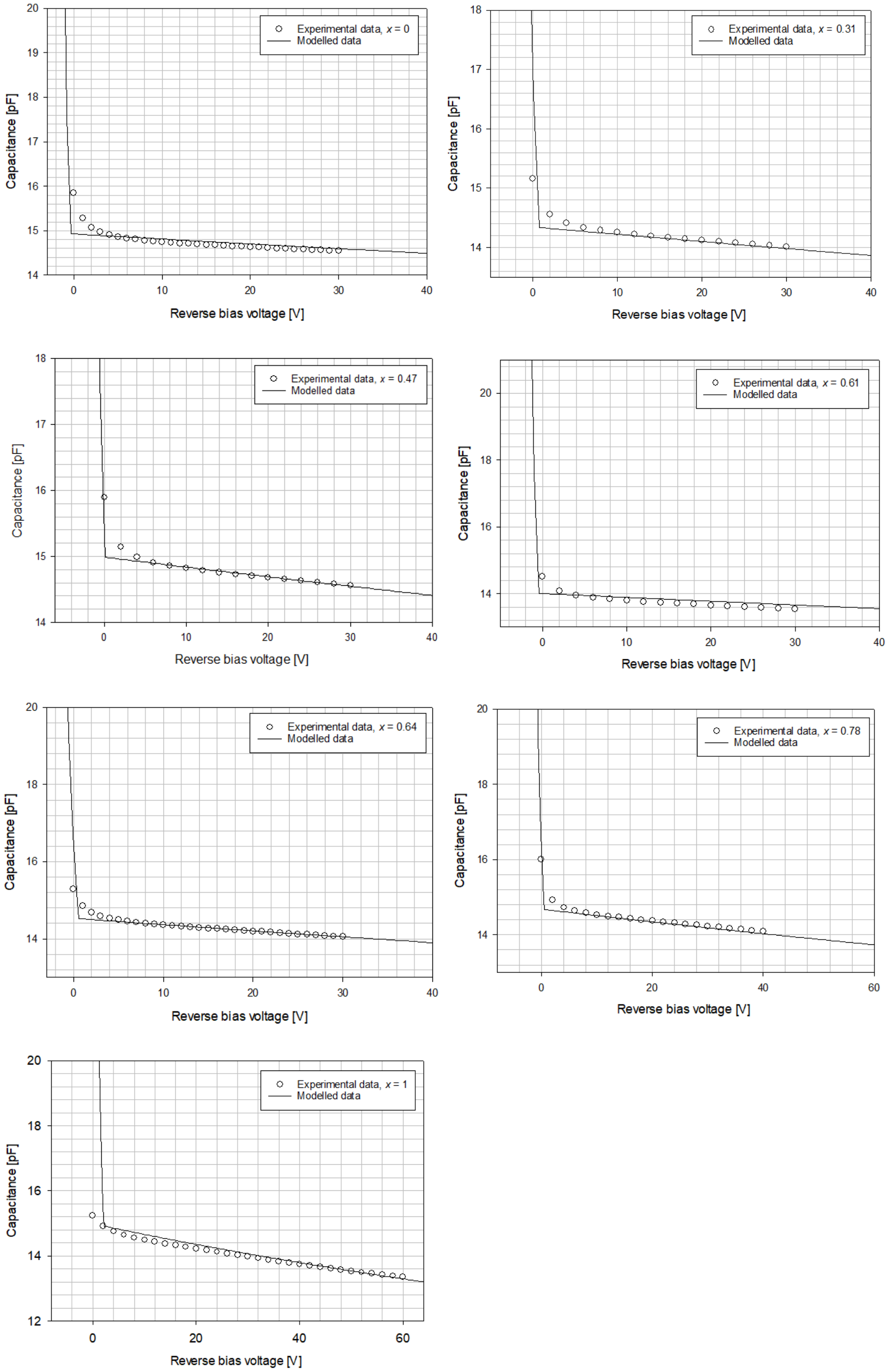

Figure 4.4: Reverse capacitance-voltage characteristics for each wafer used in this study, shown with modelled data using fitted region widths and dopings.

4.6 Multiplication measurements

The data used to extract the impact ionisation coefficients were taken under pure electron injection conditions. Multiplication data for these samples had been previously measured by Qiao [144] and these measurements were repeated for corroboration. Light sources were selected for each alloy such that ≥99.9% of photons were absorbed in the p^+ cladding of the devices, eliciting pure electron injection. If too long a wavelength is used and the absorption coefficient is too low, a significant proportion of the incident light will pass through the cladding to the intrinsic region of the device before being absorbed. However, if the wavelength used is too short and the absorption coefficient is too high, the photocurrent signal will be reduced because optically generated carriers will recombine before they diffuse far enough to be collected by the electric field. The sources used were a 430nm LED for $x = 1$, a 460nm LED for $x = 0.47$, 0.61, 0.64, and 0.78, and a 543nm laser for $x = 0.31$ and $x = 0$. Multiplication increases, and avalanche breakdown voltage decreases, with decreasing aluminium concentration, as is expected due to the narrower band-gap. Figure 4.5 shows multiplication data for each sample in the form M-1.

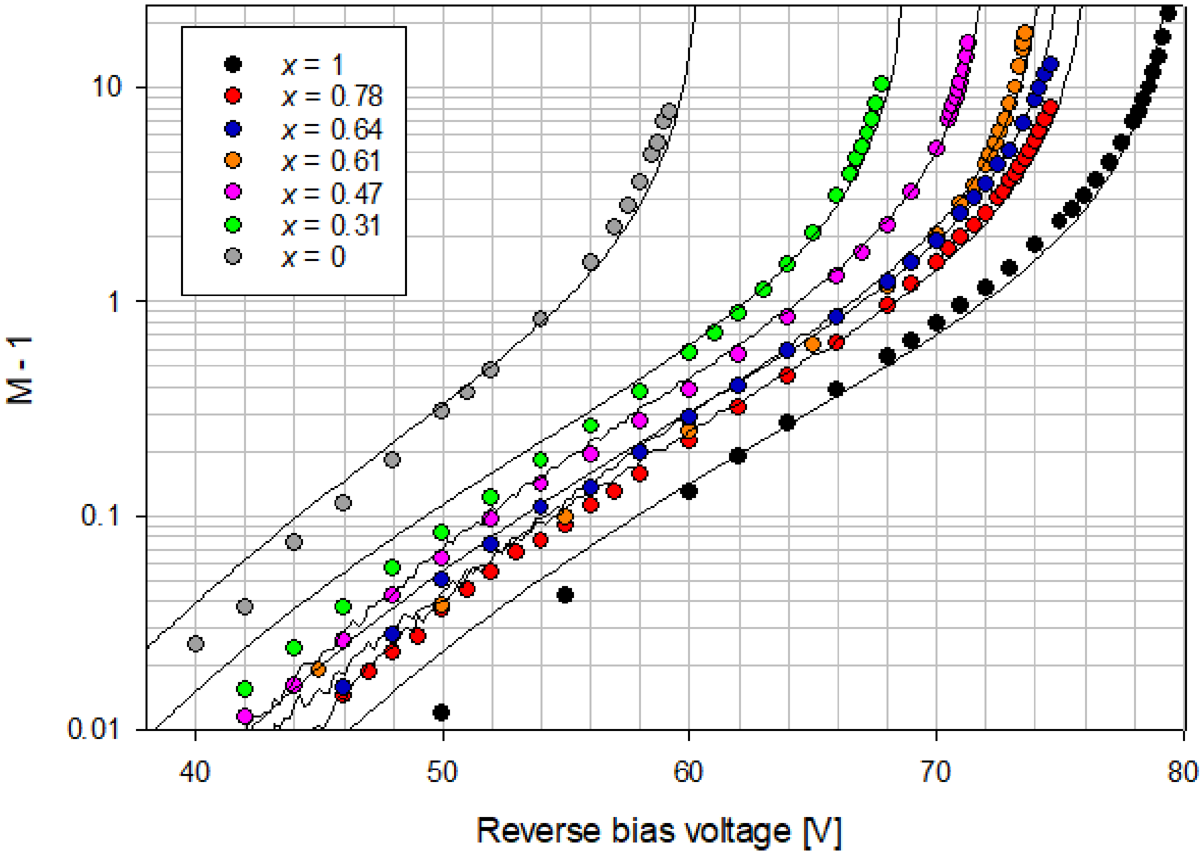

Figure 4.5 Multiplication data for each $(Al_xGa_{1-x})_{0.52}In_{0.48}P$ sample measured in this study, shown with data simulated by an RPL model using the fitted ionisation coefficients.

4.7 Excess noise measurements

Excess noise was measured using the low photocurrent noise measurement system of Qiao *et al.,* described in chapter 3. Noise data for these samples had been previously measured by Qiao [144] and these measurements were repeated for corroboration. Data are shown in figure 4.6, with simulated data for comparable GaAs and $Al_{0.8}Ga_{0.2}As$ shown for comparison. The excess noise reduces with increasing values of *x,* from an effective *k* of approximately 1 when $x = 0$ to approximately 0.5 when $x = 0.64$. Further increases in *x* do not decrease the noise further. The largest relative decrease occurs between $x = 0.61$ and $x = 0.64$, despite only a small change in composition.

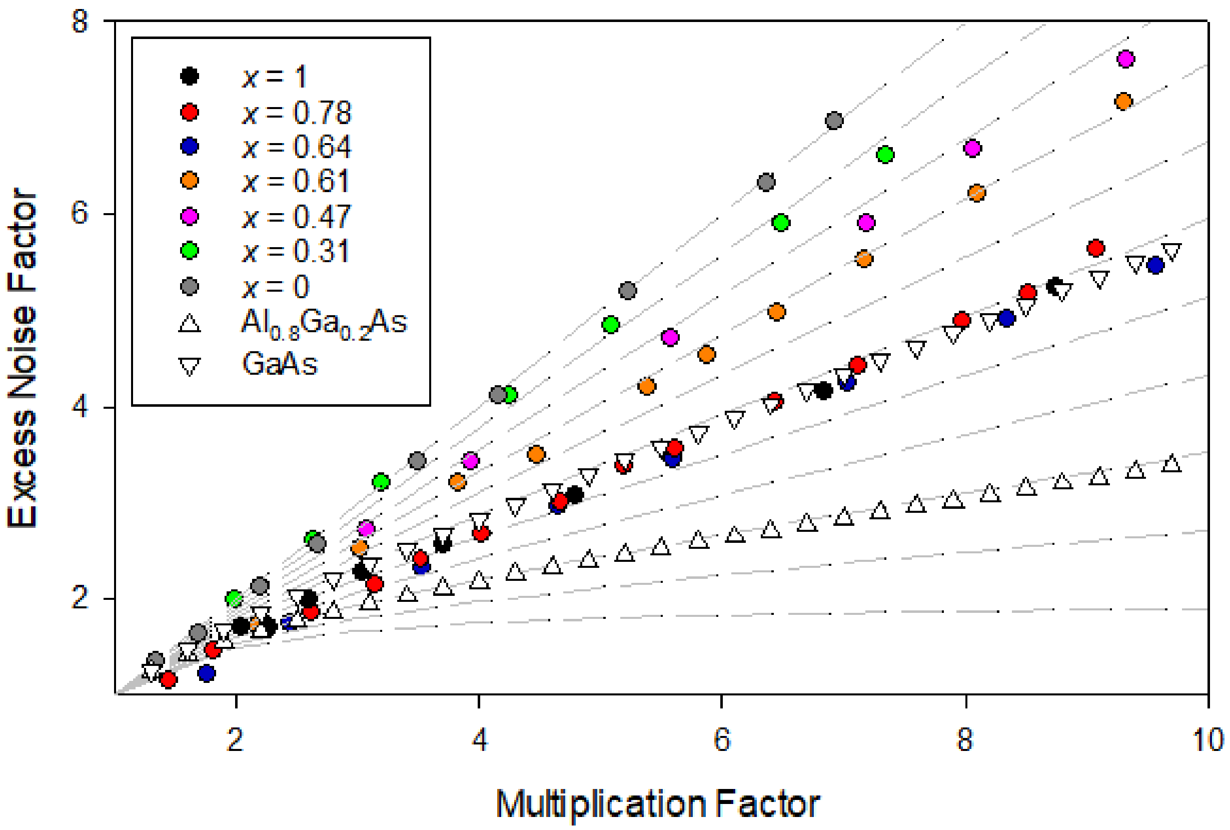

Figure 4.6: Excess noise factor versus M_e for several compositions of $(Al_XGa_{1\text{-}X})_{0.52}In_{0.48}P$. The lines represent Macintyre's ideal noise curves for effective k values of 0 – 1, in steps of 0.1. Simulated data for comparable GaAs (▽) and $Al_{0.8}Ga_{0.2}As$ (△) structures are included for comparison [145].

4.8 Impact ionisation coefficients

For a perfect PIN structure with no dead space, the electron and hole ionisation coefficients are related to the pure electron initiated multiplication (M_e) and the pure hole initiated multiplication (M_h) by equations 2.9 and 2.10, shown here as equations 4.1 and 4.2:

$$M_e = \frac{1}{1-\frac{\alpha}{\beta-\alpha}\{\exp[(\beta-\alpha)W_T]-1\}} \quad (4.1)$$

$$M_h = \frac{1}{1-\frac{\beta}{\alpha-\beta}\{\exp[(\alpha-\beta)W_T]-1\}} \quad (4.2)$$

If only one of M_e and M_h is available, then it is theoretically possible to infer the other by using noise data. This is done by using Macintyre's equations [2] to determine the effective β/α ratio, referred to as k. This means that it is possible to calculate both α and β analytically if multiplication and noise data are available for pure injection conditions of only one carrier type, as will be the case if either PIN structures only or NIP structures only are available. Only PIN structures were available in this case, so data were available only for the pure electron injection or mixed injection cases.

Some problems can arise if this method is used. The equations involved become significantly more complex if the structure used is not a perfect PIN structure, or closely approximate to one. A perfect PIN structure is here defined as being completely undoped in the intrinsic region and having infinite doping in the p^+ and n^+ cladding regions, so that the electric field is uniform throughout the intrinsic region and the depletion does not extend into the p^+ and n^+ regions. This is not a good approximation for the samples used here, where the doping in the intrinsic region was as high as $4.5 \text{x} 10^{15}$ for some structures and the p^+ doping as low as $3.5 \text{x} 10^{17}$. This means that there is significant non-uniformity in the electric field strength within the intrinsic region and that the depletion extends significantly into the cladding layers. Additionally, the wide band-gap of AlGaInP means that the dead space has a significant effect on multiplication and noise. This means that it is not possible to obtain accurate values of α and β using M_e and M_h using the standard local model equations. Moreover, it will not be possible to infer M_h from M_e, or vice versa, because Macintyre's equations will not accurately represent the relationship between the excess noise and the α/β ratio if non-local effects are significant. The limitations of the local model and the effects of dead space are described in more detail in chapter 2.

To account for these, values for α and β were determined empirically using a random path length (RPL) model. Approximate values, calculated using the local model method described above, were used a starting point. The model was then used to produce simulated multiplication and noise data, which was compared to the experimental data. This process was repeated iteratively using different values of α and β until the simulated data matched the experimental data. This was performed for each of the wafers to yield optimised values of α and β for each alloy composition. This method incorporates consideration of the details of each wafer structure, including the thicknesses and doping levels of each region and the ionisation threshold energies for each carrier type, which are determined by the band-gap and therefore vary with alloy composition.

The electron and hole ionisation threshold energies, E_{the} and E_{thh} respectively, for AlInP and GaInP are available in the literature [146]. It was assumed that the relationship between the threshold energies and the minimum energy band-gaps was the same in the intermediate alloys as in the ternary end-points. The threshold energy for each intermediate composition was approximated as 2.05 times the energy band-gap, using band-gap values reported by Cheong *et al.* [146]. It was assumed that the electron and hole ionisation threshold energies were the same, which is known to be true for AlInP and GaInP. The minimum energy band-gaps and inferred threshold energies are shown in table 4.2.

TABLE 4.2

ENERGY BAND-GAPS AND THRESHOLD ENERGIES FOR DIFFERENT COMPOSITIONS OF $(AL_XGA_{1-X})_{0.52}IN_{0.48}P$

Al fraction, x	Minimum energy band-gap, E_g [eV]	Ionisation threshold energy, E_{th} [eV]
0	1.90	4.05
0.31	2.12	4.35
0.47	2.23	4.57
0.61, 0.64, 0.78, 1	2.24	4.60

The optimised ionisation coefficients were determined as a function of electric field in the form of a simplified Chynoweth expression:

$$\alpha(\beta) = Aexp(-\frac{B}{\xi}) \quad (4.3)$$

Where ξ represents electric field, and A and B are constants. The simplified version of this expression was used so that the parameterised coefficients could be fitted as a function of alloy composition (quantified by the aluminium concentration, x) and represented by single unified equations for α and β. Once a set of optimised ionisation coefficients had been found for each alloy composition, another round of fitting was performed in order to find general equations for α and β in terms of aluminium concentration, x. A least squares regression algorithm was used to fit the array of functions for α and β, which were in terms of electric field only, to a single, more general equation for each ionisation coefficient in terms of both electric field and x.

Due to the disproportionately large change in both α and β between $x = 0.61$ and $x = 0.64$, the data were split into two ranges of $x \leq 0.61$ and $x > 0.61$. The equations found for α and β are given in equations 4.4-4.7:

$$\alpha = (5.91\mathrm{x}10^{6} - 1.12\mathrm{x}10^{5}x - 6.05\mathrm{x}10^{7}x^{2} + 1.14\mathrm{x}10^{8}x^{3})\exp\left(\frac{-4.16\mathrm{x}10^{6}+1.01\mathrm{x}10^{6}x-1.63\mathrm{x}10^{6}x^{2}-3.58\mathrm{x}10^{6}x^{3}}{\xi}\right)\ cm^{-1} \quad (4.4)$$

$$\beta = (4.43\mathrm{x}10^{6} + 4.98\mathrm{x}10^{7}x - 2.12\mathrm{x}10^{8}x^{2} + 2.23\mathrm{x}10^{8}x^{3})\exp\left(\frac{-3.86\mathrm{x}10^{6}-5.71\mathrm{x}10^{6}x+1.99\mathrm{x}10^{7}x^{2}-2.15\mathrm{x}10^{7}x^{3}}{\xi}\right)\ cm^{-1} \quad (4.5)$$

for $x \leq 0.61$, and

$$\alpha = (2.20\mathrm{x}10^{8} - 8.42\mathrm{x}10^{8}x + 1.09\mathrm{x}10^{9}x^{2} - 4.50\mathrm{x}10^{8}x^{3})\exp\left(\frac{8.26\mathrm{x}10^{6}-4.68\mathrm{x}10^{7}x+5.43\mathrm{x}10^{7}x^{2}-2.15\mathrm{x}10^{7}x^{3}}{\xi}\right)\ cm^{-1} \quad (4.6)$$

$$\beta = (8.88\mathrm{x}10^{8} - 3.87\mathrm{x}10^{9}x + 5.44\mathrm{x}10^{9}x^{2} - 2.39\mathrm{x}10^{9}x^{3})\exp\left(\frac{1.15\mathrm{x}10^{8}-4.43\mathrm{x}10^{8}x+5.35\mathrm{x}10^{8}x^{2}-2.14\mathrm{x}10^{8}x^{3}}{\xi}\right)\ cm^{-1} \quad (4.7)$$

for $x > 0.61$.

These general equations were verified by using the RPL model to ensure that the simulated multiplication and noise data for each composition matched the experimental data. It was found that the ionisation coefficients for AlInP and GaInP differed at low electric field values from those of Ong *et al.* [135] and Ghin *et al.* [137]. The RPL model produced nearly identical sets of simulated data using the previously reported coefficients and the new coefficients, suggesting that M_e and excess noise factor in these structures are insensitive to the values of α and β at low electric fields. This means that further experimental data, from thicker structures, which would operate at lower electric fields, may be required to verify that the ionisation coefficients are correct across the entire electric field range. The final impact ionisation coefficients are shown as a function of electric field in figure 4.7, and are shown as a function of aluminium concentration for various electric fields in figure 4.10. The electron and hole ionisation coefficients are shown on three-dimensional graphs as a function of inverse electric field and aluminium fraction in figures 4.8 and 4.9.

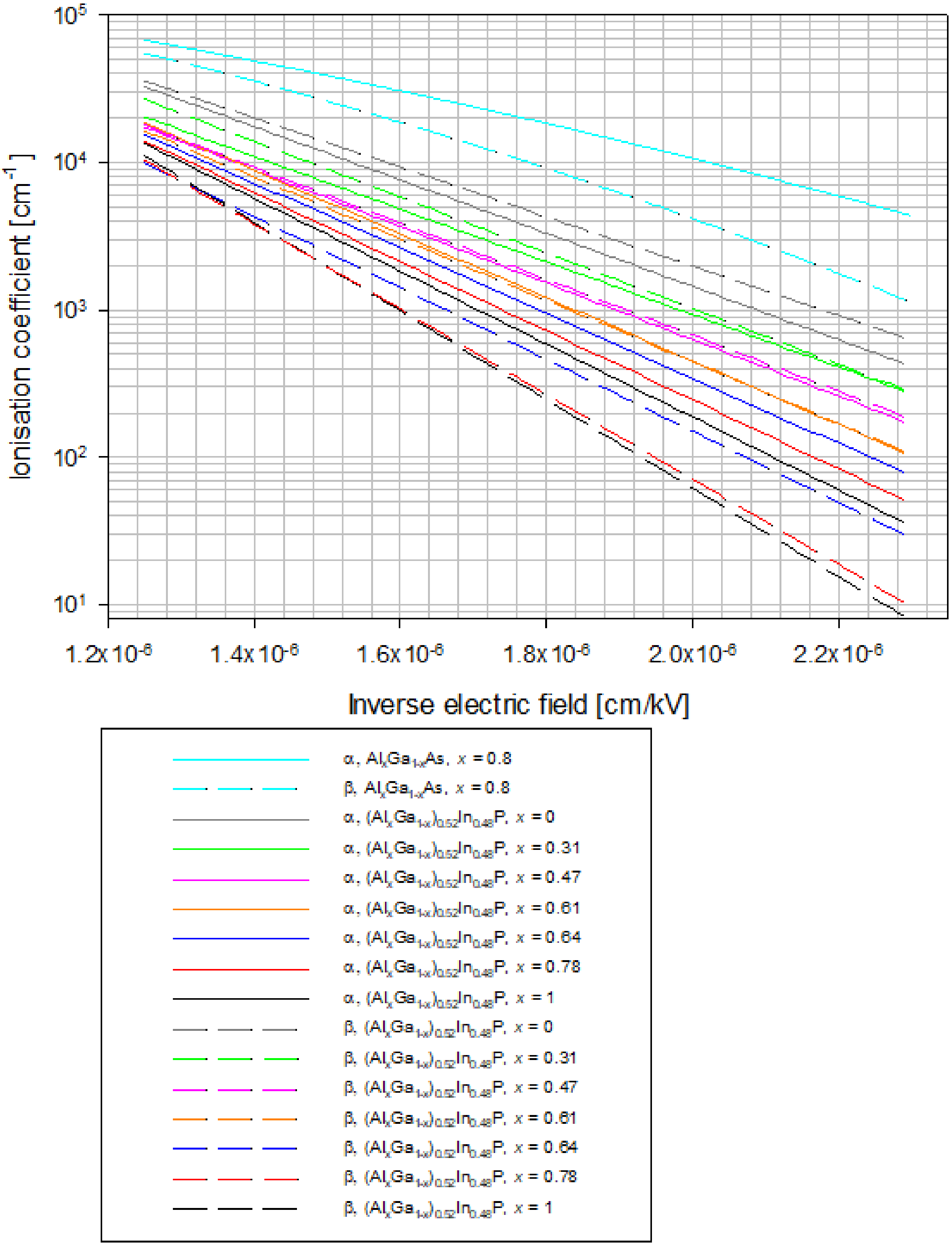

Fig. 4.7: Electron and hole ionisation coefficients for (Al$_X$Ga$_{1-X}$)$_{0.52}$In$_{0.48}$P, with data for Al$_{0.8}$Ga$_{0.2}$As included for comparison [145].

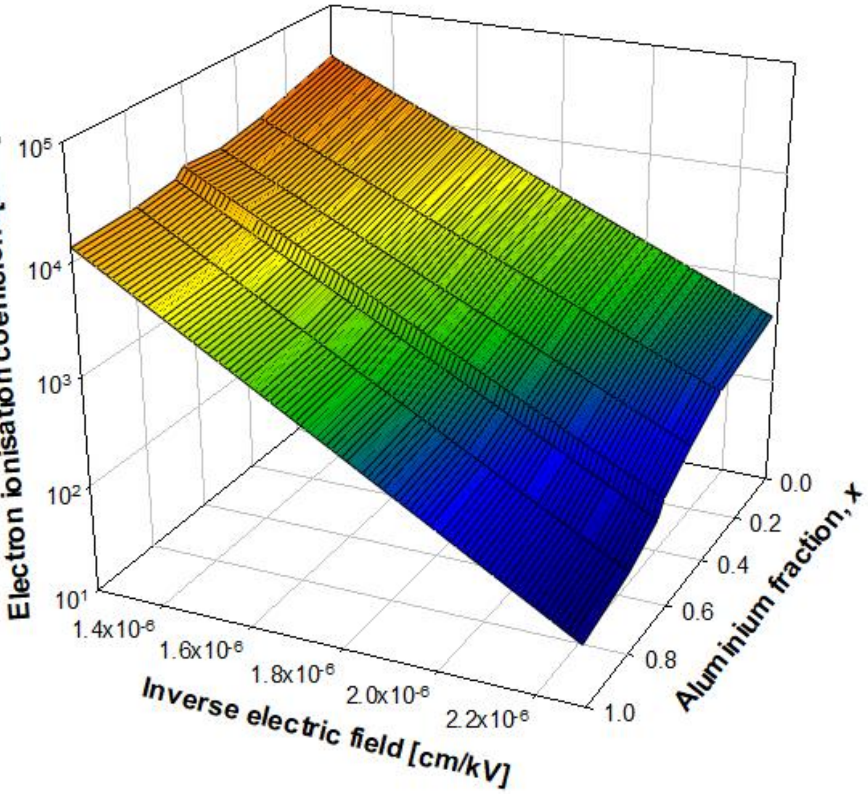

Fig. 4.8: Electron ionisation coefficients for $(Al_XGa_{1-X})_{0.52}In_{0.48}P$ shown as a function of aluminium fraction and electric field.

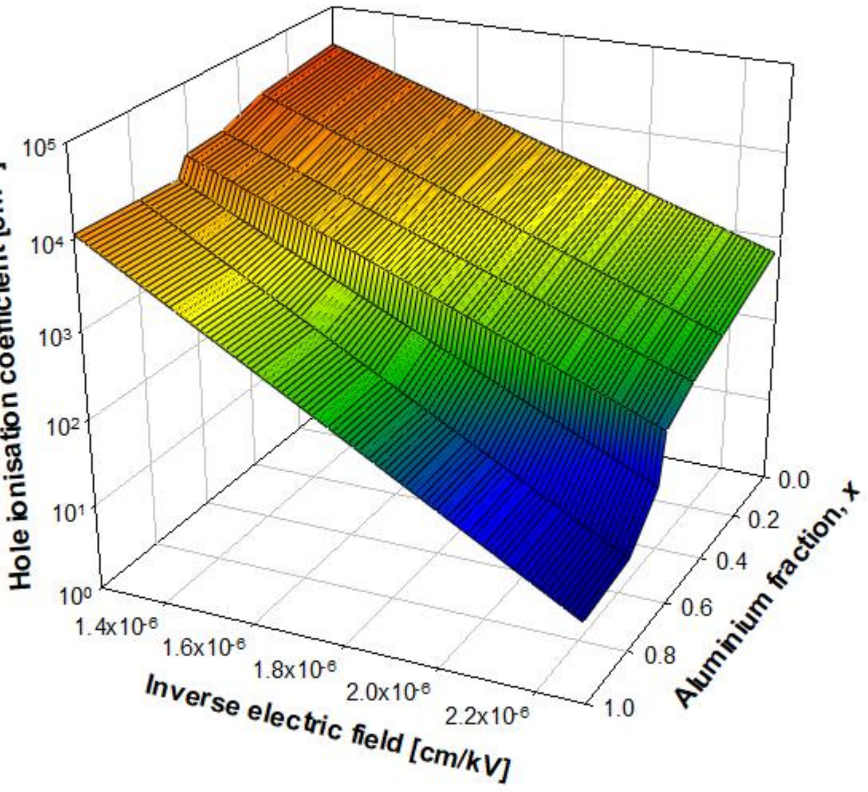

Fig. 4.9: Hole ionisation coefficients for $(Al_XGa_{1-X})_{0.52}In_{0.48}P$ shown as a function of aluminium fraction and electric field.

4.9 Discussion

Both α and β decrease with increasing aluminium fraction. $\beta > \alpha$ in GaInP, but the rates of decrease mean that β is approximately equal to α for $x = 0.31$-0.61 and $\beta < \alpha$ for $x > 0.61$. α decreases almost linearly with increasing x across the full composition range, with a slightly larger decrease between $x = 0.61$ and $x = 0.64$. β however decreases linearly with x up to $x = 0.61$, but then decreases rapidly until $x = 0.78$, after which it changes very little.

$Al_xGa_{1-x}As$ (AlGaAs), another wide band-gap alloy system which can be grown lattice-matched to GaAs, exhibits similar behaviour. Excess noise in AlGaAs is significantly reduced for $x > 0.61$ [25] which is similar to the threshold for low excess noise in AlGaInP. The impact ionisation coefficients of AlGaAs have been studied across the full composition range and reported by Plimmer *et al.* and Ng. *et al.* [147], [148], and a similar sharp decrease in β is observed between $x = 0.61$ and $x = 0.63$. This implies that the reduced excess noise in the higher aluminium concentrations in both alloy systems is due to the suppression of hole impact ionisation, which occurs after a threshold of aluminium content is reached. This threshold appears to be the same, or similar, in both AlGaInP and AlGaAs. In empirical terms, the reduction in β leads to a reduced β/α ratio, which produces reduced excess noise in keeping with classical McIntyre theory.

The ionisation coefficients have been used to calculate the avalanche breakdown voltages (V_{bd}) of ideal 1µm PIN structures for different compositions of AlGaInP. It is notable that the breakdown voltages for AlGaInP are the highest for any non-nitride III-V alloy. These are shown in figure 4.11 alongside equivalent data for AlGaAs. V_{bd} initially increases with x in both cases but saturates when $x \geq 0.64$ and when $x \geq 0.63$ in AlGaInP and AlGaAs respectively. After this point it increases very little in AlGaAs and appears not to increase at all in AlGaInP.

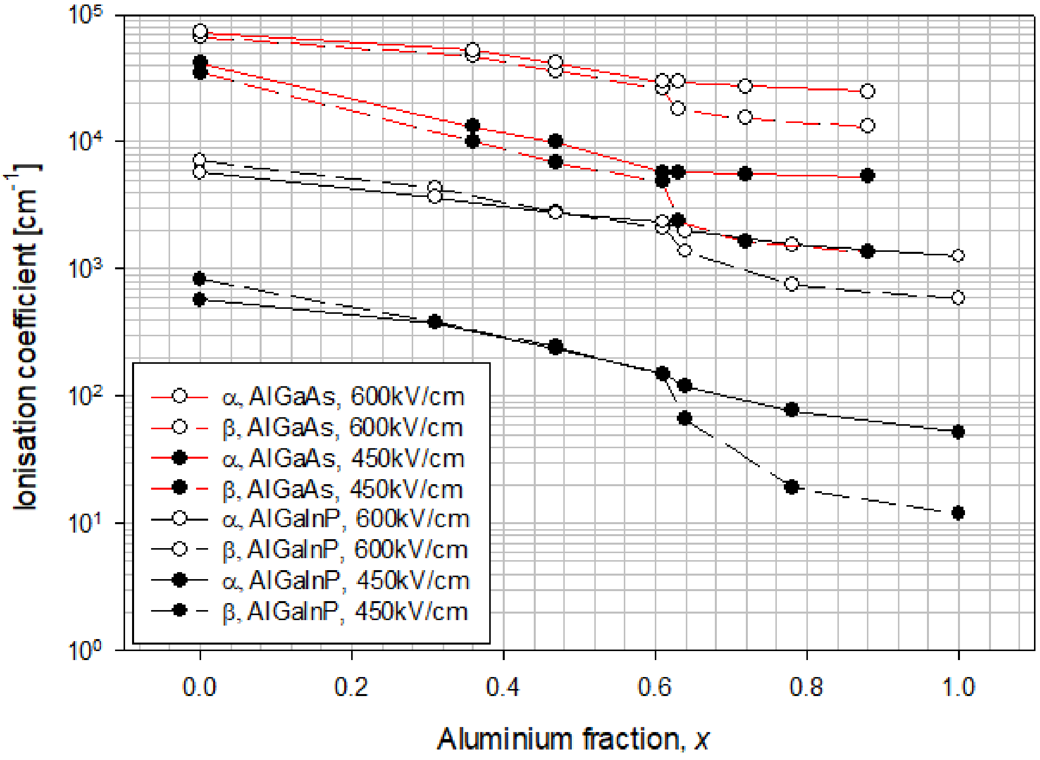

Fig. 4.10 Electron and hole ionisation coefficients for $(Al_xGa_{1-x})_{0.52}In_{0.48}P$ and $Al_xGa_{1-x}As$, shown as a function of aluminium fraction at electric fields of 450 and 600kV/cm.

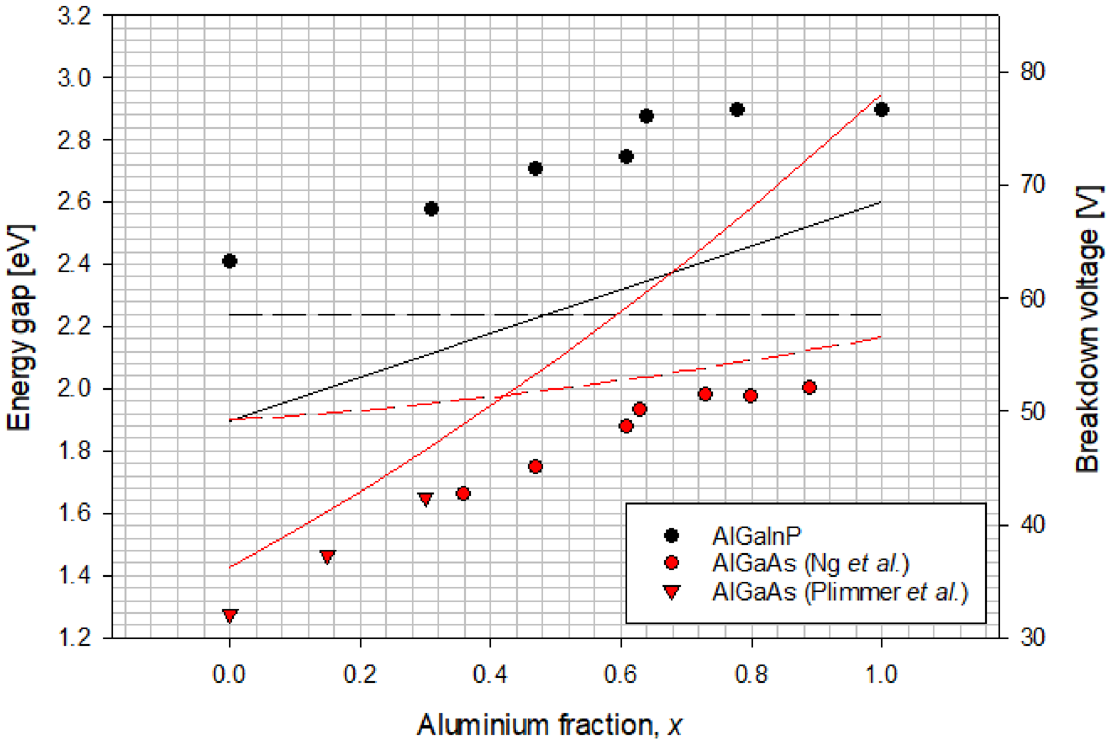

Fig. 4.11 Breakdown voltages for an ideal 1μm PIN structure with different compositions of $(Al_xGa_{1-x})_{0.52}In_{0.48}P$ and $Al_xGa_{1-x}As$ (right hand axis). Also shown are the *Γ* (solid line) and *X* (dashed line) energy gaps for these material systems (left hand axis, $Al_xGa_{1-x}As$ in red, $(Al_xGa_{1-x})_{0.52}In_{0.48}P$ in black).

At lower aluminium concentrations, the modelled breakdown voltages for both alloy systems are proportional to the Brillouin-zone-averaged indirect energy gap, E_{ind}, as predicted by Allam *et al.* [115] This is defined as:

$$\langle E_{\mathrm{ind}} \rangle = \frac{1}{8}[E_{\Gamma} + 3E_{\mathrm{X}} + 4E_{\mathrm{L}}] \quad (4.8)$$

Allam *et al.* showed that this is related to the breakdown voltage of a 1µm PIN structure in a range of semiconductor materials by equation 4.9:

$$V_{\mathrm{bd}} = 45.8(\langle E_{\mathrm{ind}} \rangle - 1.01) \quad (4.9)$$

At higher aluminium concentrations, the predicted breakdown voltages of AlGaInP and AlGaAs deviate from this relationship.
Silicon, which has a very large Γ energy gap, also deviates from the predicted breakdown voltage. Allam presents an alternative expression for E_{ind}, which excludes E_{Γ} because carriers from the lower energy satellite valleys are unlikely to gain sufficient energy to scatter into the Γ valley.

A wide Γ energy gap may also be responsible for behaviours seen in high-aluminium AlGaInP and AlGaAs. For both alloy systems, the β/α ratio is significantly reduced above a certain threshold of aluminium content, and V_{bd} saturates at a similar threshold. This threshold is the same in both alloy systems and occurs when x is roughly equal to 0.63. In both alloy systems the X conduction band minimum is lower than the Γ conduction band minimum for low values of x, and becomes higher for high values of x. The crossover point after which $E_{\Gamma} > E_X$ occurs at $x = 0.48$ and $x = 0.45$ in AlGaInP and AlGaAs respectively [116], [146]. This is significantly lower than the point at which these behaviours occur and the Γ/X crossover is unlikely to be directly responsible for them. However, the difference between E_{Γ} and E_X continues to increase in both alloy systems as x increases. The saturation of the breakdown voltage indicates that there may be a point at which the Γ energy gap becomes sufficiently large that the Γ valley is no longer involved in the impact ionisation process. This is supported by the fact that V_{bd} increases proportionally to the change in the X conduction band minimum after saturation – that is, it does not increase at all in AlGaInP, and it increases minimally in AlGaAs. The changes in the energy gaps and breakdown voltages with x are illustrated in figure 4.11.

The E_{Γ} - E_X separation when this happens is significantly larger in AlGaAs (approximately 0.28eV) than in AlGaInP (approximately 0.12eV), which may be related to the larger electron effective masses in AlGaInP. The reason for the sudden decrease in β seen in high-aluminium composition AlGaInP and AlGaAs is unclear without more detailed modelling of the valence band structure. It is possible that, when E_{Γ} is much larger than E_X, fewer hole impact ionisation events can satisfy the conditions of conservation of energy and momentum. This may occur as electrons can initiate impact ionisation events from a wide variety of positions in momentum-space in higher conduction bands, whereas holes generally initiate impact ionisation events in GaAs from the spin-orbit split off band [37]. This would mean that hole-initiated ionisation events require phonon interactions in order to conserve momentum when scattering electrons into the X-valley, while electrons are less affected by the increasingly indirect band-gap. Hole impact ionisation is also likely to be suppressed due to the flattening of the heavy hole band as aluminium content increases [116], which may cause the inter-band scattering rate to increase and prevent holes from accumulating sufficient energy to impact ionise [149].

Returning to a technological perspective, what these findings indicate is that the aluminium content in AlGaInP can be reduced significantly without detriment to the core useful properties of high breakdown voltage, low excess noise and low dark current. Existing research on AlInP [128] suggests that reducing the thickness of the high-field region can result in low excess noise. This would have the added advantage of increased operating speed due to reduced carrier transit time, and would not suffer from tunnelling current. This means that AlGaInP SACM structures with thin multiplication regions would be a useful material for a GaAs-based visible light APD with a tuneable and specific detection wavelength. SACM structures incorporating a thin AlGaInP multiplication region and a narrower band-gap alloy as an absorber could be used to produce a GaAs-based infrared APD, and in this case reducing the aluminium content to approximately $x = 0.75$ would be likely to yield an optimal compromise between maximising α/β ratio and maintaining material quality.

Knowledge of how α and β change with composition in this alloy system is also useful in the examination of other Al/Ga containing III-V alloys. This includes $Al_xGa_{1-x}As_{0.56}Sb_{0.44}$, which is of significant interest for its extremely low β/α ratio and is discussed in detail in chapters 5 and 6.

Chapter 5: Excess noise in $Al_{0.85}Ga_{0.15}As_{0.56}Sb_{0.44}$

5.1 Introduction

The objective of this chapter is to provide a comprehensive analysis of the bulk excess noise characteristics of $Al_{0.85}Ga_{0.15}As_{0.56}Sb_{0.44}$ ($Al_{0.85}Ga_{0.15}AsSb$), for a wide range of structure thicknesses and for material grown as random and digital alloys. 4 PIN structures, with thicknesses between 397nm and 996nm, and 1 NIP structure, with a thickness of 890nm, have been measured. A broad range of wavelengths has been used to measure avalanche multiplication and noise under pure electron injection and pure hole injection conditions, and variously mixed injection conditions. Noise in both digital and random alloy structures is also compared. Impact ionisation coefficients have also been extracted from multiplication data for these structures and those reported in the literature using a local model. Experimental data is combined with modelling of the transit time limited and RC limited bandwidths for these structures to provide a discussion of the relative merits of different structure thicknesses for this alloy.

5.2 Motivations

The $Al_xGa_{1-x}As_{0.56}Sb_{0.44}$ alloy system (hereafter referred to as AlGaAsSb) is a promising candidate for use as the multiplication region in SACM structures for optical communications APDs. It exhibits low bulk dark currents due to its wide band-gap and can be grown lattice-matched to InP. This is advantageous due to the high technological maturity and low substrate costs of InP, and means that AlGaAsSb can be combined with narrow band-gap alloys such as InGaAs or GaAsSb for absorption at the infrared wavelengths necessary for low-loss optical communications.

Most critically, AlGaAsSb exhibits very low excess noise. The excess noise and impact ionisation coefficients of AlAsSb, one of the ternary endpoints of the AlGaAsSb system, have been reported comprehensively [35], [36]. AlAsSb has an extremely high α/β ratio, >100 at electric fields below 460kV/cm, and >1000 at electric fields below 360kV/cm. This is significantly higher than any other wide band-gap III-V semiconductor material. An excess noise factor corresponding to an effective k of 0.005 has been reported for an AlAsSb structure with a 1550nm thick multiplication region. This is significantly lower than any other III-V alloy lattice-matched to InP, and even lower than silicon.

However, the high aluminium content of AlAsSb results in poor device reliability similar to that seen in other high-aluminium alloys, as well as high surface dark currents. This has prompted research into lower-aluminium alloys in the system, of which $Al_{0.85}Ga_{0.15}AsSb$ has received the most attention. Lee *et al.* have reported avalanche multiplication and excess noise data, with an effective k of 0.01, for a 1µm $Al_{0.85}Ga_{0.15}AsSb$ structure [150]. Excess noise for a 600nm $Al_{0.85}Ga_{0.15}AsSb$ PIN structure has also been reported by Taylor-Mew *et al.*, indicating excess noise well below that expected for an effective *k* of 0 [151]. Pinel *et al.* have also reported results on thinner PIN and NIP structures, showing significantly higher noise equivalent to a *k* approaching 0.01 [152]. These results do not provide a clear picture and it is therefore necessary to examine the bulk noise characteristics of this alloy more comprehensively.

5.3 Review of research into the $Al_xGa_{1-x}As_{0.56}Sb_{0.44}$ alloy system

Initial research into AlGaAsSb investigated thin structures, in keeping with the paradigm that thin structures were necessary for high-speed operation and that minimal excess noise in III-V alloys could be achieved only by taking advantage of the effects of the carrier dead space.

Measurements on thin $AlAs_{0.56}Sb_{0.44}$ (AlAsSb) were first performed by Xie and Tan, with the intention of investigating materials which may have sufficiently low tunnelling current for very thin multiplication regions. PIN structures were measured with avalanche region widths of 80 and 230nm [153]. Changes in dark current with temperature were used to infer that tunnelling current is negligible up to an electric field of 1.07MV/cm. Excess noise measurements on the same devices [154] indicated that α is significantly greater than β, and found effective *k* values of 0.1 and 0.05 for the 80 and 230nm structures respectively under pure electron injection conditions. The excess noise was attributed to dead space effects due to the thin avalanche regions of the structures. Uncertainty of the unmultiplied photocurrent and the effects of dead space meant that the impact ionisation coefficients could not be calculated from these samples. Due to significant surface oxidation in these structures, these initial studies were followed by investigations into $Al_xGa_{1-x}AsSb$ with $x = 0.85$ to 1 [155]. It was reported that the breakdown voltage decreases with increasing Ga concentration, and it was inferred that the band-gap decreases from 1.65 to 1.59eV as *x* increases from 0 to 0.15. It was also observed that surface leakage current decreases with increasing Ga concentration. They also reported low excess noise, with an effective *k* of approximately 0.1, in devices with $x = 0.1$ and 0.15 and avalanche region widths of 110-116nm [156]. Excess noise was slightly higher in the structure with lower aluminium content.

Zhou *et al.* then reported an InGaAs/$Al_{0.85}Ga_{0.15}AsSb$ SAM APD with a 100nm avalanche layer [157], which displayed negligible tunnelling current and a gain-bandwidth product of 407.4 GHz. Xie *et al* have reported an InGaAs/$Al_{0.85}Ga_{0.15}AsSb$ SAM APD with an even higher gain-bandwidth product of 424 GHz [43], which remains the highest reported for an InP-based SAM-APD.

Measurements on thicker PIN and NIP AlAsSb structures, with nominal avalanche region thicknesses of 100-1550nm, were later performed by Yi *et al* [35]. This allowed the ionisation coefficients to be calculated for the first time and demonstrated the extremely wide α/β ratio of this alloy. The use of thicker structures also meant that it was possible to discount dead space effects, which were considered to be the source of the low excess noise in the devices of Xie *et al.* This research was critical in showing that low noise and high speed could be achieved in a thick detector structure, which have the additional advantage of increased sensitivity. The α/β ratio also increases rapidly as electric field decreases, which explained the result of Xie *et al.* [154] whereby the excess noise decreased significantly when the avalanche region thickness was increased from 80 to 230nm. Yi *et al.* also reported very low excess noise in thick AlAsSb structures, equivalent to a k value of 0.005 for a 1550nm thick multiplication region [36]. This is significantly lower than the excess noise in silicon for a structure of equivalent thickness. They showed that the excess noise factor in thicker structures was in accordance with that predicted by McIntyre's local model for the ionisation coefficients, but that the noise was lower than that predicted by the local model in submicron structures. This indicates the presence of significant dead space effects in the thinner structures.

These developments in AlAsSb have prompted further investigations into the bulk properties of the $Al_xGa_{1-x}AsSb$ alloy system. Excess noise measurements of thicker $Al_{0.85}Ga_{0.15}AsSb$ structures have been reported and are detailed in section 5.2. The optical properties of $Al_{0.85}Ga_{0.15}AsSb$ have also been reported, indicating absorption up to a wavelength of 850nm [158].

5.4 Wafer and device details

One digital alloy (DA) and three random alloy (RA) $Al_{0.85}Ga_{0.15}AsSb$ PIN structures, and a digital alloy NIP structure, were grown on semi-insulating InP substrates using molecular beam epitaxy. The DA PIN structure is the same wafer as that described in [150] and the 1µm RA structure is described in [159]. The parameters of each structure are given in table 5.1. Digital alloy growth here refers to constructing a pseudo-quaternary alloy by growing very thin alternating layers of four binary alloys, whereas random alloy growth refers to growing a bulk quaternary structure in which both the group III and group V atoms are distributed with uniform randomness throughout the crystal.

Digital alloy processes have historically been the choice for the growth of thick quaternary alloy structures on InP substrates because RA growth suffers from phase separation due to the large theoretical miscibility gap in $Al_xGa_{1-x}As_ySb_{1-y}$, which results in material defects [160], [161]. DA structures may also exhibit lower excess noise than RA structures in some cases, as observed in InAlAs [23]. However, RA growth is preferable if possible as it can be adapted to metal-organic chemical vapour deposition (MOCVD), which makes it more suitable for commercialization. DA growth of Sb/As alloys can also be problematic due to imperfect interfaces between the alternating binary alloy layers. These occur because the As atom bonds more strongly to the group III atoms than the Sb atom, and residual As may diffuse from the As-containing layers to the Sb-containing layers [162]–[164]. This results in high defect concentrations around the interfaces, which significantly detriments device performance. The large number of mechanical shuttering operations required for digital alloy growth of Sb-containing alloys can also lead to build-up of residual Sb on the shutter of the MBE reactor, which can lead to significant MBE downtime [159].

Recent studies, including a report on the 1µm RA structure used in this work, have indicated that high-quality RA growth of antimonide quaternary alloy systems on InP is possible by employing growth temperatures of 450ºC or lower [34], [159], [165]. Low growth temperatures prevent phase separation by reducing surface adatom mobility [159], which slows the rate of phase separation. This means that crystal growth can occur before equilibrium conditions are reached.

PIN851, PIN852, and NIP851 were grown with a highly doped 400nm InGaAs bottom contact layer and a 20nm InGaAs top cladding layer. PIN853 and PIN854 were grown with a highly doped 500nm InAlAs bottom contact layer and a 20nm InGaAs top cladding layer. The nominal widths of the $Al_{0.85}Ga_{0.15}$AsSb cladding layers for all structures were 300nm for the top cladding and 100nm for the bottom cladding. The actual UID region widths and dopings were calculated using capacitance-voltage measurements, and are detailed in table 5.1.

TABLE 5.1
PARAMETERS OF $AL_{0.85}GA_{0.15}AS_{0.56}SB_{0.44}$ WAFERS USED IN THIS STUDY

Wafer	Growth type	Nominal intrinsic region width [µm]	Calculated intrinsic region width, w [µm]	N_i [$\times 10^{15}$cm^{-3}] ± 1×10^{15}cm^{-3}	N_p [$\times10^{17}$cm^{-3}] ± 1×10^{17}cm^{-3}
PIN851	DA	1	0.870	16	30
NIP851	DA	1	0.890	18	30
PIN852	RA	1	0.996	1.8	11
PIN853	RA	0.6	0.580	2.5	40
PIN854	RA	0.4	0.397	5	40

Wafers PIN851, NIP851, and PIN852 were fabricated at Sheffield. Mesa structures with diameters of 420, 220, 120, and 70µm were fabricated using wet etching in a solution composed of 20g citric acid:5ml H_3PO_4:5ml H_2O_2:120ml H_2O. Wafers PIN853 and PIN854 were fabricated at the Ohio State University. These wafers were fabricated with diameters of 350, 250, 200, 150, 100, and 60µm by wet etching using the same etchant composition used at Sheffield. Ti/Au with a thickness of 20/200nm was used for top and bottom contacts for all devices.

5.5 Dark I-V and C-V measurements

5.5.1 Dark I-V measurements

Figure 5.1 shows reverse dark current densities for each sample. The dark currents did not scale with device area, indicating the presence of surface dark currents. There was some variation in dark current between devices, which is attributed to the sensitivity of surface dark currents to imperfections in the mesa surface. Figure 5.2 shows forward bias dark current densities for each sample. Series resistance in all devices was of a sufficiently low order of magnitude to avoid distorting excess noise measurements by reducing the effective bandwidth of the measurement system, which would lead to error of the type discussed in section 3.8.2.

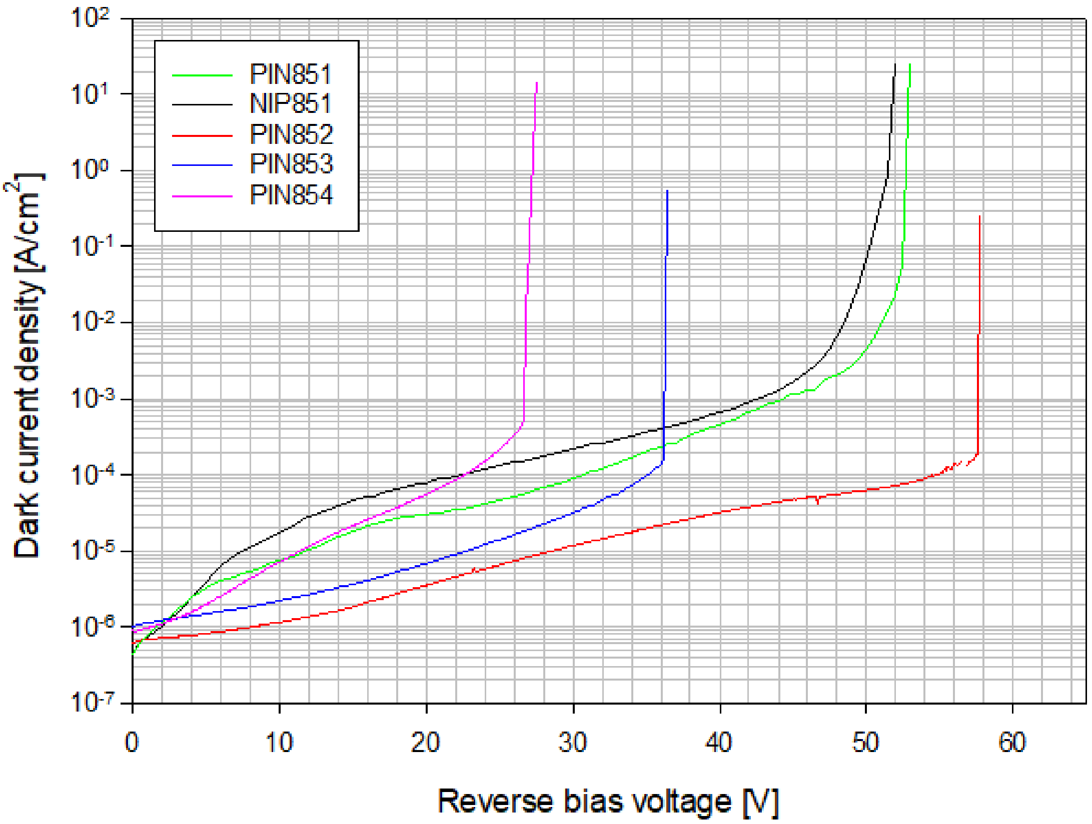

Figure 5.1: Reverse dark current densities for each of the $Al_{0.85}Ga_{0.15}AsSb$ wafers used in this study. Data for PIN851, PIN852, and NIP851 are for 220µm diameter devices, and data for PIN853 and PIN854 are for 200µm diameter devices.

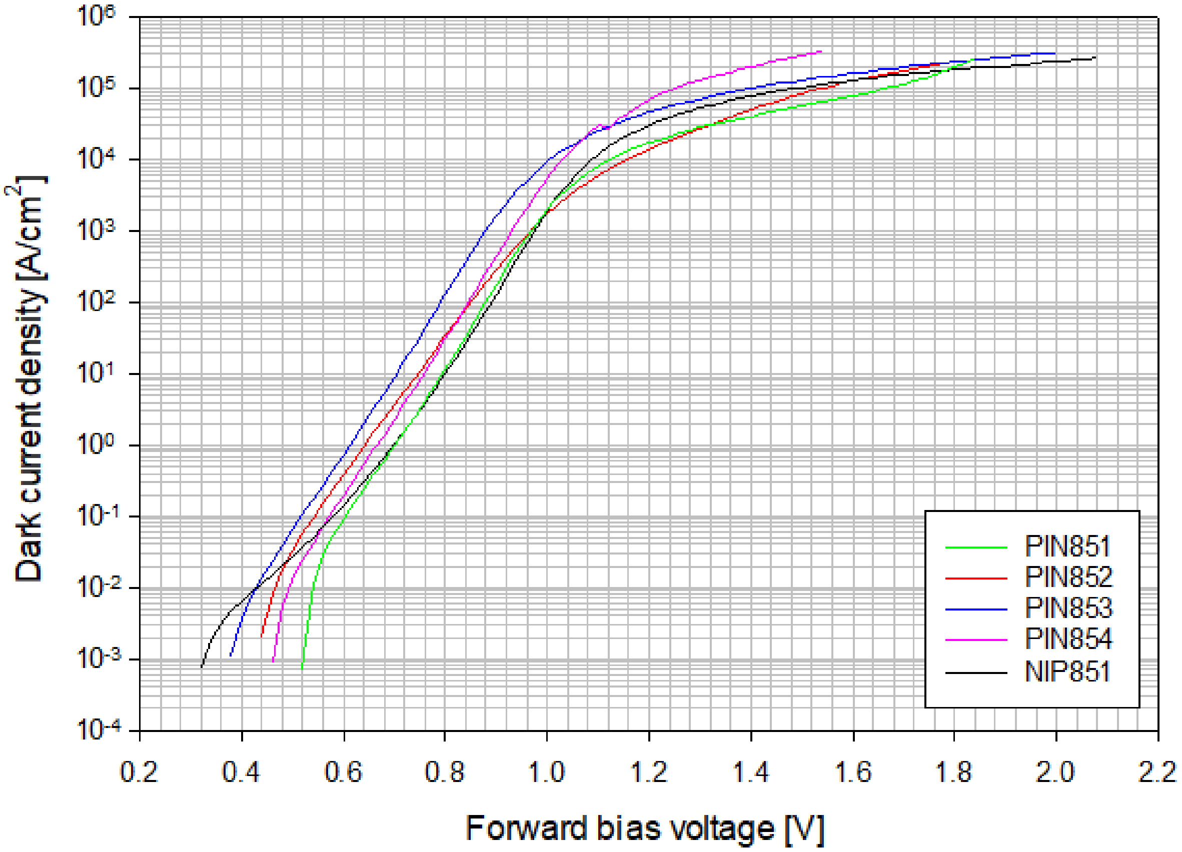

Figure 5.2: Forward dark current densities for each of the $Al_{0.85}Ga_{0.15}AsSb$ wafers used in this study. Data for PIN851, PIN852, and NIP851 are for 220µm diameter devices, and data for PIN853 and PIN854 are for 200µm diameter devices.

5.5.1 C-V measurements

Reverse bias capacitance-voltage measurements for each wafer are shown in figure 5.3. A static dielectric constant of 11.48 was linearly interpolated from the dielectric constants of AlAsSb (10.95, [35]) and GaAsSb (14.47, [116]). The region widths and dopings used to generate the simulated data for each sample are given in table 5.1.

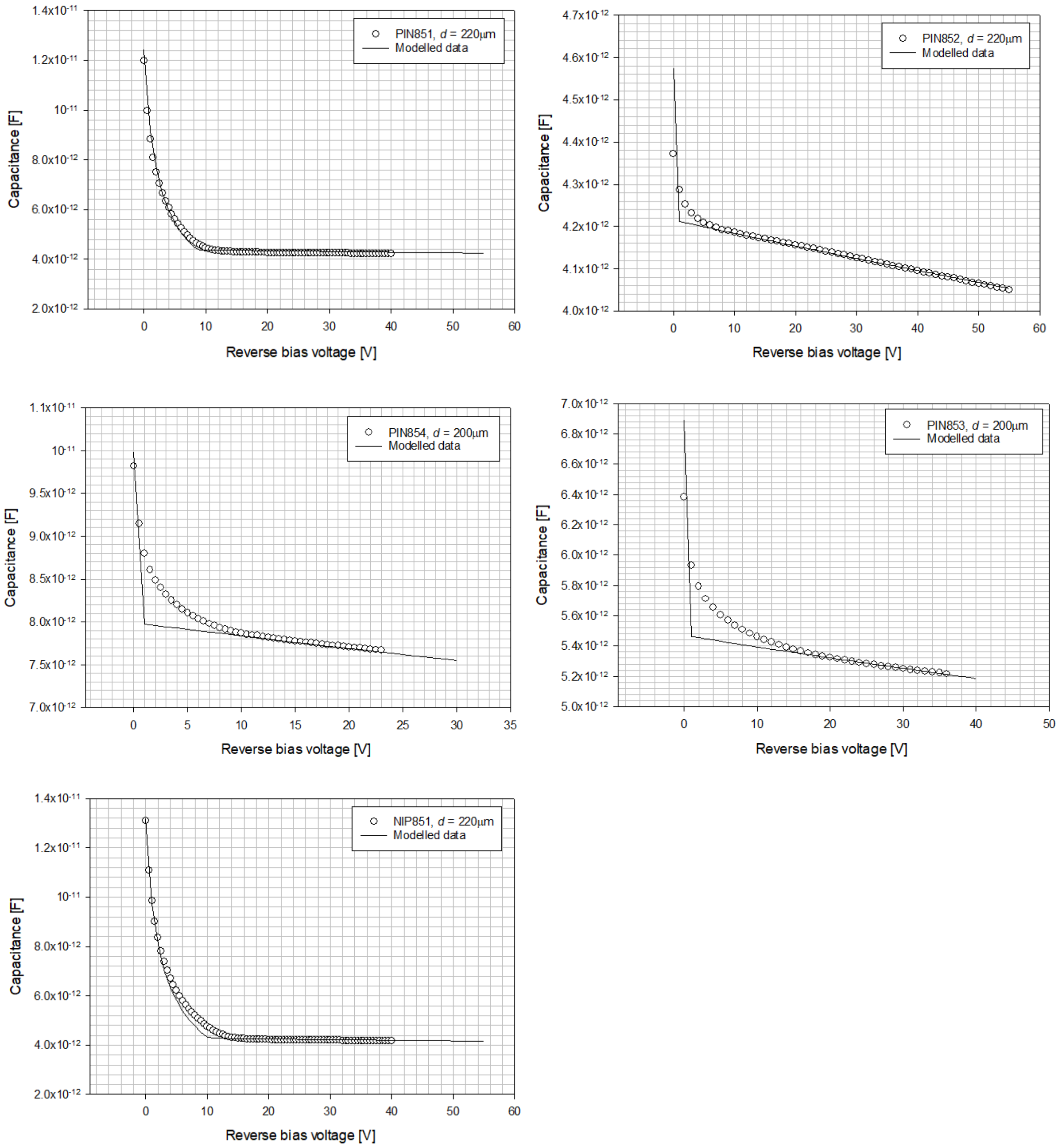

Figure 5.3: Capacitance-voltage data for each of the $Al_{0.85}Ga_{0.15}AsSb$ wafers used in this study, shown with the simulated data used to infer the region widths and doping densities.

5.6 Multiplication measurements

Figures 5.4 and 5.5 show multiplication data for different structures under varying injection conditions. Data are shown in the form M-1 so that the onset of multiplication can be seen. A 455nm fibre-coupled LED was used to elicit pure injection conditions, and 530, 625, and 780nm LEDs were used to produce variously mixed injection conditions. A study of the optical characteristics of this alloy has indicated that injection should be pure for wavelengths of 460nm or shorter with a top cladding thickness of 300nm [158].

Multiplication decreases with increasingly mixed injection conditions for all PIN structures and decreases with increasingly mixed injection conditions for the digital alloy NIP structure. Multiplication data for 780nm on the NIP structure were almost identical to that seen in the DA PIN structure and have been omitted from figure 5.4 for clarity. It is notable that the effect of mixed injection conditions in the PIN structures is small, although slightly greater in the random alloy PIN, whereas even a small amount of mixed injection in the NIP structure gives multiplication that is close to that seen in the PIN structures. This indicates the domination of electron-initiated ionisation events - a small number of primary electrons in the hole-dominated condition changes the multiplication result significantly, whereas a small number of primary holes in the electron-dominated condition has a minimal effect.

The change in multiplication with varying injection conditions is also less significant in the DA PIN structure than in the random alloy PIN structures. This is attributed to the higher background doping in the DA structure, which is considered to result from imperfect interfaces between the binary alloy layers. This in turn leads to high defect concentrations close to the interfaces. Higher background doping results in an electric field with a tapered shape, with a higher field strength closer to the *p-n* junction. If the electric field is uniform across the intrinsic region, carriers that drift into the high-field cladding region, or carriers that are generated anywhere in the high-field region will be equally likely to impact ionise. If the field is not uniform, carriers which drift into the high-field region from the cladding region further from the *p-n* junction (the *p*-type cladding region in the case of *p*-type background doping) will be less likely to impact ionise than those that are generated closer to the *p-n* junction. The probability of ionisation will increase as carriers drift towards the *p-n* junction, where the electric field is highest. This will reduce multiplication in purer injection cases and reduce the disparity between multiplication characteristics under pure and mixed injection conditions.

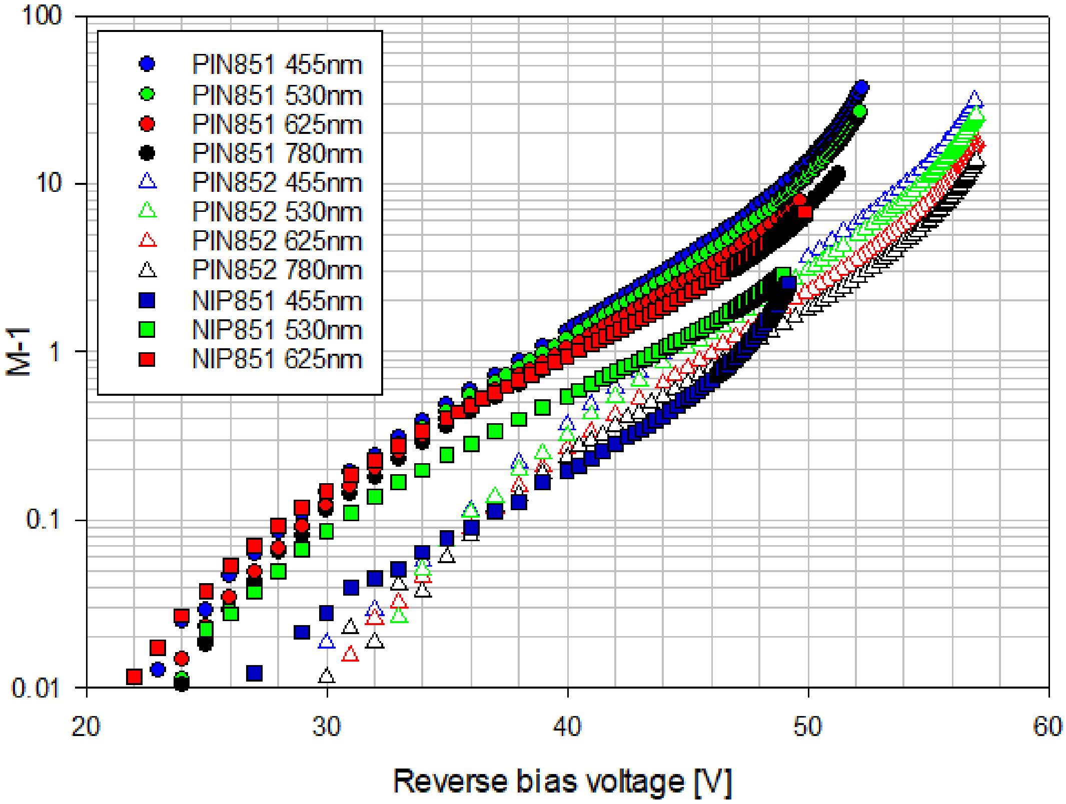

Figure 5.4: Multiplication data for PIN851, PIN852, and NIP851 under various injection conditions, shown in the form M-1.

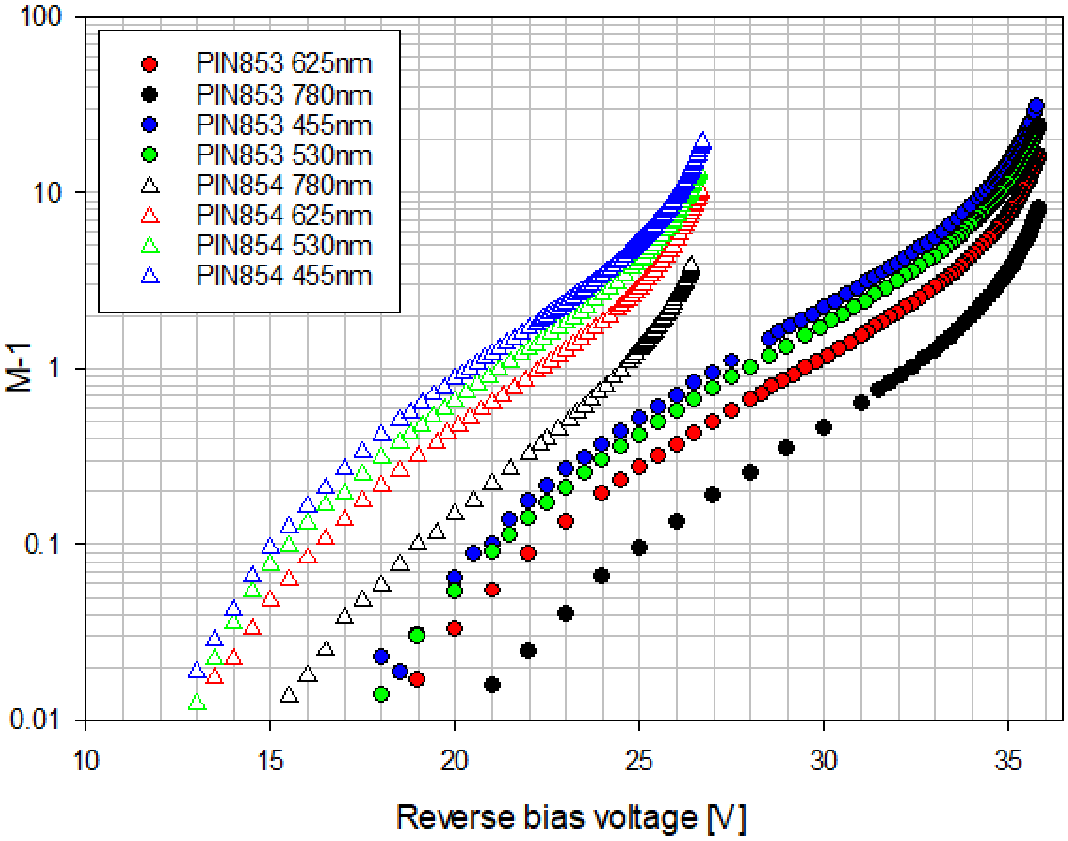

Figure 5.5: Multiplication data for PIN853 and PIN854 under various injection conditions, shown in the form M-1.

5.7 Excess noise measurements

Figure 5.6 shows the variation in excess noise for varying injection conditions in PIN851 and PIN852. Under pure electron injection conditions, the excess noise factor is similar in both structures and is equal to that predicted by McIntyre's local model for an effective k of 0 at M = 20, and equal to that predicted for an effective k of 0.01 at M = 30. When M < 20 the excess noise factor is below that predicted for an effective k of 0. The shape of the F vs. M curve does not correspond to that predicted by McIntyre's local model. This is expected in a wide band-gap alloy where the effects of dead space are significant. The deviation from theoretically predicted data is discussed further in section 5.10. The difference in the measured excess noise factor values between the random and digital alloy structures was small, but the noise in the RA structure appears to start slightly lower and increase with a steeper gradient, indicating that the noise may be higher at higher values of M. All PIN structures show an increase in excess noise with increasing wavelength. The noise for uniformly mixed injection was approximately equivalent to that predicted for an effective k of 0.06 in the 870nm DA structure and 0.14 in 996nm RA structure. As is the case for the multiplication, the DA structure shows a smaller change in mixed injection than the RA structures. This is attributed to the tapered shape of the electric field in the DA structure as described in section 5.6.

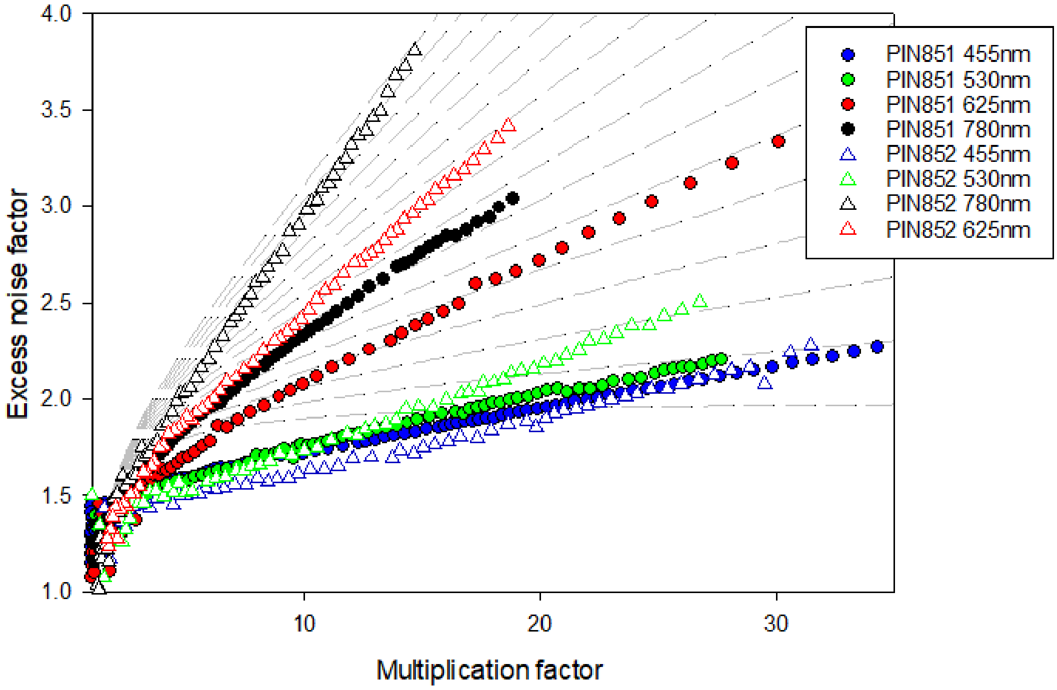

Figure 5.6: Excess noise factor data for PIN851 and PIN852 under varying injection conditions. Dashed lines represent the excess noise factor predicted by McIntyre's local model for k values of 0 to 0.1 in steps of 0.01.

Figures 5.7 and 5.8 show the noise for PIN851 and NIP851. Under illumination at 780nm both structures show identical noise characteristics, confirming that the carrier injection conditions are uniformly mixed at this wavelength. The noise in the NIP structure increases with decreasing wavelength, and under pure injection conditions the noise is equivalent to that predicted for an effective *k* of approximately 50. Notably, similarly to the trend observed in the multiplication data, the magnitude of the change in noise performance under weakly mixed injection conditions is much larger in the NIP structure than in the PIN structure. In the NIP structure, the excess noise reduces from an effective *k* of 50 under 455nm illumination to an effective *k* of 1 under 530nm illumination, whereas the noise characteristics in the PIN structure are almost identical for illumination with these two wavelengths.

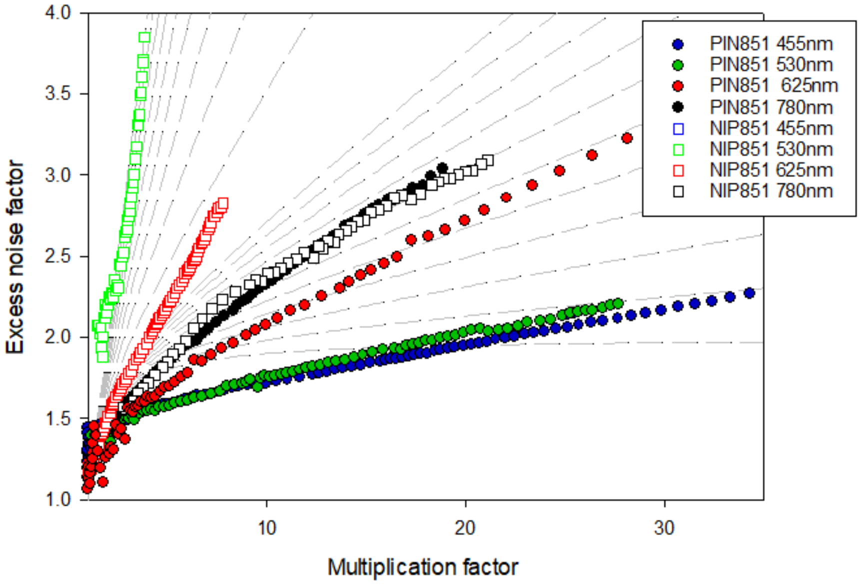

Figure 5.7: Excess noise factor data for PIN851 and NIP851 under varying injection conditions. Dashed lines represent the excess noise factor predicted by McIntyre's local model for *k* values of 0 to 0.1 in steps of 0.01, and 0.1 to 1 in steps of 0.1.

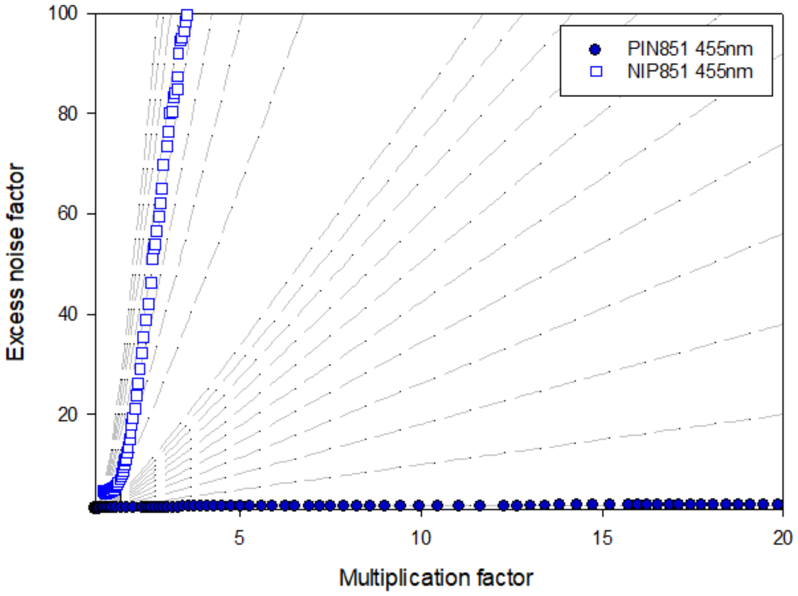

Figure 5.8: Excess noise factor data for PIN851 and NIP851 under pure injection conditions. Dashed lines represent the excess noise factor predicted by McIntyre's local model for *k* values of 0 to 10 in steps of 1, and 10 to 100 in steps of 10.

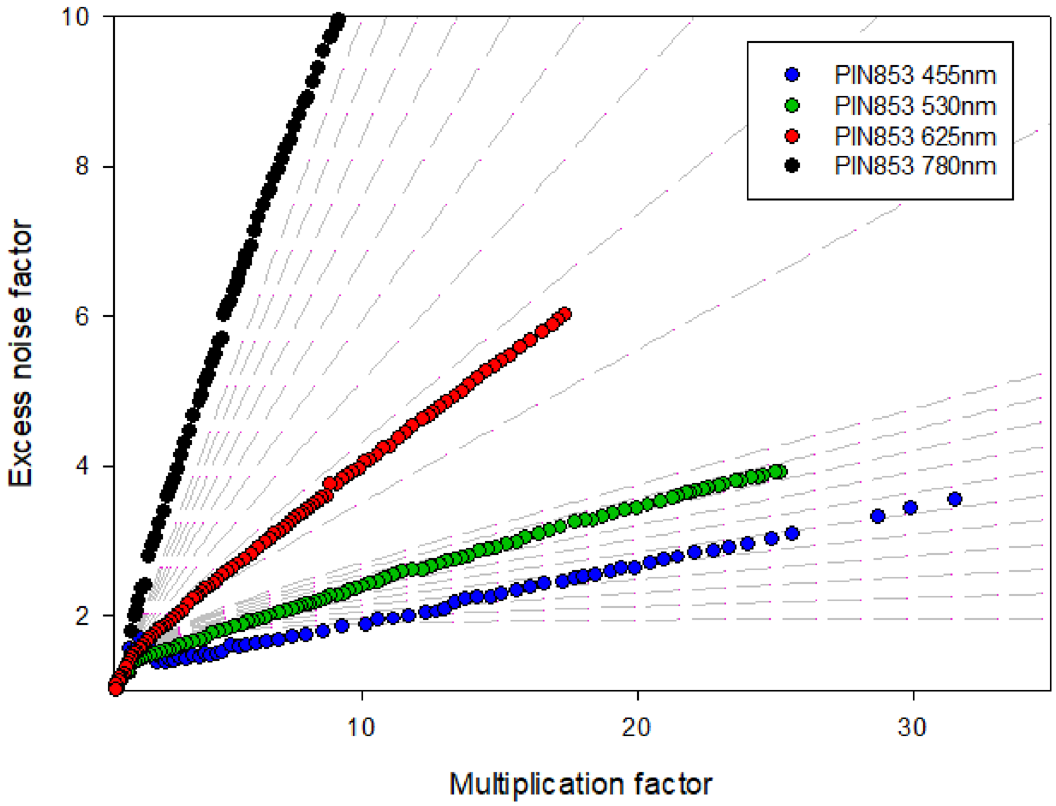

Figure 5.9: Excess noise factor data for PIN853 under varying injection conditions. Dashed lines represent the excess noise factor predicted by McIntyre's local model for *k* values of 0 to 0.1 in steps of 0.01.

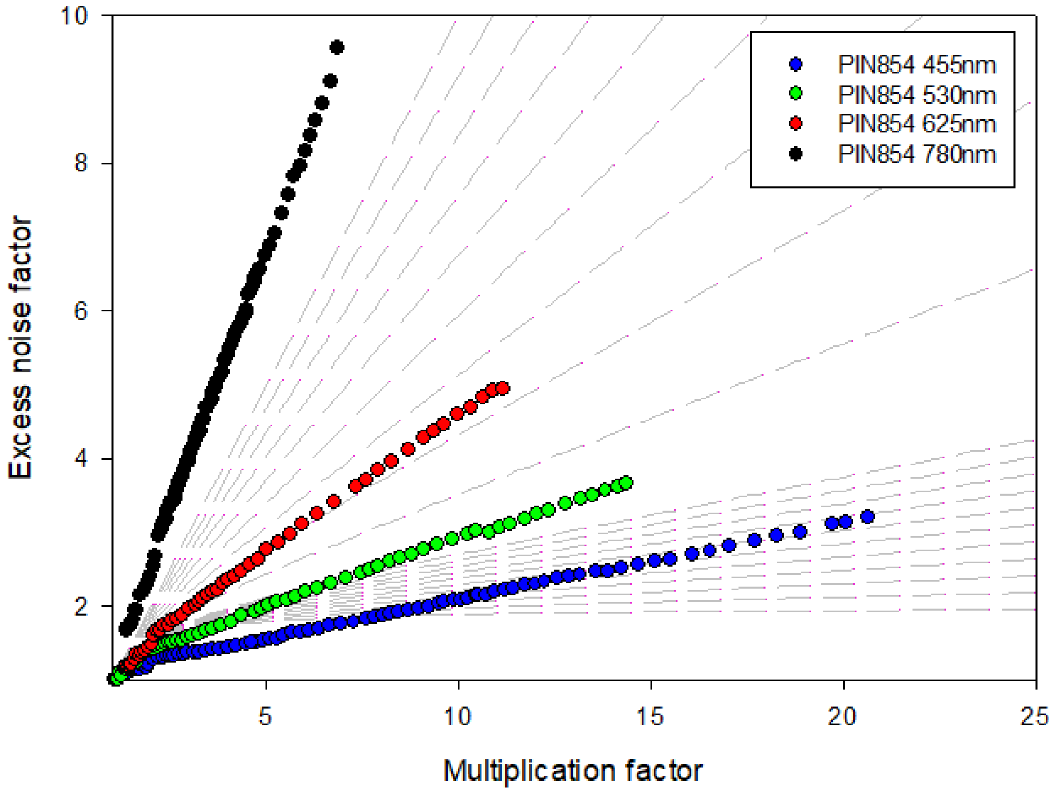

Figure 5.10: Excess noise factor data for PIN854 under varying injection conditions. Dashed lines represent the excess noise factor predicted by McIntyre's local model for *k* values of 0 to 0.1 in steps of 0.01.

Figures 5.9 and 5.10 show excess noise data for PIN853 and PIN854 respectively. The noise was seen to increase with decreasing structure thickness: the 400nm structure shows excess noise equivalent to a k of 0 at an M of approximately 7.5, and equivalent to a k of 0.065 at an M of 20. The 590nm structure shows noise equivalent to a k of 0 at an M of 10 and equivalent to a k of 0.04 at an M of 20. Both structures show a similar variation in excess noise factor for varying injection conditions. Notably, the noise under 780nm illumination was greater than that expected for a k of 1 in both structures. This is theoretically only possible in an alloy where $\alpha > \beta$ if holes make up the majority of the primary carriers. This result was therefore attributed to some photons passing through the intrinsic region and being absorbed in the back n^+ cladding layer or the n^+ InAlAs back contact layer, resulting in a higher proportion of holes as primary carriers.

5.8 Impact ionisation coefficients

The multiplication results for these structures were used to fit impact ionisation coefficients for this alloy. As data were available for structures of varying thicknesses, including thinner structures described in the literature [151], [152], the ionisation coefficients were fitted using multiplication and breakdown voltage data only. This means that a local model can be used, simplifying the fitting process, as the effects of dead space are less significant on multiplication than they are on excess noise. The impact ionisation coefficients for AlAsSb were used as a starting point, and the model was used to produce simulated multiplication data for each structure. The coefficients were varied using an iterative fitting process to produce simulated data matching the measured data for each structure. The model used calculated an electric field profile based on the region widths and dopings determined for each structure to account for depletion into the cladding regions, and for the tapered electric field profile in the structures with higher background doping in the intrinsic region.

The ionisation coefficients are given in equations 5.1 and 5.2 in the form of the standard Chynoweth expression,

$\alpha(\beta) = Aexp(-(\frac{B}{\xi})^C)$:

$$\alpha = \begin{cases} 5.5 \times 10^5 exp\left(-\left[\frac{1.21\times10^6}{\xi}\right]^{1.43}\right) cm^{-1}, for\ 200kV/cm < \xi \le 500kV/cm \\ 8 \times 10^5 exp\left(-\left[\frac{1.3\times10^6}{\xi}\right]^{1.43}\right) cm^{-1}, for\ 500kV/cm < \xi \le 1000kV/cm \end{cases} \quad (5.1)$$

$$\beta = \begin{cases} 2.5 \times 10^5 exp\left(-\left[\frac{1.7\times10^6}{\xi}\right]^{1.44}\right) cm^{-1}, for\ 200kV/cm < \xi \le 500kV/cm \\ 4.5 \times 10^5 exp\left(-\left[\frac{1.92\times10^6}{\xi}\right]^{1.38}\right) cm^{-1}, for\ 500kV/cm < \xi \le 1000kV/cm \end{cases} \quad (5.2)$$

Where ξ is electric field in V/cm.

Measured multiplication data for the structures used in this study, and multiplication data for the 600nm PIN structure described by Taylor-Mew *et al.* [151] and the thinner PIN and NIP structures described by Pinel *et al.* [152], are shown alongside corresponding simulated data using the fitted ionisation coefficients in figure 5.11. The multiplication data reported by Taylor-Mew *et al.* is for a structure of comparable thickness to PIN853, and is similar to our measured data for the latter.

The impact ionisation coefficients are shown as a function of electric field in figure 5.12. The ionisation coefficients for AlAsSb are included for comparison. The fitted α for $Al_{0.85}Ga_{0.15}AsSb$ is almost identical to that reported for AlAsSb. The fitted β is slightly higher than in AlAsSb.

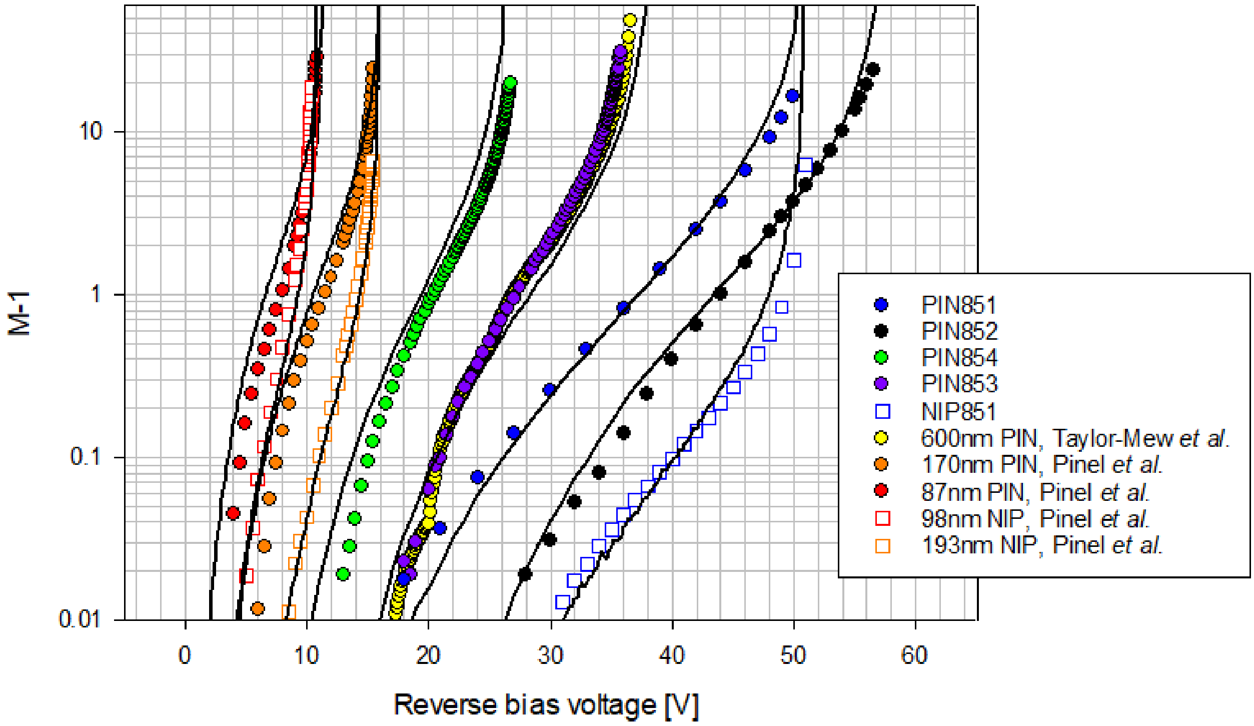

Figure 5.11: Multiplication data, in the form M-1, for each of the $Al_{0.85}Ga_{0.15}AsSb$ wafers used in this study and for structures reported on in the literature, shown with simulated data produced using the fitted ionisation coefficients.

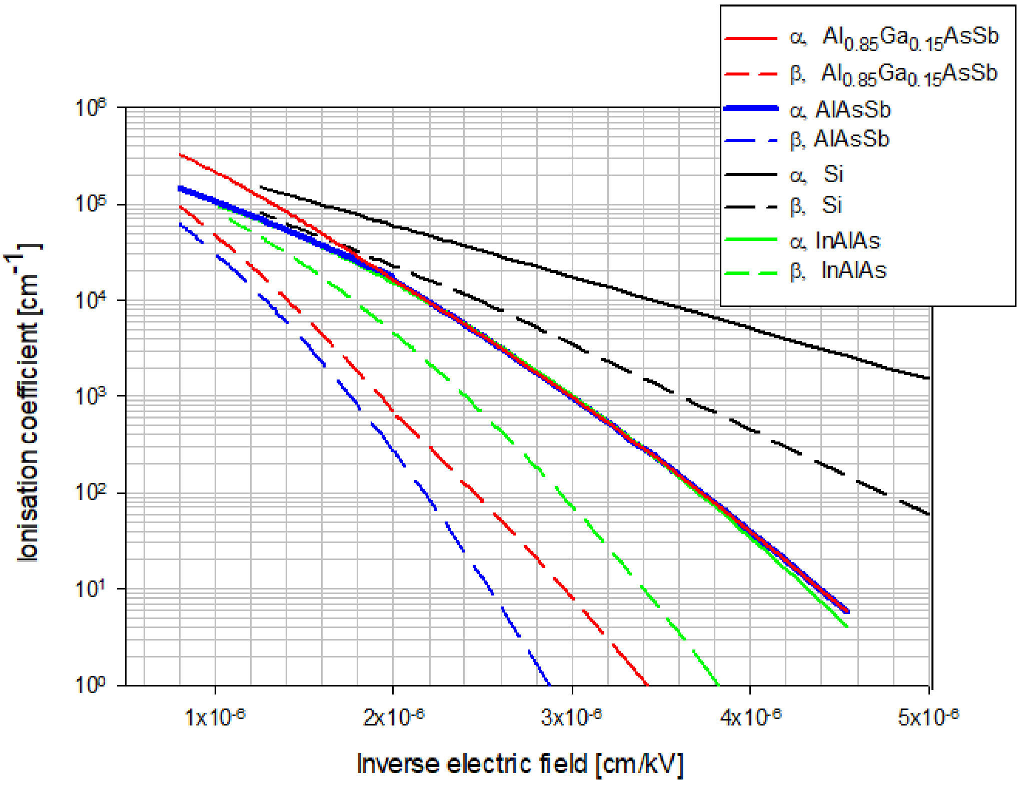

Figure 5.12: Electron and hole impact ionisation coefficients shown as a function of inverse electric field for $Al_{0.85}Ga_{0.15}AsSb$, AlAsSb [35], Si [166], and InAlAs [167].

5.9 Bandwidth modelling

The transit-time limited bandwidth of each of the random alloy PIN structures (PIN852, PIN853, and PIN854) has been simulated for a variety of multiplication values. This was done by using an RPL model, incorporating the previously fitted ionisation coefficients, to simulate the transient current response of each device for a given voltage. This was processed using a Fourier transform to give the frequency response, and the -3dB frequency for each voltage was determined graphically. The simulations assumed pure electron injection conditions and the actual region widths and dopings of the structures were used as parameters in the model to facilitate comparison with measured excess noise data. The impulse response for each trial in the RPL model computation is calculated using Ramo’s theorem [168], where the avalanche current for each carrier is given by equation 5.3:

$$i = qv/w \quad (5.3)$$

Where q is the electronic charge, v is the carrier drift saturation velocity, and w is the width of the avalanche region. The carrier drift saturation velocities were approximated as 1x10^{5}m/s and

6.65×10^4m/s for electrons and holes respectively, which are the values in AlAsSb [36]. The simulated -3dB frequencies are shown as a function of multiplication factor for each structure in figure 5.13.

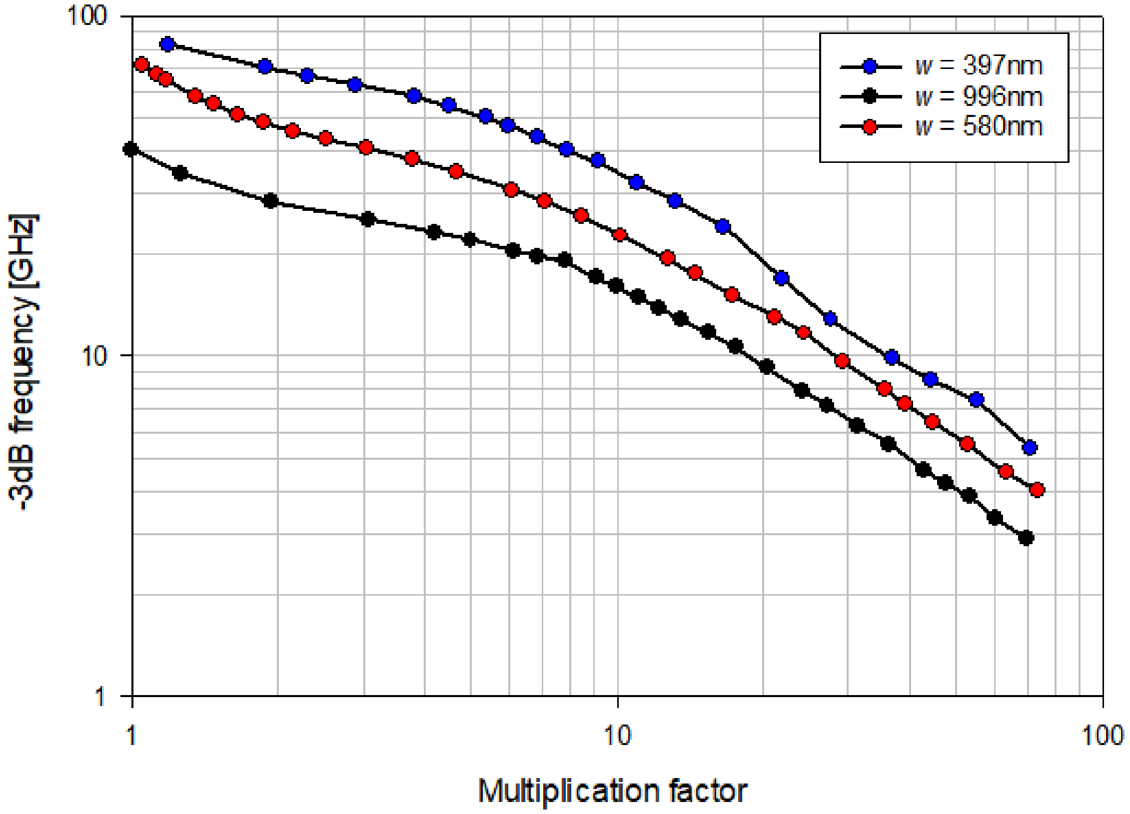

Figure 5.13: Theoretical -3dB frequency due to carrier transit time, shown as a function of multiplication factor for $Al_{0.85}Ga_{0.15}$AsSb PIN devices with intrinsic region thicknesses of 397, 580, and 996nm.

Bandwidth decreases with increasing structure thickness, as is expected due to longer carrier transit time. However, the difference in bandwidth between structures becomes smaller at higher multiplication factors, in relative as well as absolute terms.

The RC limited bandwidth has also been calculated for each PIN structure for a range of device areas. This is straightforward to calculate using equation 5.4:

$$f_{3dB} = \frac{1}{2\pi R \frac{\varepsilon_0 \varepsilon_r A}{d}} \quad (5.4)$$

Where R is the device series resistance, A is the device area, and d is the junction depletion width. For the purposes of this calculation, the depletion width was assumed to be equivalent to the width of the intrinsic region. A series resistance of 50Ω was used, as this is a common selection in commercial devices for purposes of impedance matching. The device areas used ranged from 7.85×10^{-11}m^2 to 1.26×10^{-7}m^2, equivalent to circular devices with diameters ranging from 10 to 400µm. The calculated RC limited bandwidths are shown in figure 5.14.

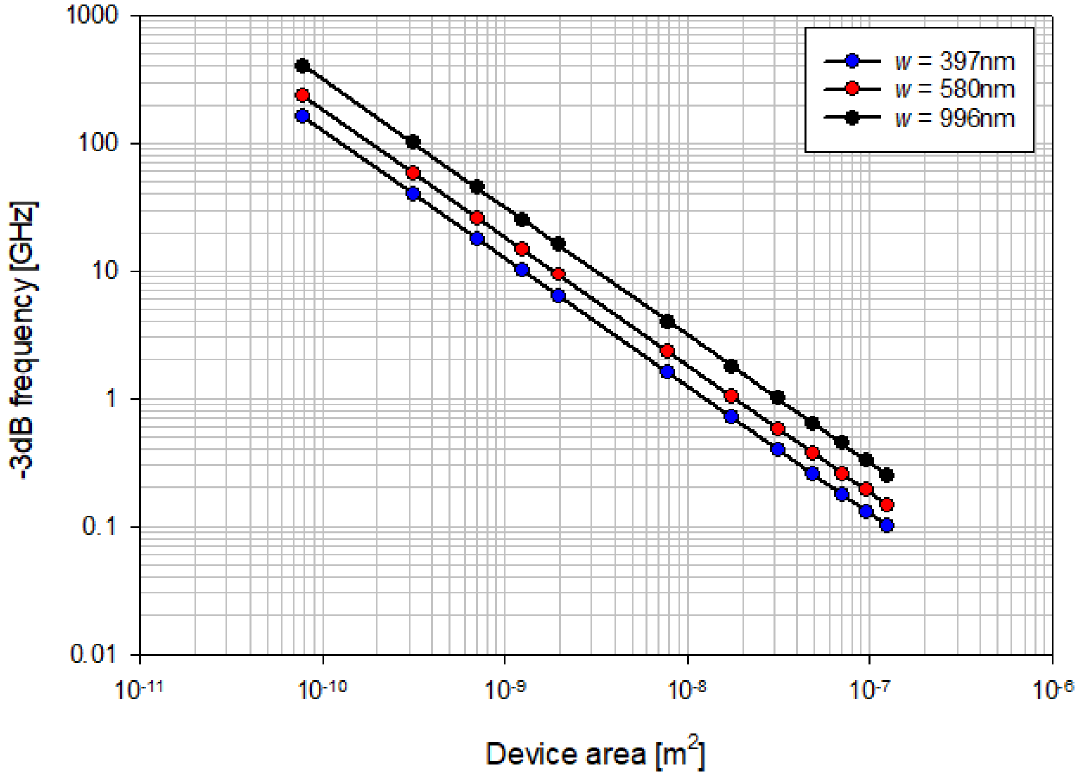

Figure 5.14: Theoretical -3dB frequency due to R-C time constant for a nominal series resistance of 50Ω, shown as a function of device area for $Al_{0.85}Ga_{0.15}AsSb$ PIN devices with intrinsic region thicknesses of 397, 580, and 996nm.

At low gains the RC limited bandwidth is lower than the transit-time limited bandwidth for all but the smallest devices, and devices greater than approximately 1x10^{-8}m^2 in area (equivalent to a circular device with a diameter of 113µm) are constrained by the RC limited bandwidth even at high gain values.

5.10 Discussion

These results show that a higher proportion of electrons as primary charge carriers results in higher avalanche multiplication and lower excess noise, as is expected in an alloy where $\alpha >> \beta$. However, in the PIN structures, the difference in multiplication and noise performance between pure electron injection and slightly mixed injection conditions was minimal. This indicates that it is not critical to ensure pure electron conditions for low noise in this alloy.

The reduced effect of mixed injection in PIN851 compared to the PIN852, despite their similar structures, is likely due to the higher background *p*-type doping in the digital alloy. This causes the electric field to be tapered, with the highest field being closest to the junction with the n^+ cladding layer.

Pure electron injection noise is shown for structures of each thickness in figure 5.15, with other published data for excess noise in this alloy. Our results are in some disagreement with those from the literature. The structure reported by Lee *et al.* is the same wafer referred to as PIN851 in this work and after discussion with the authors we believe our results to be a correction to those previously published. The difference is due to Lee *et al.* processing noise data by normalising gain and excess noise to a single data point which is taken to constitute 'unity gain.' The disadvantages of this method compared to the use of a linear baseline correction are described in chapter 3. The reason for the discrepancy between our results for PIN3 and those for the structure reported by Taylor-Mew *et al.*, which is of an almost identical thickness and yielded almost identical multiplication data to that of PIN853, is not clear. For the purposes of this discussion, we have assumed that our results are representative of the bulk characteristics of $\mathrm{Al_{0.85}Ga_{0.15}AsSb}$ for the range of structure thicknesses shown.

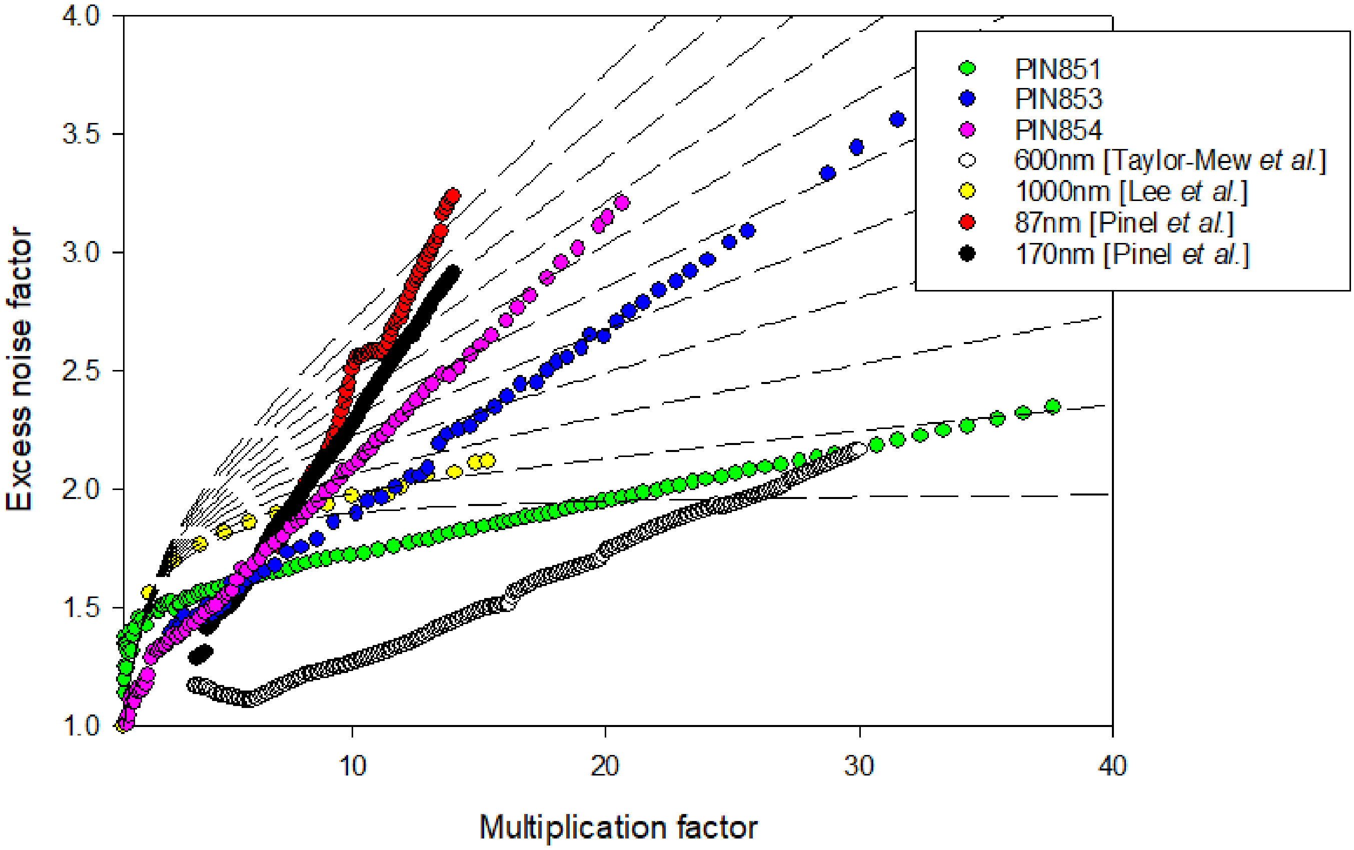

Figure 5.15: Excess noise factor data for PIN851, PIN853, and PIN854 under pure injection conditions, shown with data from the literature for other $\mathrm{Al_{0.85}Ga_{0.15}AsSb}$ structures. Dashed lines represent the excess noise factor predicted by McIntyre's local model for k values of 0 to 0.1 in steps of 0.01.

Excess noise is seen to increase with decreasing structure thickness, which is expected given that α and β converge as electric field increases. However, the increase in noise is more significant than is predicted by theory, which has implications for device design. It is evident that the reduction in the α/β ratio as electric field increases has a more significant effect on the noise than the carrier dead space, which would be expected to reduce the noise in thinner structures. It is possible that even lower noise could be produced in a thicker structure, as is seen in AlAsSb.

The excess noise factor at a multiplication of 10 is shown as a function of structure thickness in figure 5.16. The measured values for excess noise factor are significantly lower than those predicted by the local model, indicating that the effects of the dead space in this alloy are significant. The relative change in excess noise factor with structure thickness is similar to that predicted by the local model. Simulated data from an RPL model using electron and hole ionisation threshold energies of 2.5eV overpredicts excess noise for the thicker structures, and underpredicts excess noise for the thinner structures. This indicates that the change in excess noise with structure thickness is greater than that predicted by standard dead space theory. As described in chapter 2, the RPL model uses the DSMT theory of Hayat *et al.* [83], [84]. This assumes that the probability of impact ionisation for a given carrier is zero before the carrier has traversed the dead space, and is then represented by an exponentially decaying PDF once the dead space has been traversed. The deviation of the model from our measured data indicates that this is an oversimplification of the actual ionisation PDF.

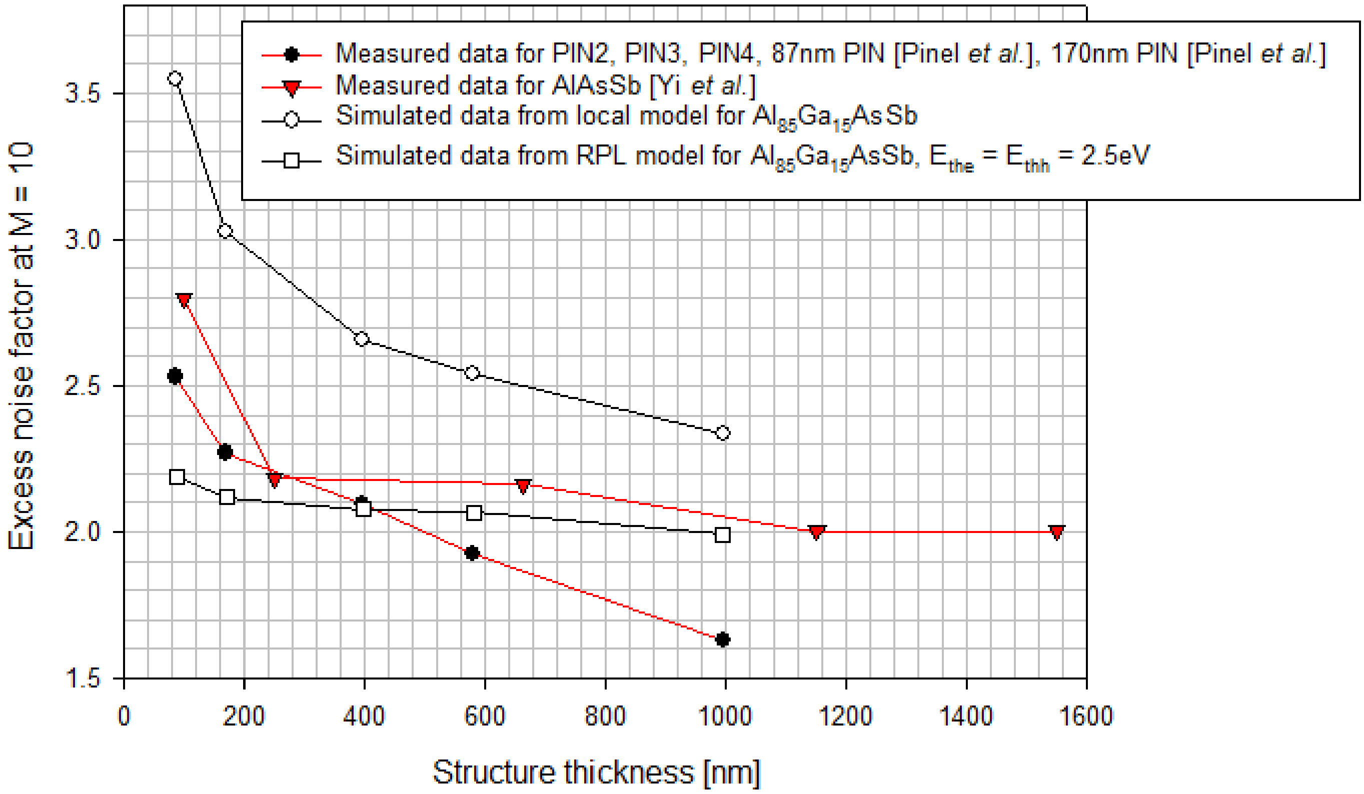

Figure 5.16: Excess noise factor at a multiplication factor of 10 for the RA PIN samples in this study, shown with simulated data from local and RPL models and measured data for AlAsSb [36].

Accurate modelling of excess noise in this alloy would therefore require a more complex and comprehensive model, using Monte-Carlo techniques or otherwise. This would incorporate the details of the alloy band-structure and the rates of various scattering mechanisms. Alloy scattering is likely to be significant, as the $Al_xGa_{1-x}As_ySb_{1-y}$ system has high alloy disorder potential. This is due to the large differences between the radii of the different atoms in the quaternary system, in particular the As and Sb atoms. A Simple Monte-Carlo model for $Al_{0.85}Ga_{0.15}AsSb$ has been proposed by Taylor-Mew *et al.* [92]. This model fitted to the excess noise data previously published by these authors, which disagrees with our measured data for a similar structure, and to that of Pinel *et al.* [152]. Excess noise data for thicker structures was not used. More modelling studies are required in order to comprehensively predict the noise behaviour in this alloy, and this is considered to be beyond the scope of this work.

The characteristics displayed by this alloy necessitate a compromise between the optimal noise performance, as well as increased sensitivity, in thicker structures against the generally higher speed of thinner structures. In cases where the device size and series resistance results in a bandwidth that is RC limited, thicker structures will also result in a higher bandwidth due to reduced capacitance. The bandwidth simulations in this chapter consider homojunction PIN structures only. An SACM structure incorporating an absorber region will be thicker, and will therefore have a lower transit-time limited bandwidth and a higher RC limited bandwidth – this may necessitate a thinner multiplication region.

The appropriate choice of structure thickness will vary for different device applications and careful design based on the prioritisation of performance metrics will be necessary. High-speed applications such as optical communications may require a sacrifice in noise performance and sensitivity for optimal bandwidth. Conversely, applications such as LiDAR systems SPADs will require maximum sensitivity, with bandwidth being less critical. FSO systems may require large optical window sizes, in which case bandwidth is likely to be limited by device capacitance and thicker structures can be employed for maximum sensitivity.

The noise characteristics do not appear to improve with the use of a digital alloy, as is true in $Al_xGa_{1-x}As$ but not in InAlAs [23], [169]. Random alloy growth is therefore likely to be a preferable option to digital alloy growth due to the lower defect densities in random alloy crystal structures.

Chapter 6: Multiplication and excess noise in $Al_{0.75}Ga_{0.25}As_{0.56}Sb_{0.44}$ and $Al_{0.55}Ga_{0.45}As_{0.56}Sb_{0.44}$

6.1 Introduction

This chapter is an analysis of complementary, nominally 1.55µm thick PIN and NIP structures of $Al_{0.75}Ga_{0.25}As_{0.56}Sb_{0.44}$ ($Al_{0.75}Ga_{0.25}AsSb$) and $Al_{0.55}Ga_{0.45}As_{0.56}Sb_{0.44}$ ($Al_{0.55}Ga_{0.45}AsSb$), reporting measurements of multiplication and excess noise under pure injection conditions in the PIN structures and a range of injection conditions in the NIP structures. Impact ionisation coefficients have been derived from the pure injection multiplication data from both alloys. These coefficients are compared with those of $AlAs_{0.56}Sb_{0.44}$ and $Al_{85}Ga_{15}As_{0.56}Sb_{0.44}$ and their changes with alloy composition are discussed and compared to those of AlGaAs and AlGaInP.

6.2 Motivations

The work in chapters 4 and 5 has provided a comprehensive analysis of the noise characteristics of $Al_{0.85}Ga_{0.15}AsSb$ and a discussion of how impact ionisation behaviour changes with aluminium/gallium ratio in AlGaInP and AlGaAs. There has thus far been no research into the bulk characteristics of $Al_xGa_{1-x}AsSb$ with $x < 0.85$. Decreasing aluminium content further would carry several advantages. Dark current in $Al_{0.85}Ga_{0.15}AsSb$ devices remains dominated by surface effects, even for a relatively well optimised fabrication process. Additionally, we have observed that $Al_{0.85}Ga_{0.15}AsSb$ devices degrade significantly over time. This can occur even if the devices are surface passivated. Other advantages of reducing aluminium content are lower device operating voltages and absorption at longer wavelengths. If a wide β/α ratio can be maintained with a sufficiently low band-gap for infrared absorption, then it would be possible to design a low noise, high sensitivity infrared detector without the need to employ an SACM structure, which complicates growth. In addition to the practical benefits of lower-aluminium alloys, investigating how the impact ionisation characteristics change with alloy composition may shed light on possible mechanisms for the very wide α/β ratio seen in the high-aluminium AlGaAsSb alloys. This would aid in the design of future high-performance detector materials.

6.3 Wafer and device details

The AlGaAsSb wafers were grown as digital alloys by molecular beam epitaxy on n^+-InP and p^+-InP substrates for the PIN and NIP structures respectively. The wafers consisted of 300nm top cladding and 200nm bottom cladding layers around a 1.55um unintentionally doped region. They also included highly doped 20nm top and 400nm bottom InGaAs contact layers. The wafers were fabricated at the University of Cardiff using standard wet etching with an HCl-based etchant. Standard circular mesa diodes structures were produced with diameters 90, 140, 240 and 440nm, with titanium/gold top and bottom contacts. The device sidewalls were passivated with SU-8 and coated with gold to prevent side injection. The region thicknesses and dopings were verified using capacitance-voltage measurements and are listed in table 6.1. Static dielectric constants of 11.75 for $x = 0.75$ and 12.38 for $x = 0.55$ were interpolated from those for AlAsSb and GaAsSb, which are given in section 5.5. A general schematic of these wafers is shown in figure 6.1.

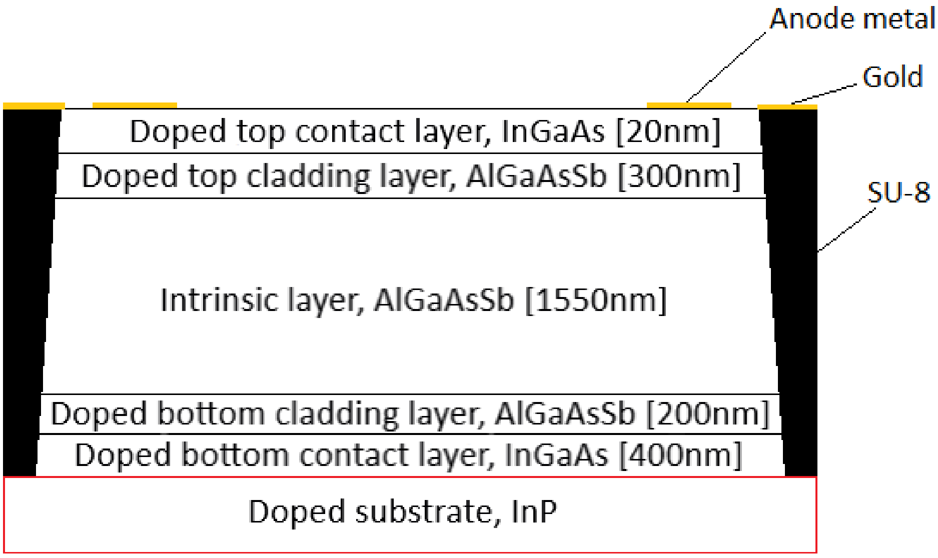

Figure 6.1: Schematic diagram of the AlGaAsSb PIN and NIP wafers used in this study, with nominal layer thicknesses.

TABLE 6.1

PARAMETERS OF AL$_{0.55}$GA$_{0.45}$AS$_{0.56}$SB$_{0.44}$ AND AL$_{0.55}$GA$_{0.45}$AS$_{0.56}$SB$_{0.44}$WAFERS USED IN THIS STUDY

Sample	Aluminium fraction, x	Calculated intrinsic region width, w [µm]	N_i [x10^{15}cm^{-3}] ± 1x10^{15}cm^{-3}	N_p [x10^{17}cm^{-3}] ± 1x10^{17}cm^{-3}
PIN751	0.75	1.50	15	30
NIP751	0.75	1.47	15	30
PIN551	0.55	1.50	20	10
NIP551	0.55	1.50	14	10

6.4 Dark I-V and C-V measurements

6.4.1 Dark I-V measurements

Reverse bias dark current data for PIN751 and NIP751 are shown in figure 6.2. The dark current for all measured devices was below 1µA at 95% of breakdown voltage. The dark currents scale with perimeter for both wafers, indicating the dominance of surface dark currents. The breakdown voltage in the PIN structure is higher due to the thicker intrinsic region.

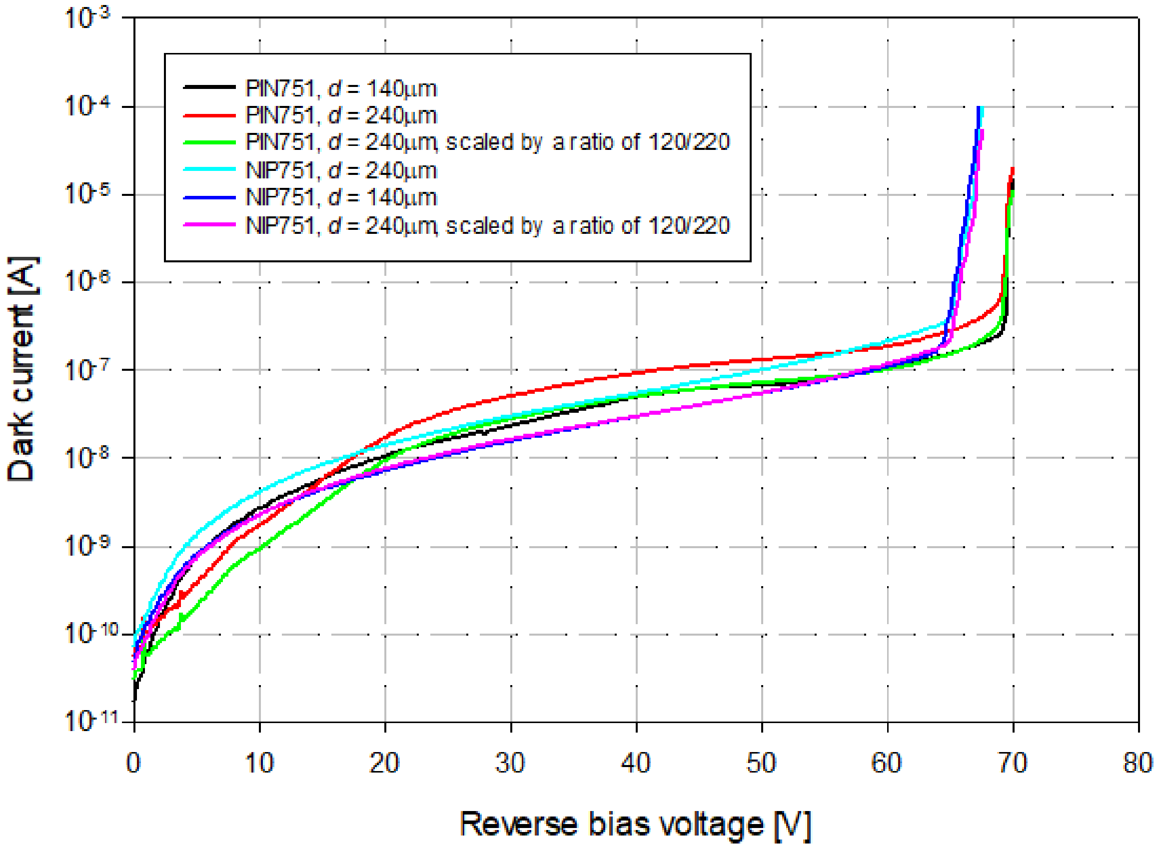

Figure 6.2: Reverse dark current-voltage characteristics for PIN751 and NIP751.

Reverse bias dark current data for PIN551 and NIP551 are shown in figure 6.3. The dark currents in the PIN structure were low, below 100nA at 95% of breakdown voltage. However, the dark currents in this structure scale with device perimeter. This indicates that surface leakage currents continue to dominate even at this lower aluminium concentration. The dark currents in the NIP structure were significantly higher and were not consistent even for devices of the same diameter, suggesting non-uniformity in the dark current mechanisms across the wafer. The NIP structure has a higher breakdown voltage, despite being of similar thickness, which is attributed to lower background doping in the intrinsic region.

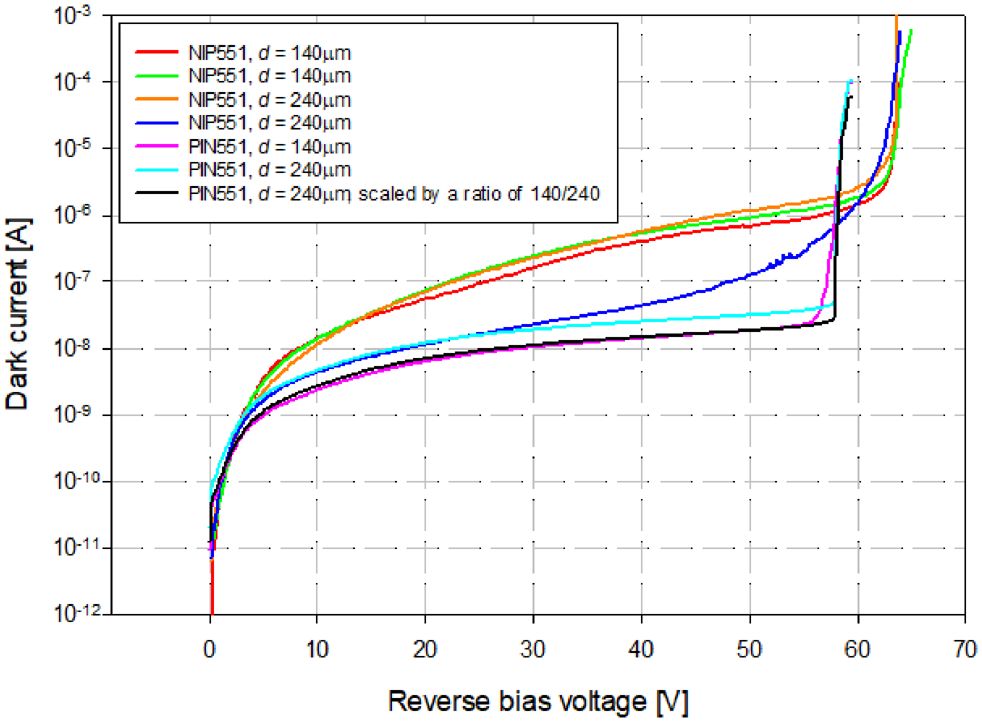

Figure 6.3: Reverse dark current-voltage characteristics for PIN551 and NIP551.

Forward bias characteristics for each $Al_{0.75}Ga_{0.25}AsSb$ and $Al_{0.55}Ga_{0.45}AsSb$ wafer used in this study are given in figure 6.4. These data indicate that the series resistance for these samples was of an order of magnitude low enough to avoid the distortion of excess noise measurements.

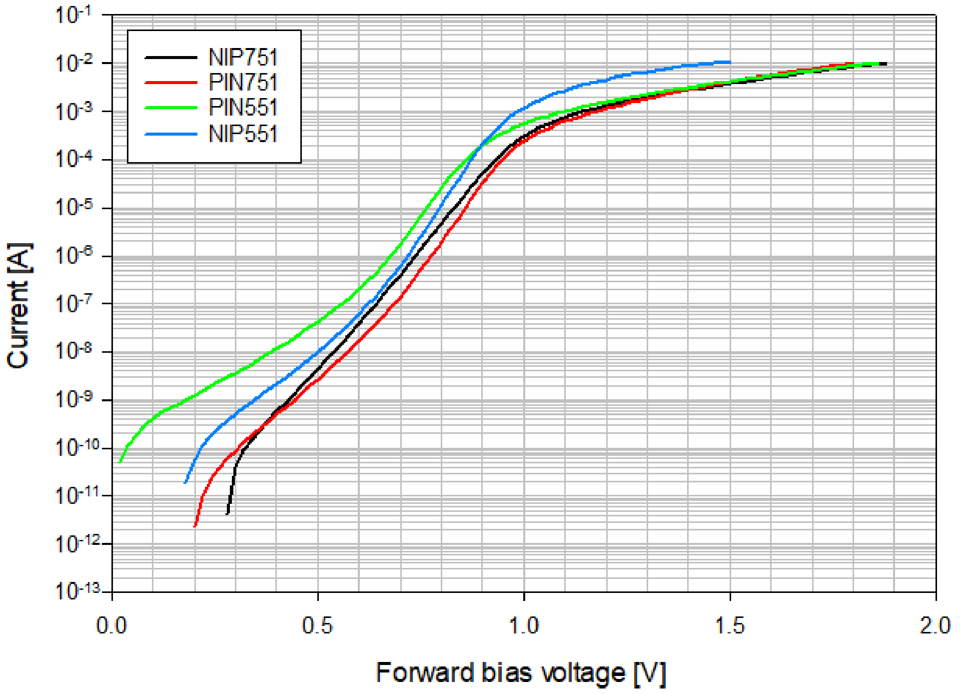

Figure 6.4: Forward dark current-voltage characteristics for PIN751, NIP751, PIN551, and NIP551. All measurements are for 240µm diameter devices.

6.4.2 C-V measurements

Capacitance-voltage measurements for PIN751, NIP751, PIN551 and NIP551 are shown in figure 6.5. These results indicate that the intrinsic regions of PIN751 and NIP751 do not become fully depleted until the reverse bias voltage is greater than approximately 35V. This is indicative of relatively high background doping in the intrinsic regions. The relatively small change in capacitance after this point indicates that depletion into the cladding layers is minimal, indicating high doping in these layers. The capacitance at bias voltages >35V was slightly higher in NIP751 than in PIN751, indicating that it has a thinner intrinsic region than the PIN structure.

The intrinsic region of PIN551 is fully depleted at approximately 30V and that of NIP551 is fully depleted at approximately 25V. The capacitances at bias voltages greater than these values were similar. This indicates that the structures have intrinsic regions of similar thicknesses and that the background doping in the PIN structure is slightly higher. Both structures showed a minimal change in capacitance once the intrinsic regions were fully depleted, indicating high doping in the cladding regions.

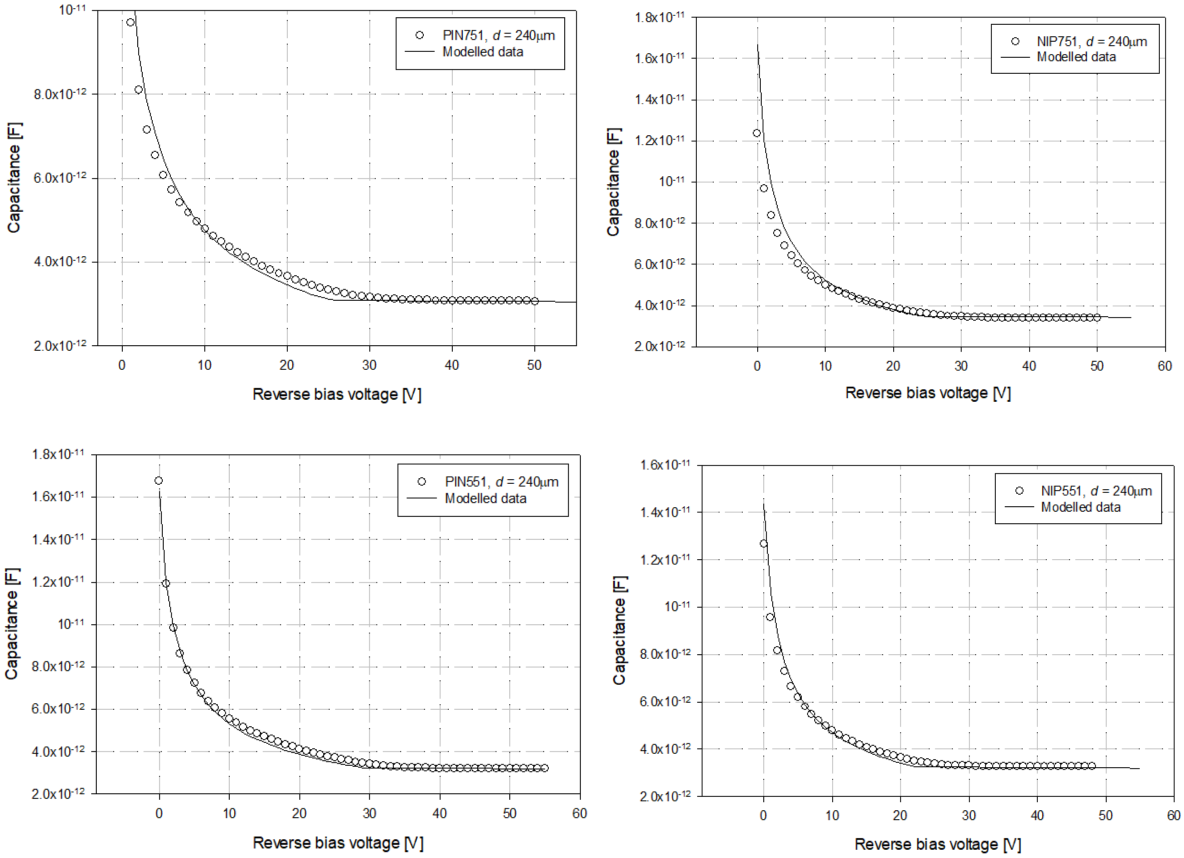

Figure 6.5: Reverse capacitance-voltage characteristics for the AlGaAsSb wafers used in this study.

6.5 Multiplication measurements

6.5.1 Determination of unity gain photocurrent in structures with high background doping

Some uncertainty in the determination of the multiplication factor is introduced due to avalanche multiplication onsetting at a voltage where the structure is not fully depleted. This makes it difficult to discern the true unity gain photocurrent of the device, as increases in photocurrent may be attributed either to avalanche multiplication or to increased collection efficiency by the electric field.

The background doping in these samples is considered to be p-type, as is generally the case in antimonide material. This is thought to be due to Ga or Sb vacancies in the crystal lattice [170]. This is corroborated by the multiplication and noise data, as shown below. The polarity of the background doping means that the p-n junctions in the PIN samples are at the opposite end of the device to where the carriers are being injected. This means that carrier collection efficiency changes significantly as the width of the depletion region increases. This is because carriers generated in the p^+ cladding must drift further to be collected by the electric field when the high field region does not extend to the full width of the intrinsic region. This effect is responsible for the 'droop' seen at lower voltages on the multiplication characteristics.

The result of this is that there is a significant part of the photocurrent characteristic where current is increasing with voltage due to two mechanisms: that of avalanche gain, and that of increasing collection efficiency. It is necessary to precisely determine the rate of increase due to the changing collection efficiency in order to accurately calculate the primary photocurrent, and therefore the avalanche multiplication factor. This is particularly critical for the interpretation of excess noise data because small errors in the calculation of multiplication factor can have a significant effect on calculated excess noise factor, as described in chapter 3.

Liu *et al.* [15] have reported an algorithm which allows the multiplication and excess noise factor to be solved for analytically using measured data for photocurrent and noise power as a function of bias voltage. This algorithm has not been used in this case as it relies on the use of McIntyre's local model equation [1], which will not be accurate for wide band-gap materials in which the effects of the carrier dead space are significant.

The primary photocurrent for pure injection in the PIN structures were therefore calculated using Woods' equation [76] as described in section 3.4. This equation, given again as equation 6.1, relates the primary photocurrent as a function of the minority carrier generation rate at one end of the device, the minority carrier diffusion length, and the position of the depletion region edge relative to the width of the device.

$$J_{pi} = \frac{qG_0}{\cosh(L-L_{\mathrm{pn}})} \quad (6.1)$$

Where J_{pi} is the primary photocurrent, q is the electronic charge, G_0 is the minority carrier generation rate at one edge of the device, L_{pn} is the minority carrier diffusion length, and L is the distance between the edge of the device, where carriers are injected, and the edge of the depletion region. The depletion region width (W) was calculated as a function of bias voltage from the C-V characteristic, and the total distance between the carrier generation point and the *p-n* junction (L_0) was taken as the sum of the widths of the intrinsic and p^+ cladding regions. The intrinsic region width used was that calculated from the C-V measurement, and the nominal p^+ region width was used. W is then subtracted from L_0 to give L. G_0 and L_{pn} are used as modifiable parameters to fit the calculated primary photocurrent to the initial part of the measured photocurrent data, where impact ionisation has not initiated. This method relies on several assumptions: firstly, the equation assumes that carriers are generated uniformly at the edge of the region where light is injected. This means that very short wavelength light must be used, as even if all optical absorption occurs in the top cladding layer, resulting in pure electron injection, some carriers may be being absorbed close to the junction between the p^+ cladding layer and the intrinsic layer. This also means that it is not possible to use this method to calculate the primary photocurrent under mixed injection conditions. The calculation also assumes the nominal width of the p^+ region is correct. It is not possible to directly determine the width of the p^+ region from the C-V measurement because it does not become fully depleted at fields below the avalanche breakdown voltage. The final assumption is that the depletion into the n^+ bottom cladding layer is negligible. This assumption is considered acceptable due to the high cladding layer doping indicated by the minimal change in the device capacitance at reverse bias voltages above those at which the intrinsic region becomes fully depleted. Additionally, if this assumption were incorrect, the result would be a smaller change in the value of L at high bias voltages, because a higher proportion of the cladding depletion would be occurring in the n^+ cladding. As the change in L is already minimal at these voltages, this would not have a significant effect on the final multiplication and noise results inferred using the calculated primary photocurrent.

This analysis was performed on pure injection photocurrent data for PIN751 and PIN551. Short wavelength light was used to ensure that carriers were absorbed close to the device surface. A 420nm fibre-coupled LED was used for to illuminate PIN751, and a 455nm fibre-coupled LED was used to illuminate PIN551. The measured photocurrent data are shown with the calculated primary photocurrents in figures 6.6 and 6.7.

A G_0 of $4.5\text{x}10^{14}\text{m}^{-2}$ and an L_{pn} of 360nm were used for PIN751, and a G_0 of $2.5\text{x}10^{12}\text{m}^{-2}$ and an L_{pn} of 680nm were used for PIN551. The minority carrier diffusion lengths are affected by the defect concentration in a given device, meaning that the values used here are considered to be wafer-specific rather than necessarily representative of the bulk characteristics of the alloy. The carrier generation rate G_0 is here considered to be the rate of carriers generated in the device that do not recombine at the surface.

This effect of the moving depletion edge is less problematic in the NIP structures, as the *p-n* junction is at the same end of the device as where the carriers are being injected. This means that carriers absorbed in the n^+ cladding do not need to drift a significant distance to be collected by the electric field. Additionally, carrier injection in the NIP structures has a majority of holes as initiating carriers. This means that multiplication is lower and begins at higher electric fields. These factors mean that the primary photocurrent in the NIP structures could be calculated using the linear approximation to Woods' equation, which can be inferred empirically from the region of the photocurrent characteristic where the intrinsic region of the structure is fully depleted but impact ionisation has not begun. This allowed accurate calculation of the multiplication and noise characteristics under both pure and mixed carrier injection conditions.

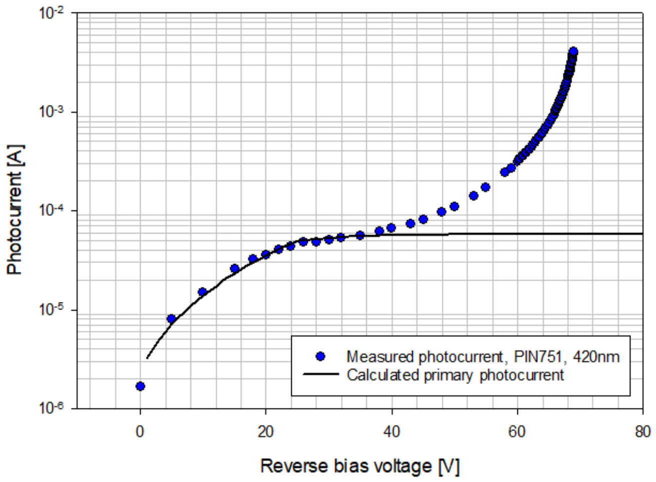

Figure 6.6: Photocurrent for PIN751 under 420nm illumination, shown with primary photocurrent calculated using Woods' equation.

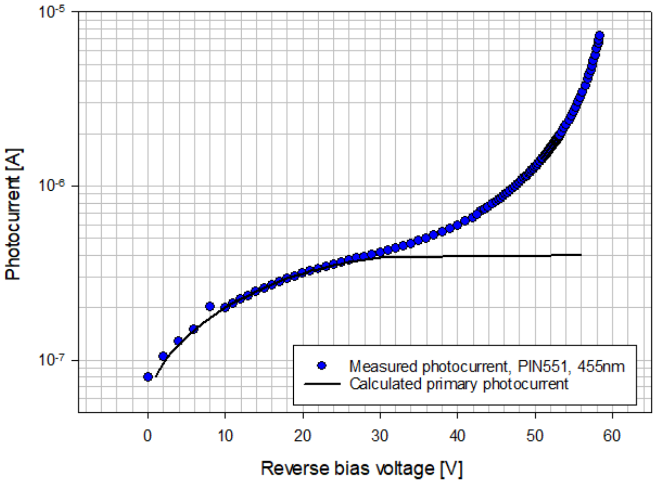

Figure 6.7: Photocurrent for PIN551 under 455nm illumination, shown with primary photocurrent calculated using Woods' equation.

6.5.2 Multiplication results

M-1 curves for PIN751 under pure injection conditions, and for NIP751 under a range of injection conditions, are shown in figure 6.8. A 420nm fibre-coupled LED was used to illuminate the PIN device for pure electron injection. This ensured that carriers were absorbed as close to the top surface of the p^+ cladding layer as possible to improve the accuracy of the calculated primary photocurrent. The NIP structure was illuminated with a 455nm LED for pure injection, and with a 543nm He-Ne laser and 625nm and 850nm LEDs to produce mixed injection conditions. A 455nm LED was used as the signal intensity was higher due to reduced surface recombination, resulting in better measurement accuracy at low multiplication values. The results for the PIN structure are for pure injection conditions as it was not possible to calculate the primary photocurrent under mixed injection conditions. The highest multiplication was observed for pure injection in the PIN structure (pure electron injection), and the lowest was observed for pure injection in the NIP structure (pure hole injection). The multiplication for the NIP structure has significant wavelength dependence, with more mixed injection conditions (which have a higher proportion of electron-initiated impact ionisation events) producing higher multiplication, and the most mixed injection conditions yielded multiplication similar results to those for pure electron injection. This indicates that the avalanche multiplication process is dominated by electron-initiated events, as is the case in AlAsSb and $Al_{0.85}Ga_{0.15}AsSb$.

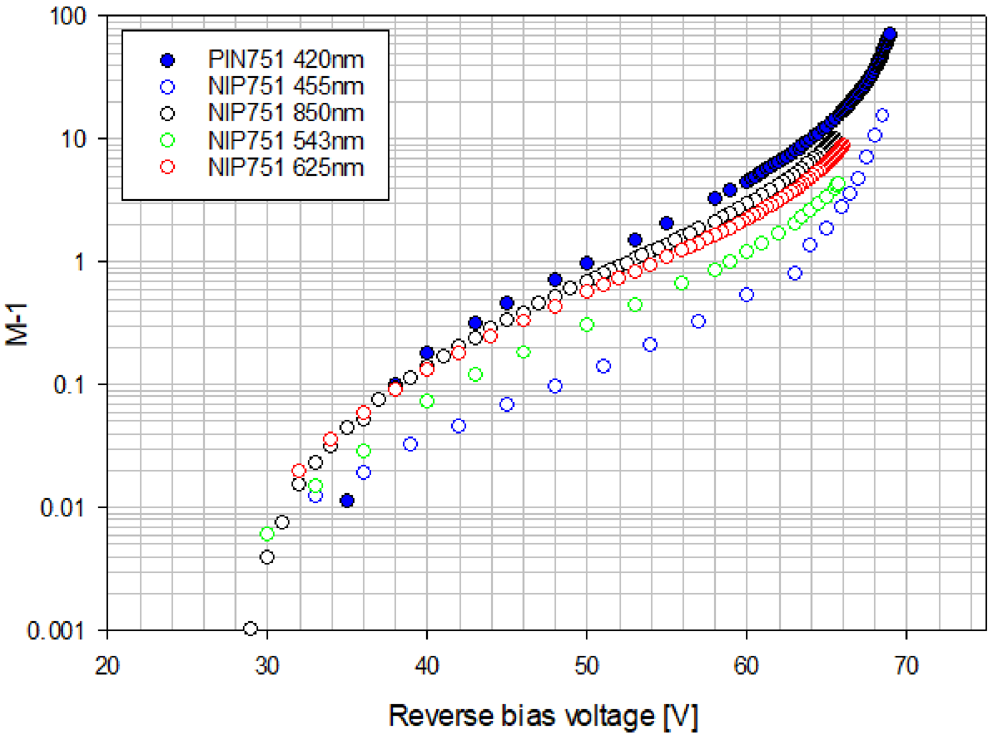

Figure 6.8: Multiplication data for PIN751 under pure electron injection conditions and for NIP751 under a range of injection conditions, shown in the form M-1.

M-1 curves for PIN551 under pure injection conditions, and for NIP551 under a range of injection conditions, are shown in figure 6.9. A 455nm LED was used to illuminate both devices for pure injection conditions, and 625nm, 780nm, and 940nm LEDs were used to produce variously mixed injection conditions in the NIP structure. The multiplication under pure electron injection conditions remains significantly higher than that under pure hole injection, indicating that $\alpha > \beta$ for this alloy. However, the multiplication under mixed injection in NIP551 is lower than that seen in NIP751, with the most mixed injection profile producing multiplication that is only slightly closer to the M_e than it is to the M_h. This indicates that electron-initiated ionisation events do not dominate in $Al_{0.55}Ga_{0.45}AsSb$ to the same extent that they do in the higher-aluminium AlGaAsSb alloys.

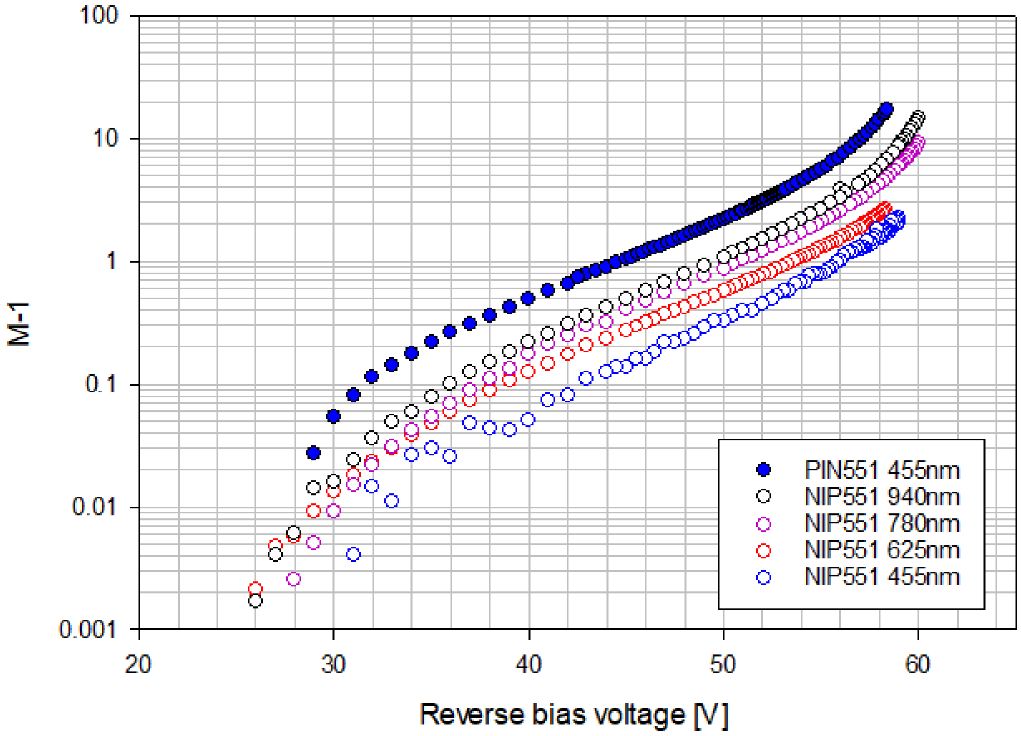

Figure 6.9: Multiplication data for PIN551 under pure electron injection conditions and for NIP551 under a range of injection conditions, shown in the form M-1.

6.6 Excess noise measurements

Excess noise measurements for these wafers were performed using the system after Li, as described in chapter 3. The same light sources were used to illuminate the devices as for the multiplication measurements.

Excess noise data are shown in figures 6.10-6.13. The excess noise for PIN751 under pure electron conditions is low, equivalent to that predicted by McIntyre's local model for a k of 0 at M = 20 and for a k of 0.02 at M = 60. The noise data is comparable to that of the 870nm $Al_{0.85}Ga_{0.15}AsSb$ PIN structure (PIN851) measured in chapter 5 up to an M of approximately 20, becoming higher as multiplication increases. Excess noise in NIP751 under pure hole injection conditions is high, equivalent to that predicted for a k of 40-50. This is slightly lower than that observed in PIN851 and given in chapter 5. The excess noise in NIP751 decreases significantly with increasingly mixed injection conditions, and is equivalent to that predicted for an effective k of 1.1, 0.3, and 0.12 under 543nm, 625nm, and 850nm illumination respectively.

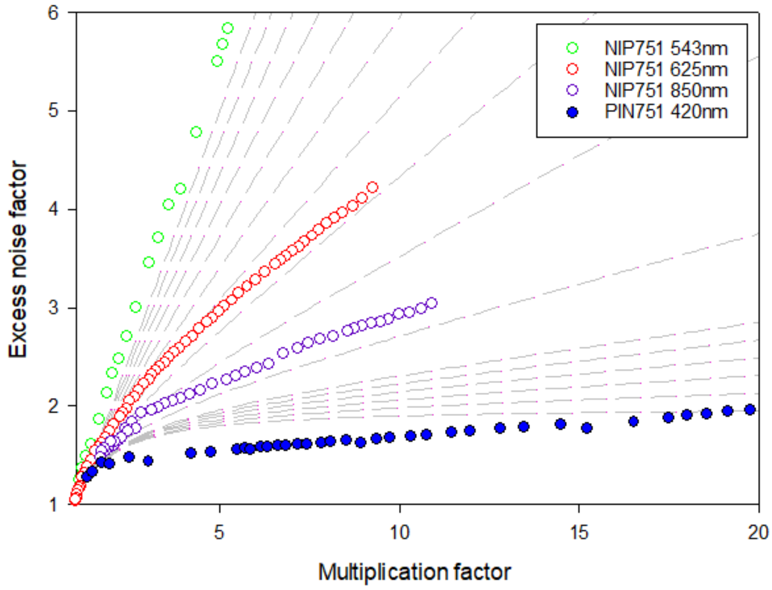

Figure 6.10: Excess noise data for PIN751 under pure electron injection conditions and for NIP751 under a range of mixed injection conditions. Dashed lines represent the noise predicted by McIntyre’s local model for k values of 0 to 0.05 in steps of 0.01, and 0.1 to 1 in steps of 0.1.

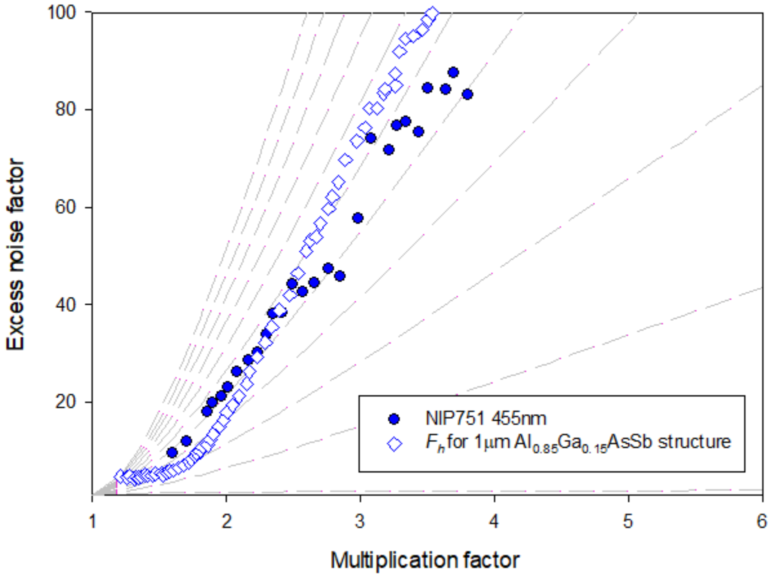

Figure 6.11: Excess noise data for NIP751 under pure injection conditions shown with F_h data for a nominally 1μm thick $Al_{0.85}Ga_{0.15}AsSb$ NIP structure for comparison. Dashed lines represent the noise predicted by McIntyre’s local model for k values of 0 to 100 in steps of 10.

The pure electron injection excess noise measured in PIN551 is higher than that in PIN751, equivalent to that predicted by McIntyre for a *k* of 0 at M = 7 and to a *k* of 0.04 at M = 15. The excess noise under mixed injection conditions in NIP551 was approximately equivalent to that predicted for a *k* of 0.25 at 940nm, 0.3 at 780nm, and 0.5 at 625nm. The noise for the most mixed injection conditions is higher than that measured under equivalent injection conditions in NIP751.

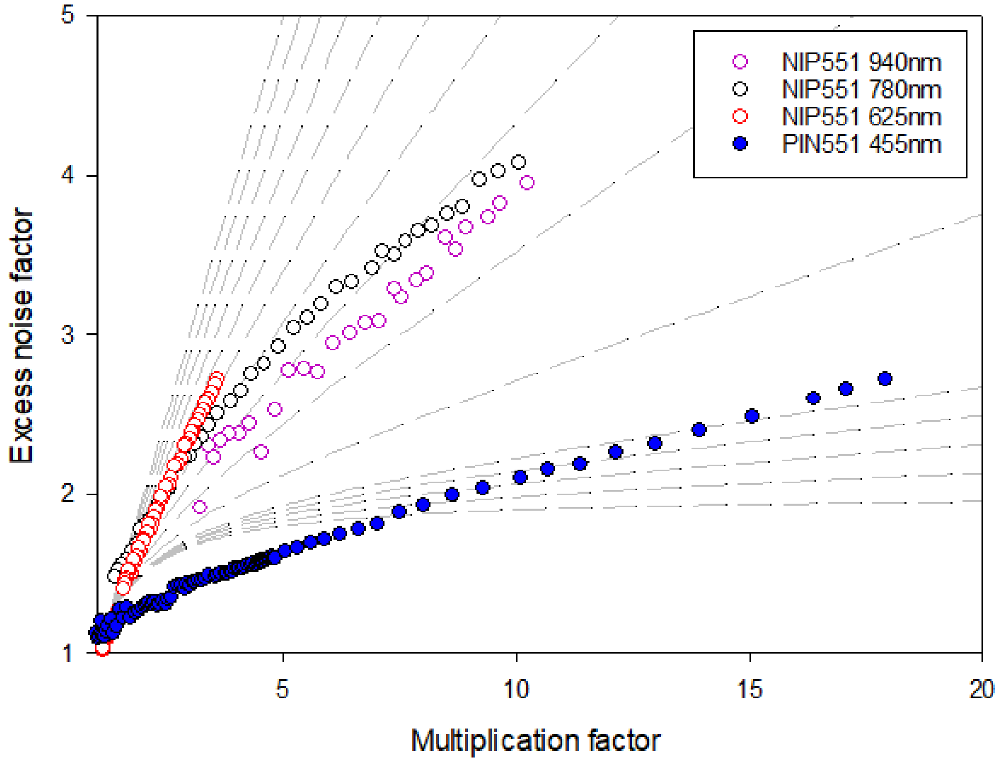

Figure 6.12: Excess noise data for PIN551 under pure electron injection conditions and for NIP551 under a range of mixed injection conditions. Dashed lines represent the noise predicted by McIntyre's local model for *k* values of 0 to 0.05 in steps of 0.01, and 0.1 to 1 in steps of 0.1.

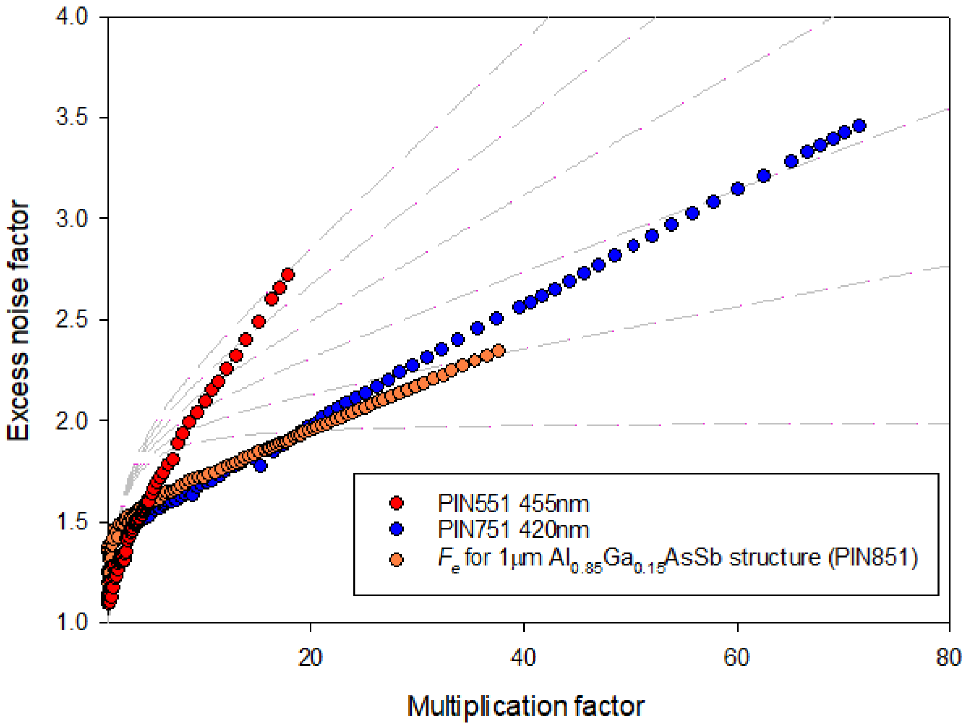

Figure 6.13: Excess noise data for PIN751 and PIN551 under pure injection conditions, shown with F_e data for a nominally 1μm thick $Al_{0.85}Ga_{0.15}AsSb$ PIN structure for comparison. Dashed lines represent the noise predicted by McIntyre's local model for k values of 0 to 0.05 in steps of 0.01.

6.7 Discussion and extraction of impact ionisation coefficients

These results indicate that $Al_{0.75}Ga_{0.25}AsSb$ has a wide α/β ratio, in common with the higher-aluminium compounds in this alloy system that have previously been studied. The excess noise is observed to be very low under pure electron injection conditions and very high under pure hole electron conditions, and the multiplication under pure electron injection conditions is significantly higher than under pure hole injection conditions. A small amount of mixed injection in the NIP structure increases multiplication and reduces excess noise considerably, which indicates the dominance of electron initiated ionisation events. This behaviour is consistent with, and similar to, that observed in the $Al_{0.85}Ga_{0.15}AsSb$ structures reported in chapter 5. However, it is notable that the $Al_{0.75}Ga_{0.25}AsSb$ structures measured here are significantly thicker than the 1μm $Al_{0.85}Ga_{0.15}AsSb$ structure to which the results are comparable. Given that, in AlAsSb and $Al_{0.85}Ga_{0.15}AsSb$, the α/β ratio increases significantly with decreasing electric field, the excess noise characteristics would be expected to improve with increasing structure thickness if the α/β ratio in $Al_{0.75}Ga_{0.25}AsSb$ were similar to that in $Al_{0.75}Ga_{0.25}AsSb$. It is possible that the excess noise is increased due to the reduced effects of dead space in the thicker structure, but this is unlikely given that noise is observed to decrease with increasing structure thickness in $Al_{0.85}Ga_{0.15}AsSb$. The dead space would also be expected to have a more significant effect in Al$_{0.85}$Ga$_{0.15}$AsSb due to its wider band-gap, and the fact that the structures studied are thinner.

Figure 6.14 shows pure injection multiplication for PIN751 and NIP751 alongside several sets of simulated multiplication data. All of the simulated data was produced using a local model using the fitted parameters for each Al$_{0.75}$Ga$_{0.25}$AsSb structure. Multiplication data generated using the impact ionisation coefficients for Al$_{0.85}$Ga$_{0.15}$AsSb shows a significantly higher breakdown voltage than that measured for these structures. This indicates that breakdown voltage decreases with the decrease in minimum energy band-gap as x becomes lower, and does not exhibit the saturation effect seen at high aluminium concentrations in AlGaAs and AlGaInP. Figure 6.14 also shows multiplication data simulated using the Al$_{0.85}$Ga$_{0.15}$AsSb ionisation coefficients scaled linearly by a factor of 1.3, which compensates for the change in band-gap without altering the α/β ratio. This provides a good fit to the measured data for M_e, but the simulated M_h is significantly lower than that measured. This indicates that β is relatively higher in Al$_{0.75}$Ga$_{0.25}$AsSb than in Al$_{0.85}$Ga$_{0.15}$AsSb.

The simulated M_e and M_h were iteratively fitted to the measured data to yield a set of impact ionisation coefficients for Al$_{0.75}$Ga$_{0.25}$AsSb, which are given in equations 6.2 and 6.3 in the form of standard Chynoweth expression, $\alpha(\beta) = Aexp(-(\frac{B}{\xi})^C)$:

$$\alpha = 5.5 \times 10^5 exp\left(-\left[\frac{1.20\times10^6}{\xi}\right]^{1.43}\right) cm^{-1} \quad (6.2)$$

$$\beta = 1.7425 \times 10^5 exp\left(-\left[\frac{1.42\times10^6}{\xi}\right]^{1.42}\right) cm^{-1} \quad (6.3)$$

Where ξ is electric field in V/cm.

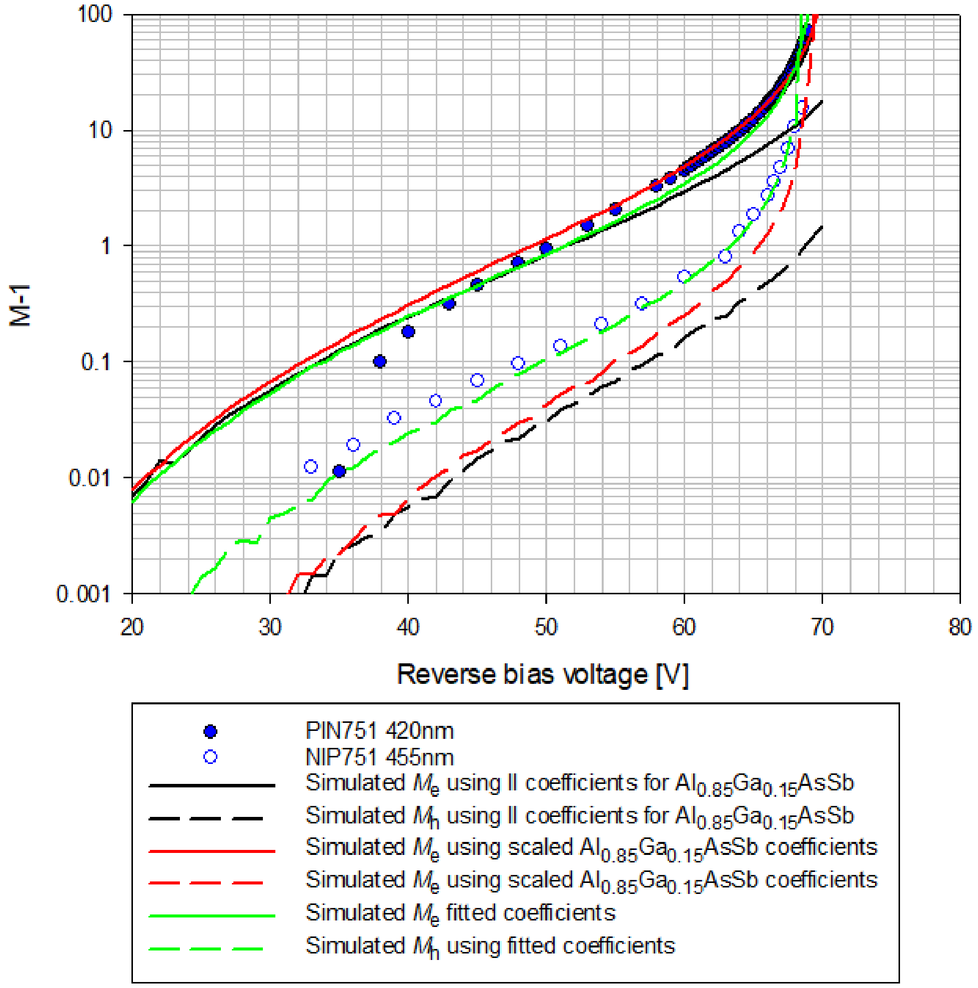

Figure 6.14: Multiplication data for PIN751 and NIP751 under pure injection conditions, shown with simulated multiplication data for their respective structure details using (i) the impact ionisation coefficients of $Al_{0.85}Ga_{0.15}AsSb$, (ii) the impact ionisation coefficients of $Al_{0.85}Ga_{0.15}AsSb$ with a linear scaling factor applied, and (iii) the fitted ionisation coefficients for $Al_{0.75}Ga_{0.25}AsSb$. All data are given in the form M-1.

The measured multiplication data deviate from the simulated data at low multiplication values, which is considered acceptable because the method of calculating primary photocurrent using Woods' equation generates less accurate data close to the onset of multiplication. This is because the equation models the p^+ cladding region and the *p*-type unintentionally doped region as distinct, with a step change in doping between them. In the real case, the doping will grade continuously between the cladding and the unintentionally doped region. This means that the calculated primary photocurrent characteristic will have a sharp corner at the point at which the unintentionally doped region becomes fully depleted, which will cause error in the multiplication data close to this point. This is the case in both PIN751 and PIN551.

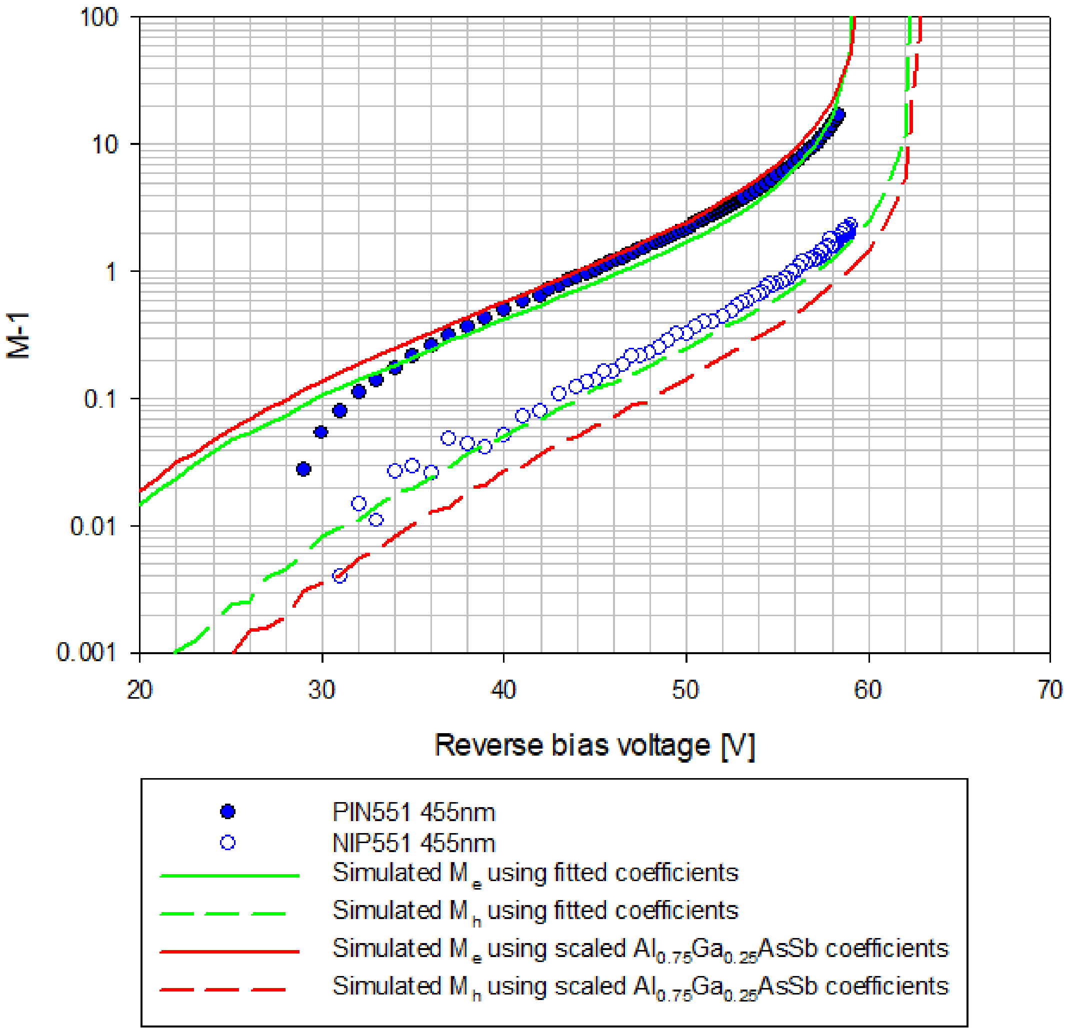

Figure 6.15: Multiplication data for PIN551 and NIP551 under pure injection conditions, shown with simulated multiplication data for their respective structure details using (i) the fitted ionisation coefficients for Al$_{0.55}$Ga$_{0.45}$AsSb and (ii) the impact ionisation coefficients of Al$_{0.75}$Ga$_{0.25}$AsSb with a linear scaling factor applied. All data are given in the form M-1.

The above process was repeated to extract impact ionisation coefficients for Al$_{0.55}$Ga$_{0.45}$AsSb. The pure injection multiplication data for PIN551 and NIP551 are shown with simulated data in figure 6.15. The breakdown voltage for the Al$_{0.55}$Ga$_{0.45}$AsSb structures was lower than that of the Al$_{0.75}$Ga$_{0.25}$AsSb structures despite their similar thickness, indicating that the impact ionisation coefficients continue to increase as the energy band-gap decreases. The ionisation coefficients for Al$_{0.75}$Ga$_{0.25}$AsSb were scaled by a factor of 1.6 to produce simulated data which matched the breakdown voltage for PIN551, and these were used as a starting point to iteratively fit a set of coefficients. The M_h data simulated using the scaled Al$_{0.75}$Ga$_{0.25}$AsSb coefficients was lower than the measured data, indicating that β is greater in Al$_{0.55}$Ga$_{0.45}$AsSb than in Al$_{0.75}$Ga$_{0.25}$AsSb. The fitted coefficients are given in equations 6.4 and 6.5 in the form of the standard Chynoweth expression as shown above.

$$\alpha = 6.3 \times 10^5 exp\left(-\left[\frac{1.20\times10^6}{\xi}\right]^{1.42}\right) cm^{-1} \quad (6.4)$$

$$\beta = 3.5 \times 10^5 exp\left(-\left[\frac{1.30\times10^6}{\xi}\right]^{1.46}\right) cm^{-1} \quad (6.5)$$

Where ξ is electric field in V/cm.

The fitted coefficients for $Al_{0.75}Ga_{0.25}AsSb$ and $Al_{0.55}Ga_{0.45}AsSb$ are valid for the electric field range for which accurate multiplication data is available for these structures, which is approximately 250-450kV/cm. Measurements of structures of different thicknesses would be required to confirm the values of α and β outside this range. The fitted ionisation coefficients are shown in figure 6.16 as a function of inverse electric field, alongside those for AlAsSb and $Al_{0.85}Ga_{0.15}AsSb$.

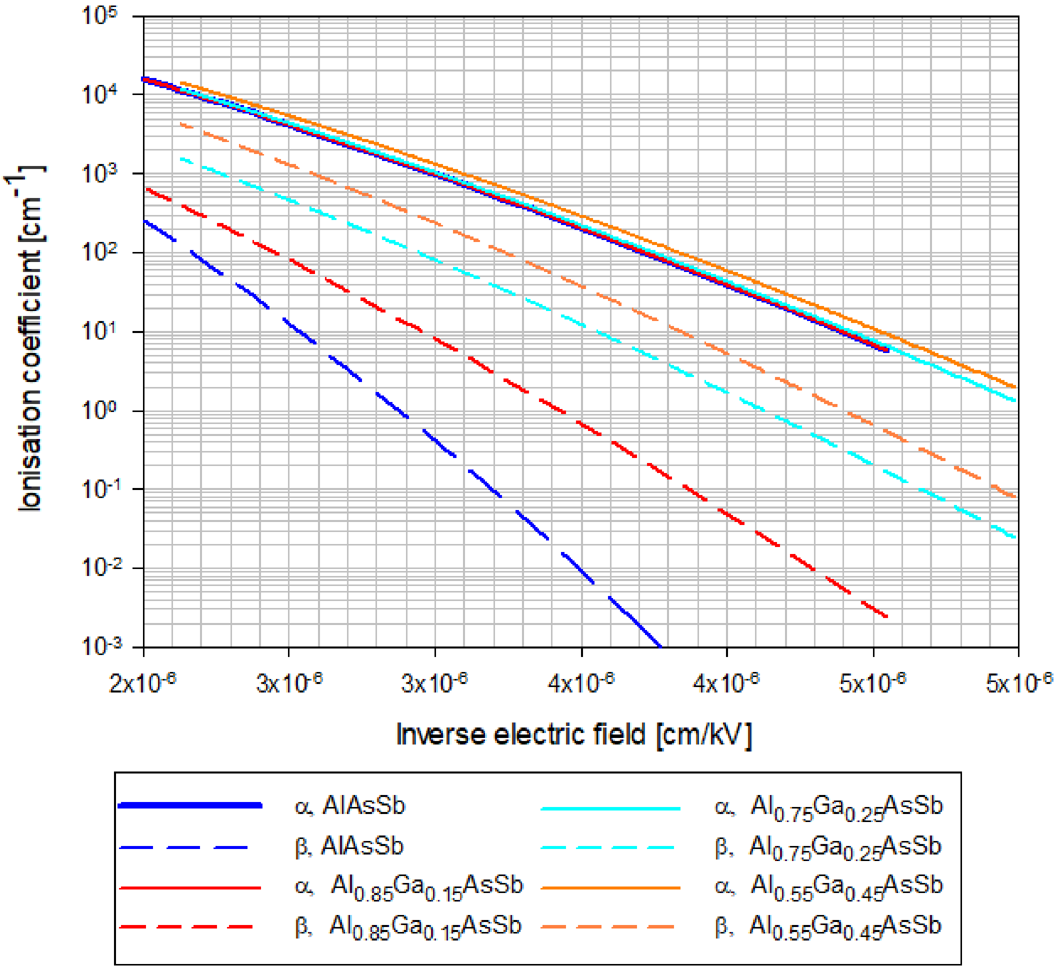

Figure 6.16: Impact ionisation coefficients for $Al_{0.75}Ga_{0.25}AsSb$ and $Al_{0.55}Ga_{0.45}AsSb$ shown as a function of inverse electric field, with those for $Al_{0.85}Ga_{0.15}AsSb$ and AlAsSb included for comparison.

The electron impact ionisation coefficient for $Al_{0.75}Ga_{0.25}AsSb$ is similar to those of AlAsSb and $Al_{0.85}Ga_{0.15}AsSb$ for this electric field range, becoming slightly higher as electric field decreases. That for $Al_{0.55}Ga_{0.45}AsSb$ is higher than for the other compositions by a factor of approximately 1.15. The hole impact ionisation coefficient for $Al_{0.75}Ga_{0.25}AsSb$ is significantly higher than that of $Al_{0.85}Ga_{0.15}AsSb$, with a similar relative change that observed between AlAsSb and $Al_{0.85}Ga_{0.15}AsSb$. That for $Al_{0.55}Ga_{0.25}AsSb$ is higher again, but with a smaller relative change. α and β are shown as a function of x in figure 6.17, for electric fields of 250 and 400 kV/cm. This suggests that α/β decreases significantly with x for this alloy system, meaning that the lower aluminium content AlGaAsSb alloys are unlikely to be suitable for extremely high performance APDs. The α/β ratio of $Al_{0.75}Ga_{0.25}AsSb$ is comparable to that of InAlAs, making it unlikely to warrant a significant improvement over current technology. It is, however, notable that the F_e measured here is significantly lower, and that the measured F_h is significantly higher, than that which is predicted by theory given the α/β ratio implied by the disparity between the M_e and M_h. This may indicate either that the α/β ratio is larger than we believe, or that an alternative mechanism of noise suppression exists in this alloy. The low noise may also be a consequence of reduced carrier feedback due to the high background doping in these structures. Due to the *p*-type background doping in the intrinsic regions of the PIN structures, the electric field in the high field region is tapered with the highest field being observed closest to the junction with the *n*-type cladding layer. This means that secondary holes will be travelling towards a region of lower electric field, making them less likely to impact ionise. This effect is similar to that observed in PIN851 as described in chapter 5, although in the latter case it was only significant under mixed injection conditions.

The $Al_{0.75}Ga_{0.25}AsSb$ and $Al_{0.55}Ga_{0.25}AsSb$ structures measured here also showed significant surface dark currents, suggesting that the aluminium content in this alloy is not low enough to prevent surface oxidation. Given that device performance appears to decrease with decreasing x, reduction of surface dark currents by improved device fabrication and passivation processes is likely to yield better results than further reductions in aluminium content.

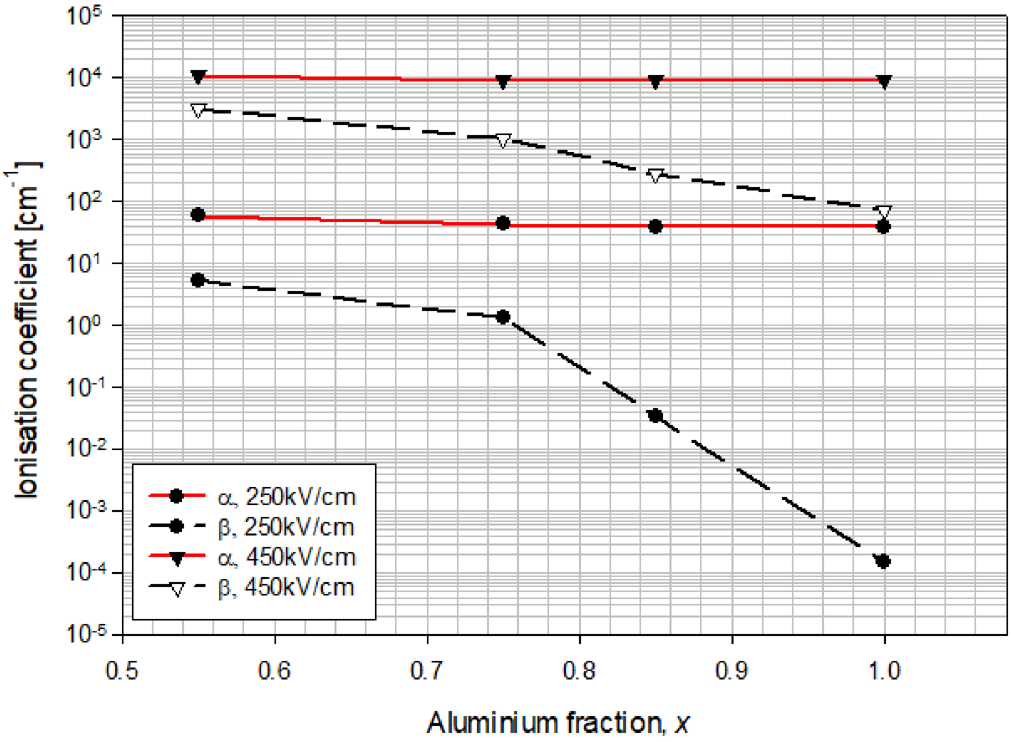

Figure 6.17: Impact ionisation coefficients for $Al_xGa_{1-x}AsSb$ as a function of *x*, at electric fields of 250 and 450kV/cm.

Chapter 7: Conclusions and further work

7.1 Summary of results

Chapter 4 of this work is an investigation into the varying impact ionisation characteristics of $(Al_xGa_{1-x})InP$ with changing alloy composition. Nominally 1µm PIN structures were measured for seven different alloy compositions with x of 0, 0.31, 0.47, 0.61, 0.64, 0.78, and 1. The excess noise factor of these samples decreases with increasing x up to $x = 0.64$, after which it does not show further significant decrease. The relative change in excess noise factor between $x = 0.61$ and $x = 0.64$ is also significantly greater than that at lower aluminium fractions. The impact ionisation coefficients for each of the measured alloy compositions were extracted using an RPL model from pure electron injection multiplication and noise data. Both α and β decrease as x increases, with β decreasing at a higher rate. β is also seen to decrease significantly between $x = 0.61$ and $x = 0.64$, and decreases minimally at higher aluminium fractions. α does not exhibit this decrease, meaning that the α/β ratio in this alloy system becomes significantly larger when x increases above this threshold. The electric field at which avalanche breakdown occurs increases with increasing x up to $x = 0.64$, but does not continue to increase at higher aluminium fractions. The threshold of alloy composition at which the α/β ratio saturates and the breakdown field saturates is the same as is observed in $Al_xGa_{1-x}As$. It is hypothesised that this threshold may be due to the Γ energy gap becoming sufficiently larger than the X energy gap that it is no longer involved in the impact ionisation process.

Chapter 5 is a detailed study of the alloy $Al_{0.85}Ga_{0.15}AsSb$, which focuses on the variation in excess noise factor in random and digital alloy PIN structures, and one NIP structure, of different thicknesses and under different injection conditions. The excess noise in the thickest structures was equivalent to that predicted by McIntyre’s local model for an effective k of 0 at approximately $M = 20$ under pure electron injection conditions. Excess noise factor increases with decreasing structure thickness and with an increasing proportion of holes as primary carriers. The excess noise in the NIP structure was high, corresponding to that predicted for an effective k of approximately 50. Excess noise factor is found not to vary significantly between random and digital alloy structures which are otherwise equivalent. The shape of the excess noise factor characteristic does not correspond to that predicted by McIntyre’s local model or to that predicted by an RPL model. Multiplication data for these structures indicates that gain increases with an increasing proportion of electrons as primary carriers. Multiplication and noise under weakly mixed injection conditions was similar to that under pure injection conditions in the PIN structures, but significantly different in the NIP structure. This indicates that electron-initiated ionisation events heavily dominate. Impact ionisation coefficients for this alloy have been extracted using a local model and multiplication data for the structures studied here and for others which have been reported in the literature. α is very similar to that observed in

AlAsSb, and β is greater than that observed in AlAsSb. The transit-time limited bandwidths for PIN structures of varying thickness have been theoretically calculated using an RPL model input with the fitted ionisation coefficients. These are compared with the RC time constant limited bandwidth for devices of varying size (with a nominal resistance of 50Ω) and it is observed that devices will be limited by the RC time constant in most cases.

Chapter 6 is a study of the impact ionisation characteristics of $Al_{0.75}Ga_{0.25}AsSb$ and $Al_{0.55}Ga_{0.45}AsSb$, with the intention of investigating how the properties of the $Al_xGa_{1-x}AsSb$ system change with varying alloy composition. Complementary PIN and NIP structures with a nominal thickness of 1500nm were studied for both alloys. Multiplication and excess noise factor were measured under a range of injection conditions. A higher proportion of electrons as primary carriers gives higher gain and lower noise in both alloys, but this effect becomes weaker as aluminium content decreases. Impact ionisation coefficients have been extracted from the multiplication data for these alloys under pure electron and pure hole injection conditions. α for $Al_{0.75}Ga_{0.25}AsSb$ is similar to that observed in $Al_{0.85}Ga_{0.15}AsSb$ and AlAsSb, and that for $Al_{0.55}Ga_{0.45}AsSb$ is slightly higher. β increases significantly with decreasing aluminium content. Excess noise in both $Al_{0.75}Ga_{0.25}AsSb$ and $Al_{0.55}Ga_{0.45}AsSb$ was lower under pure electron injection conditions than is predicted by theory given the extracted impact ionisation coefficients.

In summary, this work has produced detailed characterisations of the impact ionisation behaviour of $(Al_xGa_{1-x})InP$ across the full composition range and $Al_xGa_{1-x}AsSb$ for $x \geq 0.55$. For $(Al_xGa_{1-x})InP$ the critical finding is that the α/β ratio does not change linearly with aluminium composition but instead shows a rapid increase at a particular composition, with little further change as aluminium content continues to increase. This indicates that the performance advantages associated with AlInP can be maintained while decreasing the aluminium content significantly, which will improve the ease of growth and the reliability of devices. The characteristics of this alloy also shed light on a possible mechanism for the suppression of hole-initiated impact ionisation in other low-noise alloys. Namely, the Γ band-gap increases sufficiently beyond the size of the X band-gap that the Γ valley is no longer relevant to the impact ionisation process. This has a more significant effect on electrons than holes because of the smaller number of possible positions in *k*-space from which holes can initiate impact ionisation events in III-V alloys.

In $Al_xGa_{1-x}AsSb$, this work has shown the clear trend that excess noise in $Al_{0.85}Ga_{0.15}AsSb$ decreases with increasing structure thickness, which will inform the design of SACM structures incorporating this alloy. It is also shown that the excess noise characteristics deviate from those predicted by local and RPL models, indicating that the displaced-exponential probability distribution function used to model impact ionisation is not sufficiently accurate for this alloy. The work on $Al_{0.75}Ga_{0.25}AsSb$ and

$Al_{0.55}Ga_{0.45}AsSb$ has shown that the α/β ratio in this alloy increases with decreasing aluminium content, and that excess noise factor increases. This means that, contrary to for $(Al_xGa_{1-x})InP$, decreasing aluminium content does not appear to be a viable solution to the problems of surface leakage current and poor device reliability in these alloys. Improved device passivation techniques are likely to be a more useful avenue in this regard. However, the excess noise in the lower-aluminium $Al_xGa_{1-x}AsSb$ alloys does not increase to the degree that would be expected given the decrease in α/β ratio. This further indicates that the ionisation probability distributions assumed by existing models, assuming an exponential distribution which is displaced by a factor proportional to the dead space, are not sufficiently accurate to model noise in these allots. More detailed models will therefore be required in order to more completely understand the mechanisms of impact ionisation in this and other low-noise alloy systems.

7.2 Further work

The results reported in this thesis provide a foundation for the design of SWIR-detecting SAM-APD structures incorporating $(Al_xGa_{1-x})InP$ or $Al_xGa_{1-x}AsSb$ multipliers. The lower-aluminium $Al_xGa_{1-x}AsSb$ alloys which have been studied, $Al_{0.75}Ga_{0.25}AsSb$ and $Al_{0.55}Ga_{0.45}AsSb$, show a narrower α/β ratio and higher excess noise than $Al_{0.85}Ga_{0.15}AsSb$ without a significant reduction of surface effects. This indicates that these alloys are unlikely to be the optimal choice in high-performance SWIR APDs. However, given that the data presented here have been measured from limited number of structures, it would be prudent to investigate more structures of different thicknesses to more thoroughly characterise the ionisation coefficients of these alloys across a wide electric field range. It would also be useful to investigate the band-gaps of these alloys, and how the Γ and X energy gaps vary with alloy composition in $Al_xGa_{1-x}AsSb$. This would provide further information as to the validity of the hypothesis that the suppression of hole impact ionisation in some III-V alloys occurs when the Γ energy gap is sufficiently larger than the X energy gap. This may inform the design of new e-APD materials based on theoretical knowledge of alloy band-structures.

An appropriate next step would be the growth and characterisation of an $Al_{0.85}Ga_{0.15}AsSb$ SAM-APD structure incorporating an appropriate narrow band-gap absorber. For FSO communications or LiDAR use a thick multiplier would give the highest sensitivity, and a 1µm absorber would be a suitable choice. Given that excess noise factor reduces significantly with increasing multiplier thickness, it would also be of interest to investigate thicker PIN structures of this alloy. It is notable that, in AlAsSb, a 1.55µm thick sample displayed significantly lower excess noise than a 1µm thick sample, and the similar trend in the ionisation coefficients of $Al_{0.85}Ga_{0.15}AsSb$ with respect to electric field indicate that this would likely to also be the case for the latter. For fibre-optic communications the use of a thinner structure may be necessary in order to achieve maximum bandwidth. The use of thicker structures, which reduces the transit-time limited bandwidth, will increase the RC limited bandwidth due to lower capacitance. Optimal structure thickness can therefore be determined based on specified bandwidth and the minimum necessary device diameter. This will also depend on the details of the absorption, charge sheet, cladding, and buffer regions of the structure. It will also be necessary to investigate improved passivation techniques in order to minimise surface dark currents and improve device reliability to a commercially feasible level.

It would also be of interest to investigate a GaAs-based SACM structure utilising a GaNAsSb or GaSb absorption region and a thin $(Al_xGa_{1-x})InP$ multiplication region. GaSb would be an appropriate choice for an absorption material due to its relative ease of growth compared to GaNAsSb. In order to be competitive with $Al_xGa_{1-x}As$, a design would be required to use very thin multiplication layers in order to take advantage of the negligible dark currents in thin $(Al_xGa_{1-x})InP$ structures. It may be useful to grow and characterise very thin (10-25nm) $(Al_xGa_{1-x})InP$ PIN structures with $x = 0.65$-0.75 in order to determine the excess noise exhibited by such a structure.

References

[1] A. Rogalski, ‘HgCdTe infrared detector material: history, status and outlook’, *Rep. Prog. Phys.*, vol. 68, no. 10, pp. 2267–2336, Aug. 2005, doi: 10.1088/0034-4885/68/10/R01.

[2] R. J. McIntyre, ‘Multiplication noise in uniform avalanche diodes’, *IEEE Trans. Electron Devices*, vol. ED-13, no. 1, pp. 164–168, Jan. 1966, doi: 10.1109/T-ED.1966.15651.

[3] Y. Hochberg, I. Charaev, S.-W. Nam, V. Verma, M. Colangelo, and K. K. Berggren, ‘Detecting Sub-GeV Dark Matter with Superconducting Nanowires’, *Phys. Rev. Lett.*, vol. 123, no. 15, p. 151802, Oct. 2019, doi: 10.1103/PhysRevLett.123.151802.

[4] J.-P. Chen *et al.*, ‘Sending-or-Not-Sending with Independent Lasers: Secure Twin-Field Quantum Key Distribution over 509 km’, *Phys. Rev. Lett.*, vol. 124, no. 7, p. 070501, Feb. 2020, doi: 10.1103/PhysRevLett.124.070501.

[5] L. Chen *et al.*, ‘Ultra-sensitive mid-infrared emission spectrometer with sub-ns temporal resolution’, *Opt. Express*, vol. 26, no. 12, pp. 14859–14868, Jun. 2018, doi: 10.1364/OE.26.014859.

[6] E. T. Khabiboulline, J. Borregaard, K. De Greve, and M. D. Lukin, ‘Optical Interferometry with Quantum Networks’, *Phys. Rev. Lett.*, vol. 123, no. 7, p. 070504, Aug. 2019, doi: 10.1103/PhysRevLett.123.070504.

[7] M. E. Grein *et al.*, ‘An optical receiver for the Lunar Laser Communication Demonstration based on photon-counting superconducting nanowires’, vol. 9492, p. 949208, May 2015, doi: 10.1117/12.2179781.

[8] A. McCarthy *et al.*, ‘Kilometer-range, high resolution depth imaging via 1560 nm wavelength single-photon detection’, *Opt. Express*, vol. 21, no. 7, pp. 8904–8915, Apr. 2013, doi: 10.1364/OE.21.008904.

[9] A. Tosi, S. Cova, F. Zappa, M. A. Itzler, and R. Ben-Michael, ‘InGaAs/InP Single Photon Avalanche Diode Design and Characterization’, in *2006 European Solid-State Device Research Conference*, Sep. 2006, pp. 335–338. doi: 10.1109/ESSDER.2006.307706.

[10] Y. G. Xiao and M. J. Deen, ‘Frequency response and modeling of resonant-cavity separate absorption, charge, and multiplication avalanche photodiodes’, *J. Light. Technol.*, vol. 19, no. 7, pp. 1010–1022, Jul. 2001, doi: 10.1109/50.933297.

[11] R. B. Emmons, ‘Avalanche-Photodiode Frequency Response’, *J. Appl. Phys.*, vol. 38, no. 9, pp. 3705–3714, Aug. 1967, doi: 10.1063/1.1710199.

[12] M. J. Ahmed, ‘Temperature dependence of electron impact ionization coefficient in bulk silicon’, Erbil, Kurdistan, Iraq, 2017, p. 020034. doi: 10.1063/1.5004311.

[13] M. Ershov and V. Ryzhii, ‘Temperature dependence of the electron impact ionization coefficient in silicon’, *Semicond. Sci. Technol.*, vol. 10, no. 2, pp. 138–142, Feb. 1995, doi: 10.1088/0268-1242/10/2/003.

[14] H. B. Briggs, ‘Infrared Absorption in High Purity Germanium’, *JOSA*, vol. 42, no. 9, p. 686_3-687, Sep. 1952, doi: 10.1364/JOSA.42.0686_3.

[15] J. B. D. Soole and H. Schumacher, ‘InGaAs metal-semiconductor-metal photodetectors for long wavelength optical communications’, *IEEE J. Quantum Electron.*, vol. 27, no. 3, pp. 737–752, Mar. 1991, doi: 10.1109/3.81384.

[16] J. Liu *et al.*, ‘High-performance, tensile-strained Ge p-i-n photodetectors on a Si platform’, *Appl. Phys. Lett.*, vol. 87, no. 10, p. 103501, Sep. 2005, doi: 10.1063/1.2037200.

[17] N. Susa, H. Nakagome, O. Mikami, H. Ando, and H. Kanbe, ‘New InGaAs/InP avalanche photodiode structure for the 1-1.6 µm wavelength region’, *IEEE J. Quantum Electron.*, vol. 16, no. 8, pp. 864–870, Aug. 1980, doi: 10.1109/JQE.1980.1070588.

[18] L. W. Cook, G. E. Bulman, and G. E. Stillman, ‘Electron and hole impact ionization coefficients in InP determined by photomultiplication measurements’, *Appl. Phys. Lett.*, vol. 40, no. 7, pp. 589–591, Apr. 1982, doi: 10.1063/1.93190.

[19] J. C. Campbell, S. Chandrasekhar, W. T. Tsang, G. J. Qua, and B. C. Johnson, ‘Multiplication noise of wide-bandwidth InP/InGaAsP/InGaAs avalanche photodiodes’, *J. Light. Technol.*, vol. 7, no. 3, pp. 473–478, Mar. 1989, doi: 10.1109/50.16883.

[20] Y. L. Goh *et al.*, ‘Excess Avalanche Noise in In0.52Al0.48As’, *Quantum Electron. IEEE J. Of*, vol. 43, pp. 503–507, Jul. 2007, doi: 10.1109/JQE.2007.897900.

[21] N. Li *et al.*, ‘InGaAs/InAlAs avalanche photodiode with undepleted absorber’, *Appl. Phys. Lett.*, vol. 82, no. 13, pp. 2175–2177, Mar. 2003, doi: 10.1063/1.1559437.

[22] G. S. Kinsey, J. C. Campbell, and A. G. Dentai, ‘Waveguide avalanche photodiode operating at 1.55 µm with a gain-bandwidth product of 320 GHz’, *IEEE Photonics Technol. Lett.*, vol. 13, no. 8, pp. 842–844, Aug. 2001, doi: 10.1109/68.935822.

[23] J. Zheng *et al.*, ‘Digital Alloy InAlAs Avalanche Photodiodes’, *J. Light. Technol.*, vol. 36, no. 17, pp. 3580–3585, Sep. 2018, doi: 10.1109/JLT.2018.2844114.

[24] S. Lee *et al.*, ‘Engineering of impact ionization characteristics in In 0.53 Ga 0.47 As/Al 0.48 In 0.52 As superlattice avalanche photodiodes on InP substrate’, *Sci. Rep.*, vol. 10, no. 1, Art. no. 1, Oct. 2020, doi: 10.1038/s41598-020-73810-w.

[25] J. Beck *et al.*, ‘The HgCdTe electron avalanche photodiode’, *J. Electron. Mater.*, vol. 35, no. 6, pp. 1166–1173, Jun. 2006, doi: 10.1007/s11664-006-0237-3.

[26] Y. Lin *et al.*, ‘Minamata Convention on Mercury: Chinese progress and perspectives’, *Natl. Sci. Rev.*, vol. 4, no. 5, pp. 677–679, Sep. 2017, doi: 10.1093/nsr/nwx031.

[27] A. R. J. Marshall, J. P. R. David, and C. H. Tan, ‘Impact Ionization in InAs Electron Avalanche Photodiodes’, *IEEE Trans. Electron Devices*, vol. 57, no. 10, pp. 2631–2638, Oct. 2010, doi: 10.1109/TED.2010.2058330.

[28] L. W. Lim, C. H. Tan, J. S. Ng, J. D. Petticrew, and A. B. Krysa, ‘Improved Planar InAs Avalanche Photodiodes With Reduced Dark Current and Increased Responsivity’, *J. Light. Technol.*, vol. 37, no. 10, pp. 2375–2379, May 2019, doi: 10.1109/JLT.2019.2905535.

[29] S. Krishna *et al.*, ‘Linear Mode Avalanche Photodiodes with Antimonide Multipliers on InP Substrates’, *IEEE J. Quantum Electron.*, pp. 1–1, 2022, doi: 10.1109/JQE.2022.3162027.

[30] S. Maddox, S. March, and S. Bank, ‘Broadly Tunable AlInAsSb Digital Alloys Grown on GaSb’, 2016, doi: 10.1021/ACS.CGD.5B01515.

[31] M. E. Woodson, M. Ren, S. J. Maddox, Y. Chen, S. R. Bank, and J. C. Campbell, ‘Low-noise AlInAsSb avalanche photodiode’, *Appl. Phys. Lett.*, vol. 108, no. 8, p. 081102, Feb. 2016, doi: 10.1063/1.4942372.

[32] A. H. Jones, S. D. March, A. A. Dadey, A. J. Muhowski, S. R. Bank, and J. C. Campbell, ‘AlInAsSb Separate Absorption, Charge, and Multiplication Avalanche Photodiodes for Mid-Infrared Detection’, *IEEE J. Quantum Electron.*, pp. 1–1, 2022, doi: 10.1109/JQE.2022.3149532.

[33] K. Akahane, N. Yamamoto, S. Gozu, and N. Ohtani, ‘Heteroepitaxial growth of GaSb on Si(001) substrates’, *J. Cryst. Growth*, vol. 264, no. 1, pp. 21–25, Mar. 2004, doi: 10.1016/j.jcrysgro.2003.12.041.

[34] S. H. Kodati *et al.*, ‘AlInAsSb avalanche photodiodes on InP substrates’, *Appl. Phys. Lett.*, vol. 118, no. 9, p. 091101, Mar. 2021, doi: 10.1063/5.0039399.

[35] X. Yi *et al.*, ‘Demonstration of large ionization coefficient ratio in AlAs0.56Sb0.44 lattice matched to InP’, *Sci. Rep.*, vol. 8, no. 1, Dec. 2018, doi: 10.1038/s41598-018-27507-w.

[36] X. Yi *et al.*, ‘Extremely low excess noise and high sensitivity AlAs 0.56 Sb 0.44 avalanche photodiodes’, *Nat. Photonics*, vol. 13, no. 10, Art. no. 10, Oct. 2019, doi: 10.1038/s41566-019-0477-4.

[37] İ. H. Oğuzman, Y. Wang, J. Kolník, and K. F. Brennan, ‘Theoretical study of hole initiated impact ionization in bulk silicon and GaAs using a wave-vector-dependent numerical transition rate formulation within an ensemble Monte Carlo calculation’, *J. Appl. Phys.*, vol. 77, no. 1, pp. 225–232, Jan. 1995, doi: 10.1063/1.359374.

[38] Y. Liu *et al.*, ‘Valence band engineering of GaAsBi for low noise avalanche photodiodes’, *Nat. Commun.*, vol. 12, no. 1, Art. no. 1, Aug. 2021, doi: 10.1038/s41467-021-24966-0.

[39] X. Collins, ‘Dilute Nitride GaInNAsSb for Next Generation Optical Communications’, Ph.D., Lancaster University (United Kingdom), England, 2021. Accessed: May 24, 2022. [Online]. Available: https://www.proquest.com/docview/2566005259/abstract/B7FA3936EF1C4C65PQ/1

[40] F. P. Kapron, D. B. Keck, and R. D. Maurer, ‘Radiation losses in glass optical waveguides’, *Appl. Phys. Lett.*, vol. 17, no. 10, pp. 423–425, Nov. 1970, doi: 10.1063/1.1653255.

[41] The Photonics Leadership Group, ‘UK Photonics vision for 2035’, Nov. 2021. Accessed: Jul. 07, 2022. [Online]. Available: https://photonicsuk.org/wp-content/uploads/2021/10/Photonics_2035_Vision_Web_1.0.pdf

[42] ‘Optical Labs Set Terabit Transmission Records - IEEE Spectrum’, *IEEE Spectrum: Technology, Engineering, and Science News*. https://spectrum.ieee.org/tech-talk/computing/networks/optical-labs-set-terabit-transmission-records (accessed Mar. 10, 2021).

[43] S. Xie *et al.*, ‘InGaAs/AlGaAsSb avalanche photodiode with high gain-bandwidth product.’, *Opt. Express*, vol. 24, no. 21, pp. 24242–24247, 2016, doi: 10.1364/OE.24.024242.

[44] M. A. Khalighi and M. Uysal, ‘Survey on Free Space Optical Communication: A Communication Theory Perspective’, *IEEE Commun. Surv. Tutor.*, vol. 16, no. 4, pp. 2231–2258, 2014, doi: 10.1109/COMST.2014.2329501.

[45] W. S. Rabinovich *et al.*, ‘Free-space optical communications research and demonstrations at the U.S. Naval Research Laboratory’, *Appl. Opt.*, vol. 54, no. 31, pp. F189–F200, Nov. 2015, doi: 10.1364/AO.54.00F189.

[46] T. Tolker-Nielsen and G. Oppenhauser, ‘In-orbit test result of an operational optical intersatellite link between ARTEMIS and SPOT4, SILEX’, in *Free-Space Laser Communication Technologies XIV*, Apr. 2002, vol. 4635, pp. 1–15. doi: 10.1117/12.464105.

[47] V. W. S. Chan, ‘Optical satellite networks’, *J. Light. Technol.*, vol. 21, no. 11, pp. 2811–2827, Nov. 2003, doi: 10.1109/JLT.2003.819534.

[48] B. Smutny *et al.*, ‘5.6 Gbps optical intersatellite communication link’, in *Free-Space Laser Communication Technologies XXI*, Feb. 2009, vol. 7199, pp. 38–45. doi: 10.1117/12.812209.

[49] F. Arnold, M. Mosberger, J. Widmer, and F. Gambarara, ‘Ground receiver unit for optical communication between LADEE spacecraft and ESA ground station’, in *Free-Space Laser Communication and Atmospheric Propagation XXVI*, Mar. 2014, vol. 8971, pp. 152–164. doi: 10.1117/12.2039959.

[50] D. M. Boroson *et al.*, ‘Overview and results of the Lunar Laser Communication Demonstration’, in *Free-Space Laser Communication and Atmospheric Propagation XXVI*, Mar. 2014, vol. 8971, pp. 213–223. doi: 10.1117/12.2045508.

[51] E. Ciaramella *et al.*, ‘1.28-Tb/s (32 $\times$ 40 Gb/s) Free-Space Optical WDM Transmission System’, *IEEE Photonics Technol. Lett.*, vol. 21, no. 16, pp. 1121–1123, Aug. 2009, doi: 10.1109/LPT.2009.2021149.

[52] H. Henniger and O. Wilfert, ‘An Introduction to Free-space Optical Communications’, *Radioengineering J.*, vol. 19, pp. 203–212, Jun. 2010.

[53] J. Rothman, G. Lasfargues, and J. Abergel, ‘HgCdTe APDs for free space optical communications’, in *Unmanned/Unattended Sensors and Sensor Networks XI; and Advanced Free-Space Optical Communication Techniques and Applications*, Oct. 2015, vol. 9647, pp. 102–114. doi: 10.1117/12.2197171.

[54] R. T. H. Collis, ‘Lidar’, *Appl. Opt.*, vol. 9, no. 8, pp. 1782–1788, Aug. 1970, doi: 10.1364/AO.9.001782.

[55] N. R. Council, *Laser Radar: Progress and Opportunities in Active Electro-Optical Sensing*. 2014. doi: 10.17226/18733.

[56] Y. Li and J. Ibanez-Guzman, ‘Lidar for Autonomous Driving: The Principles, Challenges, and Trends for Automotive Lidar and Perception Systems’, *IEEE Signal Process. Mag.*, vol. 37, no. 4, pp. 50–61, Jul. 2020, doi: 10.1109/MSP.2020.2973615.

[57] X. Zhang, K. Kwon, J. Henriksson, J. Luo, and M. C. Wu, ‘A large-scale microelectromechanical-systems-based silicon photonics LiDAR’, *Nature*, vol. 603, no. 7900, Art. no. 7900, Mar. 2022, doi: 10.1038/s41586-022-04415-8.

[58] V. V. Meshcherinov, M. V. Spiridonov, V. A. Kazakov, and A. V. Rodin, ‘Lidar-based remote infrared gas sensor for monitoring anthropogenic pollution: a proof of concept’, *Quantum Electron.*, vol. 50, no. 11, p. 1055, Nov. 2020, doi: 10.1070/QEL17398.

[59] D. Shin *et al.*, ‘Photon-efficient imaging with a single-photon camera’, *Nat. Commun.*, vol. 7, no. 1, Art. no. 1, Jun. 2016, doi: 10.1038/ncomms12046.

[60] K. Morimoto *et al.*, ‘Megapixel time-gated SPAD image sensor for 2D and 3D imaging applications’, *Optica*, vol. 7, no. 4, pp. 346–354, Apr. 2020, doi: 10.1364/OPTICA.386574.

[61] M. Kutila, P. Pyykönen, H. Holzhüter, M. Colomb, and P. Duthon, ‘Automotive LiDAR performance verification in fog and rain’, in *2018 21st International Conference on Intelligent Transportation Systems (ITSC)*, Nov. 2018, pp. 1695–1701. doi: 10.1109/ITSC.2018.8569624.

[62] L. S. Rothman *et al.*, ‘The HITRAN 2004 molecular spectroscopic database’, *J. Quant. Spectrosc. Radiat. Transf.*, vol. 96, no. 2, pp. 139–204, Dec. 2005, doi: 10.1016/j.jqsrt.2004.10.008.

[63] G. Shen *et al.*, ‘High-speed airborne single-photon LiDAR with GHz-gated single-photon detector at 1550 nm’, *Opt. Laser Technol.*, vol. 141, p. 107109, Sep. 2021, doi: 10.1016/j.optlastec.2021.107109.

[64] W. Shockley and W. T. Read, ‘Statistics of the Recombinations of Holes and Electrons’, *Phys. Rev.*, vol. 87, no. 5, pp. 835–842, Sep. 1952, doi: 10.1103/PhysRev.87.835.

[65] C. Sah, R. N. Noyce, and W. Shockley, ‘Carrier Generation and Recombination in P-N Junctions and P-N Junction Characteristics’, *Proc. IRE*, vol. 45, no. 9, pp. 1228–1243, Sep. 1957, doi: 10.1109/JRPROC.1957.278528.

[66] L. V. Keldysh, ‘Behavior of Non-metallic Crystals in Strong Electric Fields’, *Sov. J. Exp. Theor. Phys.*, vol. 6, p. 763, Jan. 1958.

[67] A. Frova, P. Handler, F. A. Germano, and D. E. Aspnes, ‘Electro-Absorption Effects at the Band Edges of Silicon and Germanium’, *Phys. Rev.*, vol. 145, no. 2, pp. 575–583, May 1966, doi: 10.1103/PhysRev.145.575.

[68] J. P. Zheng, L. Shi, F. S. Choa, P. L. Liu, and H. S. Kwok, ‘Intensity-dependent photoluminescence spectra of semiconductor-doped glasses’, *Appl. Phys. Lett.*, vol. 53, no. 8, pp. 643–645, Aug. 1988, doi: 10.1063/1.100396.

[69] D. E. Aspnes, ‘Recombination at semiconductor surfaces and interfaces’, *Surf. Sci.*, vol. 132, no. 1, pp. 406–421, Sep. 1983, doi: 10.1016/0039-6028(83)90550-2.

[70] P. A. Wolff, ‘Theory of Electron Multiplication in Silicon and Germanium’, *Phys. Rev.*, vol. 95, no. 6, pp. 1415–1420, Sep. 1954, doi: 10.1103/PhysRev.95.1415.

[71] C. L. Anderson and C. R. Crowell, ‘Threshold Energies for Electron-Hole Pair Production by Impact Ionization in Semiconductors’, *Phys. Rev. B*, vol. 5, no. 6, pp. 2267–2272, Mar. 1972, doi: 10.1103/PhysRevB.5.2267.

[72] J. S. Cheong, M. M. Hayat, X. Zhou, and J. P. R. David, ‘Relating the Experimental Ionization Coefficients in Semiconductors to the Nonlocal Ionization Coefficients’, *IEEE Trans. Electron Devices*, vol. 62, no. 6, pp. 1946–1952, Jun. 2015, doi: 10.1109/TED.2015.2422789.

[73] K. F. Li *et al.*, ‘Low excess noise characteristics in thin avalanche region GaAs diodes’, *Electron. Lett.*, vol. 34, no. 1, pp. 125–126, Jan. 1998, doi: 10.1049/el:19980021.

[74] C. Tan *et al.*, ‘Avalanche noise measurement in thin Si p+-i-n+ diodes’, *Appl. Phys. Lett. - APPL PHYS LETT*, vol. 76, Jun. 2000, doi: 10.1063/1.126823.

[75] A. R. J. Marshall, P. J. Ker, A. Krysa, J. P. R. David, and C. H. Tan, ‘High speed InAs electron avalanche photodiodes overcome the conventional gain-bandwidth product limit’, *Opt. Express*, vol. 19, no. 23, pp. 23341–23349, Nov. 2011, doi: 10.1364/OE.19.023341.

[76] M. H. Woods, W. C. Johnson, and M. A. Lampert, ‘Use of a Schottky barrier to measure impact ionization coefficients in semiconductors’, *Solid-State Electron.*, vol. 16, no. 3, pp. 381–394, Mar. 1973, doi: 10.1016/0038-1101(73)90013-0.

[77] G. E. Stillman and C. M. Wolfe, ‘Chapter 5: Avalanche Photodiodes’, in *Semiconductors and Semimetals*, vol. 12, R. K. Willardson and A. C. Beer, Eds. Elsevier, 1977, pp. 291–393. doi: 10.1016/S0080-8784(08)60150-7.

[78] W. N. Grant, ‘Electron and hole ionization rates in epitaxial silicon at high electric fields’, *Solid-State Electron.*, vol. 16, no. 10, pp. 1189–1203, Oct. 1973, doi: 10.1016/0038-1101(73)90147-0.

[79] R. J. McIntyre, ‘A new look at impact ionization-Part I: A theory of gain, noise, breakdown probability, and frequency response’, *IEEE Trans. Electron Devices*, vol. 46, no. 8, pp. 1623–1631, Aug. 1999, doi: 10.1109/16.777150.

[80] D. S. Ong, K. F. Li, S. A. Plimmer, G. J. Rees, J. P. R. David, and P. N. Robson, ‘Full band Monte Carlo modeling of impact ionization, avalanche multiplication, and noise in submicron GaAs p+-i-n+ diodes’, *J. Appl. Phys.*, vol. 87, no. 11, pp. 7885–7891, Jun. 2000, doi: 10.1063/1.373472.

[81] C. Hu, K. A. Anselm, B. G. Streetman, and J. C. Campbell, ‘Noise characteristics of thin multiplication region GaAs avalanche photodiodes’, *Appl. Phys. Lett.*, vol. 69, no. 24, pp. 3734–3736, Dec. 1996, doi: 10.1063/1.117205.

[82] J. C. Campbell, ‘Low-noise, high-speed avalanche photodiodes’, in *Optical Fiber Communication Conference and Exhibit*, Mar. 2002, pp. 270–271. doi: 10.1109/OFC.2002.1036354.

[83] M. M. Hayat, B. E. A. Saleh, and M. C. Teich, ‘Effect of dead space on gain and noise of double-carrier-multiplication avalanche photodiodes’, *IEEE Trans. Electron Devices*, vol. 39, no. 3, pp. 546–552, Mar. 1992, doi: 10.1109/16.123476.

[84] M. M. Hayat, W. L. Sargeant, and B. E. A. Saleh, ‘Effect of dead space on gain and noise in Si and GaAs avalanche photodiodes’, *IEEE J. Quantum Electron.*, vol. 28, no. 5, pp. 1360–1365, May 1992, doi: 10.1109/3.135278.

[85] D. S. Ong, K. F. Li, G. J. Rees, J. P. R. David, and P. N. Robson, ‘A simple model to determine multiplication and noise in avalanche photodiodes’, *J. Appl. Phys.*, vol. 83, no. 6, pp. 3426–3428, Mar. 1998, doi: 10.1063/1.367111.

[86] M. V. Fischetti and S. E. Laux, ‘Monte carlo analysis of electron transport in small semiconductor devices including band-structure and space-charge effects’, *Phys. Rev. B*, vol. 38, no. 14, pp. 9721–9745, Nov. 1988, doi: 10.1103/PhysRevB.38.9721.

[87] H. K. Jung, K. Taniguchi, and C. Hamaguchi, ‘Impact ionization model for full band Monte Carlo simulation in GaAs’, *J. Appl. Phys.*, vol. 79, no. 5, pp. 2473–2480, Mar. 1996, doi: 10.1063/1.361176.

[88] M. V. Fischetti and S. E. Laux, ‘Monte Carlo simulation of transport in technologically significant semiconductors of the diamond and zinc-blende structures. II. Submicrometer MOSFET’s’, *IEEE Trans. Electron Devices*, vol. 38, no. 3, pp. 650–660, Mar. 1991, doi: 10.1109/16.75177.

[89] T. Brudevoll, B. Lund, and T. A. Fjeldly, ‘Warm and hot hole drift velocity in GaAs studied by Monte Carlo simulation’, *J. Appl. Phys.*, vol. 71, no. 10, pp. 4972–4976, May 1992, doi: 10.1063/1.350595.

[90] S. A. Plimmer, J. P. R. David, D. S. Ong, and K. F. Li, ‘A simple model for avalanche multiplication including deadspace effects’, *IEEE Trans. Electron Devices*, vol. 46, no. 4, pp. 769–775, Apr. 1999, doi: 10.1109/16.753712.

[91] J. Petticrew, S. Dimler, and J. S. Ng, ‘Simple Monte Carlo Simulator for Modelling Linear Mode and Geiger Mode Avalanche Photodiodes in C++’, *J. Open Res. Softw.*, vol. 6, no. 1, Art. no. 1, May 2018, doi: 10.5334/jors.212.

[92] J. D. Taylor-Mew, J. D. Petticrew, C. H. Tan, and J. S. Ng, ‘Simulation of $Al_{0.85}Ga_{0.15}As_{0.56}Sb_{0.44}$ avalanche photodiodes’, *Opt. Express*, vol. 30, no. 11, pp. 17946–17952, May 2022, doi: 10.1364/OE.458922.

[93] S. C. L. T. Mun, C. H. Tan, Y. L. Goh, A. R. J. Marshall, and J. P. R. David, ‘Modeling of avalanche multiplication and excess noise factor in In0.52Al0.48As avalanche photodiodes using a simple Monte Carlo model’, *J. Appl. Phys.*, vol. 104, no. 1, p. 013114, Jul. 2008, doi: 10.1063/1.2952003.

[94] X. Zhou, J. S. Ng, and C. H. Tan, ‘A simple Monte Carlo model for prediction of avalanche multiplication process in Silicon’, *J. Instrum.*, vol. 7, no. 08, pp. P08006–P08006, Aug. 2012, doi: 10.1088/1748-0221/7/08/P08006.

[95] C. H. Tan, R. Ghin, J. P. R. David, G. J. Rees, and M. Hopkinson, ‘The effect of dead space on gain and excess noise in In0.48Ga0.52P p in diodes’, *Semicond. Sci. Technol.*, vol. 18, no. 8, pp. 803–806, Jul. 2003, doi: 10.1088/0268-1242/18/8/314.

[96] W. Shockley, ‘The theory of p-n junctions in semiconductors and p-n junction transistors’, *Bell Syst. Tech. J.*, vol. 28, no. 3, pp. 435–489, Jul. 1949, doi: 10.1002/j.1538-7305.1949.tb03645.x.

[97] E. O. Kane, ‘Zener tunneling in semiconductors’, *J. Phys. Chem. Solids*, vol. 12, no. 2, pp. 181–188, Jan. 1960, doi: 10.1016/0022-3697(60)90035-4.

[98] S. R. Forrest, R. F. Leheny, R. E. Nahory, and M. A. Pollack, ‘In0.53Ga0.47As photodiodes with dark current limited by generation-recombination and tunneling’, *Appl. Phys. Lett.*, vol. 37, no. 3, pp. 322–325, Aug. 1980, doi: 10.1063/1.91922.

[99] ‘Tunnel Devices’, in *Physics of Semiconductor Devices*, John Wiley & Sons, Ltd, 2006, pp. 415–465. doi: 10.1002/9780470068328.ch8.

[100] C. Groves, R. Ghin, J. P. R. David, and G. J. Rees, ‘Temperature dependence of impact ionization in GaAs’, *IEEE Trans. Electron Devices*, vol. 50, no. 10, pp. 2027–2031, Oct. 2003, doi: 10.1109/TED.2003.816918.

[101] Y. P. Varshni, ‘Temperature dependence of the energy gap in semiconductors’, *Physica*, vol. 34, no. 1, pp. 149–154, Jan. 1967, doi: 10.1016/0031-8914(67)90062-6.

[102] C. H. Tan, G. J. Rees, P. A. Houston, J. S. Ng, W. K. Ng, and J. P. R. David, ‘Temperature dependence of electron impact ionization in In0.53Ga0.47As’, *Appl. Phys. Lett.*, vol. 84, no. 13, pp. 2322–2324, Mar. 2004, doi: 10.1063/1.1691192.

[103] I. C. Sandall, J. S. Ng, S. Xie, P. J. Ker, and C. H. Tan, ‘Temperature dependence of impact ionization in InAs’, *Opt. Express*, vol. 21, no. 7, pp. 8630–8637, Apr. 2013, doi: 10.1364/OE.21.008630.

[104] J. S. L. Ong, J. S. Ng, A. B. Krysa, and J. P. R. David, ‘Temperature dependence of avalanche multiplication and breakdown voltage in Al0.52In0.48P’, *J. Appl. Phys.*, vol. 115, no. 6, p. 064507, Feb. 2014, doi: 10.1063/1.4865743.

[105] F. Ma, G. Karve, X. Zheng, X. Sun, A. L. Holmes, and J. C. Campbell, ‘Low-temperature breakdown properties of AlxGa1−xAs avalanche photodiodes’, *Appl. Phys. Lett.*, vol. 81, no. 10, pp. 1908–1910, Sep. 2002, doi: 10.1063/1.1506012.

[106] X. Jin *et al.*, ‘Temperature Dependence of the Impact Ionization Coefficients in AlAsSb Lattice Matched to InP’, *IEEE J. Sel. Top. Quantum Electron.*, vol. 28, no. 2, pp. 1–8, Mar. 2022, doi: 10.1109/JSTQE.2021.3099912.

[107] L. Tirino, M. Weber, K. F. Brennan, E. Bellotti, and M. Goano, ‘Temperature dependence of the impact ionization coefficients in GaAs, cubic SiC, and zinc-blende GaN’, *J. Appl. Phys.*, vol. 94, no. 1, pp. 423–430, Jul. 2003, doi: 10.1063/1.1579129.

[108] R. E. Neidert, ‘Dielectric constant of semi-insulating gallium arsenide’, *Electron. Lett.*, vol. 16, p. 244, Mar. 1980, doi: 10.1049/el:19800180.

[109] A. S. Grove, *Physics and Technology of Semiconductor Devices (Wiley International Edition)*. New York: Wiley, 1967. Accessed: May 16, 2022. [Online]. Available: https://www.biblio.com/book/physics-technology-semiconductor-devices-wiley-international/d/1395635890

[110] Kim Foung Li, ‘Avalanche noise in submicron GaAs in InP structures’, University of Sheffield, Sheffield, United Kingdom, 1999.

[111] K. S. Lau *et al.*, ‘Excess noise measurement in avalanche photodiodes using a transimpedance amplifier front-end’, *Meas. Sci. Technol.*, vol. 17, no. 7, pp. 1941–1946, Jun. 2006, doi: 10.1088/0957-0233/17/7/036.

[112] Analog Devices, ‘Analog Devices Ultralow Distortion, Wide Bandwidth Voltage Feedback Op Amps: AD9631/AD9632 Rev. D’. 2014.

[113] L. Qiao, S. J. Dimler, A. N. A. P. Baharuddin, J. E. Green, and J. P. R. David, ‘An excess noise measurement system for weak responsivity avalanche photodiodes’, *Meas. Sci. Technol.*, vol. 29, no. 6, p. 065015, May 2018, doi: 10.1088/1361-6501/aabc8b.

[114] J. S. L. Ong, 'Impact Ionisation in AlInP Photodiodes', University of Sheffield, Sheffield, United Kingdom, 2012.

[115] J. A. J. Allam, '"Universal" Dependence of Avalanche Breakdown on Bandstructure: Choosing Materials for High-Power Devices', *Jpn. J. Appl. Phys.*, vol. 36, no. 3S, p. 1529, Mar. 1997, doi: 10.1143/JJAP.36.1529.

[116] S. Adachi, *Properties of Semiconductor Alloys: Group-IV, III-V and II-VI Semiconductors*. John Wiley & Sons, 2009.

[117] J. S. Cheong, A. N. A. P. Baharuddin, J. S. Ng, A. B. Krysa, and J. P. R. David, 'Absorption coefficients in AlGaInP lattice-matched to GaAs', *Sol. Energy Mater. Sol. Cells*, vol. 164, pp. 28–31, May 2017, doi: 10.1016/j.solmat.2017.01.042.

[118] K. Streubel, N. Linder, R. Wirth, and A. Jaeger, 'High brightness AlGaInP light-emitting diodes', *IEEE J. Sel. Top. Quantum Electron.*, vol. 8, no. 2, pp. 321–332, Mar. 2002, doi: 10.1109/2944.999187.

[119] M. Yamaguchi, T. Takamoto, and K. Araki, 'Super high-efficiency multi-junction and concentrator solar cells', *Sol. Energy Mater. Sol. Cells*, vol. 90, no. 18, pp. 3068–3077, Nov. 2006, doi: 10.1016/j.solmat.2006.06.028.

[120] O. Breitenstein *et al.*, 'Understanding junction breakdown in multicrystalline solar cells', Mar. 2010. *Proceedings 20th Workshop on Crystalline SiliconSolar Cells & Modules*, p. 1 - 13 NREL,Breckenridge, USA (2010)

[121] J. S. Cheong, J. S. L. Ong, J. S. Ng, A. B. Krysa, and J. P. R. David, 'Al0.52In0.48P SAM-APD as a Blue-Green Detector', *IEEE J. Sel. Top. Quantum Electron.*, vol. 20, no. 6, pp. 142–146, Nov. 2014, doi: 10.1109/JSTQE.2014.2316601.

[122] S. Zhao, S. Butera, G. Lioliou, A. B. Krysa, and A. M. Barnett, 'AlInP photodiode x-ray detectors', *J. Phys. Appl. Phys.*, vol. 52, no. 22, p. 225101, May 2019, doi: 10.1088/1361-6463/ab0d65.

[123] C. Groves, C. N. Harrison, J. P. R. David, and G. J. Rees, 'Temperature dependence of breakdown voltage in AlxGa1−xAs', *J. Appl. Phys.*, vol. 96, no. 9, pp. 5017–5019, Oct. 2004, doi: 10.1063/1.1803944.

[124] D. Ji, B. Ercan, G. Benson, A. K. M. Newaz, and S. Chowdhury, '60 A/W high voltage GaN avalanche photodiode demonstrating robust avalanche and high gain up to 525 K', *Appl. Phys. Lett.*, vol. 116, no. 21, p. 211102, May 2020, doi: 10.1063/1.5140005.

[125] P. Lechner *et al.*, 'Silicon drift detectors for high resolution room temperature X-ray spectroscopy', *Nucl. Instrum. Methods Phys. Res. Sect. Accel. Spectrometers Detect. Assoc. Equip.*, vol. 377, no. 2, pp. 346–351, Aug. 1996, doi: 10.1016/0168-9002(96)00210-0.

[126] W. K. Loke *et al.*, 'GaNAsSb/GaAs waveguide photodetector with response up to 1.6 μm grown by molecular beam epitaxy', *Appl. Phys. Lett.*, vol. 93, no. 8, p. 081102, Aug. 2008, doi: 10.1063/1.2976124.

[127] A. R. J. Marshall, A. P. Craig, C. J. Reyner, and D. L. Huffaker, 'GaAs and AlGaAs APDs with GaSb absorption regions in a separate absorption and multiplication structure using a hetero-lattice interface', *Infrared Phys. Technol.*, vol. 70, pp. 168–170, May 2015, doi: 10.1016/j.infrared.2014.08.014.

[128] L. Qiao *et al.*, 'Avalanche Noise in Al0.52In0.48P Diodes', *IEEE Photonics Technol. Lett.*, vol. 28, no. 4, pp. 481–484, Feb. 2016, doi: 10.1109/LPT.2015.2499545.

[129] D. Pasquariello, M. Camacho, K. Hjort, L. Dózsa, and B. Szentpáli, ‘Evaluation of InP-to-silicon heterobonding’, *Mater. Sci. Eng. B*, vol. 80, no. 1, pp. 134–137, Mar. 2001, doi: 10.1016/S0921-5107(00)00626-7.

[130] C. A. Tran, R. A. Masut, P. Cova, J. L. Brebner, and R. Leonelli, ‘Growth and characterization of InP on silicon by MOCVD’, *J. Cryst. Growth*, vol. 121, no. 3, pp. 365–372, Jul. 1992, doi: 10.1016/0022-0248(92)90146-A.

[131] P. A. Postigo, F. Suárez, A. Sanz-Hervás, J. Sangrador, and C. G. Fonstad, ‘Growth of InP on GaAs (001) by hydrogen-assisted low-temperature solid-source molecular beam epitaxy’, *J. Appl. Phys.*, vol. 103, no. 1, p. 013508, Jan. 2008, doi: 10.1063/1.2824967.

[132] M. Kondo, N. Okada, K. Domen, K. Sugiura, C. Anayama, and T. Tanahashi, ‘Origin of nonradiative recombination centers in AlGaInP grown by metalorganic vapor phase epitaxy’, *J. Electron. Mater.*, vol. 23, no. 3, pp. 355–358, Mar. 1994, doi: 10.1007/BF03296064.

[133] Y. Nishikawa, M. Suzuki, and M. Okajima, ‘Effects of Growth Parameters on Oxygen Incorporation into InGaAlP Grown by Metalorganic Chemical Vapor Deposition’, *Jpn. J. Appl. Phys.*, vol. 32, no. 1S, p. 498, Jan. 1993, doi: 10.1143/JJAP.32.498.

[134] R. France, M. A. Steiner, T. G. Deutsch, E. A. Brucker, C.-S. Jiang, and A. G. Norman, ‘Oxidation and characterization of AlInP under light-soaked, damp heat conditions’, in *2010 35th IEEE Photovoltaic Specialists Conference*, Jun. 2010, pp. 002016–002020. doi: 10.1109/PVSC.2010.5616977.

[135] J. S. L. Ong, J. S. Ng, A. B. Krysa, and J. P. R. David, ‘Impact Ionization Coefficients in Al0.52In0.48P’, *IEEE Electron Device Lett.*, vol. 32, no. 11, pp. 1528–1530, Nov. 2011, doi: 10.1109/LED.2011.2165520.

[136] S. -L. Fu, T. P. Chin, M. C. Ho, C. W. Tu, and P. M. Asbeck, ‘Impact ionization coefficients in (100) GaInP’, *Appl. Phys. Lett.*, vol. 66, no. 25, pp. 3507–3509, Jun. 1995, doi: 10.1063/1.113779.

[137] R. Ghin, J. P. R. David, M. Hopkinson, M. A. Pate, G. J. Rees, and P. N. Robson, ‘Impact ionization coefficients in GaInP p–i–n diodes’, *Appl. Phys. Lett.*, vol. 70, no. 26, pp. 3567–3569, Jun. 1997, doi: 10.1063/1.119235.

[138] R. Ghin *et al.*, ‘Avalanche multiplication and breakdown in Ga/sub 0.52/In/sub 0.48/P diodes’, *IEEE Trans. Electron Devices*, vol. 45, no. 10, pp. 2096–2101, Oct. 1998, doi: 10.1109/16.725241.

[139] J. P. R. David, R. Ghin, S. A. Plimmer, M. Hopkinson, and J. Allam, ‘Breakdown characteristics of (Al/sub X/Ga/sub 1-X/)/sub 0.52/In/sub 0.48/P p-i-n diodes’, in *ICSE ’96. 1996 IEEE International Conference on Semiconductor Electronics. Proceedings*, Nov. 1996, pp. 256–260. doi: 10.1109/SMELEC.1996.616493.

[140] D. J. Lockwood, G. Yu, and N. L. Rowell, ‘Optical phonon frequencies and damping in AlAs, GaP, GaAs, InP, InAs and InSb studied by oblique incidence infrared spectroscopy’, *Solid State Commun.*, vol. 136, no. 7, pp. 404–409, Nov. 2005, doi: 10.1016/j.ssc.2005.08.030.

[141] L. G. Meiners, ‘Temperature dependence of the dielectric constant of InP’, *J. Appl. Phys.*, vol. 59, no. 5, pp. 1611–1613, Mar. 1986, doi: 10.1063/1.336472.

[142] B. Monemar, ‘Determination of band gap and refractive index of AIP from optical absorption’, *Solid State Commun.*, vol. 8, no. 16, pp. 1295–1298, Aug. 1970, doi: 10.1016/0038-1098(70)90623-X.

[143] K. A. Bertness, S. R. Kurtz, S. E. Asher, and R. C. Reedy, ‘AlInP benchmarks for growth of AlGaInP compounds by organometallic vapor-phase epitaxy’, *J. Cryst. Growth*, vol. 196, no. 1, pp. 13–22, Jan. 1999, doi: 10.1016/S0022-0248(98)00751-9.

[144] L. Qiao, ‘Methodologies for low excess noise measurement in wide bandgap materials’, University of Sheffield, Sheffield, United Kingdom, 2017.

[145] B. K. Ng, J. P. R. David, S. A. Plimmer, M. Hopkinson, R. C. Tozer, and G. J. Rees, ‘Impact ionization coefficients of Al0.8Ga0.2As’, *Appl. Phys. Lett.*, vol. 77, no. 26, pp. 4374–4376, Dec. 2000, doi: 10.1063/1.1336556.

[146] J. S. Cheong, J. S. Ng, A. B. Krysa, J. S. L. Ong, and J. P. R. David, ‘Determination of absorption coefficients in AlInP lattice matched to GaAs’, *J. Phys. Appl. Phys.*, vol. 48, no. 40, p. 405101, Sep. 2015, doi: 10.1088/0022-3727/48/40/405101.

[147] B. K. Ng, ‘Impact Ionization in Wide Band Gap Semiconductors: AlxGa1-xAs and 4H-SiC’, University of Sheffield, Sheffield, United Kingdom, 2002.

[148] S. A. Plimmer, J. P. R. David, G. J. Rees, and P. N. Robson, ‘Ionization coefficients in AlxGa1-xAs (x= 0 - 0.60)’, *Semicond. Sci. Technol.*, vol. 15, no. 7, pp. 692–699, Jun. 2000, doi: 10.1088/0268-1242/15/7/307.

[149] K. Brennan and K. Hess, ‘Theory of high-field transport of holes in GaAs and InP’, *Phys. Rev. B*, vol. 29, no. 10, pp. 5581–5590, May 1984, doi: 10.1103/PhysRevB.29.5581.

[150] S. Lee *et al.*, ‘Low noise Al0.85Ga0.15As0.56Sb0.44 avalanche photodiodes on InP substrates’, *Appl. Phys. Lett.*, vol. 118, no. 8, p. 081106, Feb. 2021, doi: 10.1063/5.0035571.

[151] J. Taylor-Mew, V. Shulyak, B. White, C. H. Tan, and J. S. Ng, ‘Low Excess Noise of Al0.85Ga0.15As0.56Sb0.44 Avalanche Photodiode From Pure Electron Injection’, *IEEE Photonics Technol. Lett.*, vol. 33, no. 20, pp. 1155–1158, Oct. 2021, doi: 10.1109/LPT.2021.3110123.

[152] L. L. G. Pinel *et al.*, ‘Effects of carrier injection profile on low noise thin $Al_{0.85}Ga_{0.15}As_{0.56}Sb_{0.44}$ avalanche photodiodes’, *Opt. Express*, vol. 26, no. 3, pp. 3568–3576, Feb. 2018, doi: 10.1364/OE.26.003568.

[153] S. Xie and C. H. Tan, ‘AlAsSb Avalanche Photodiodes With a Sub-mV/K Temperature Coefficient of Breakdown Voltage’, *IEEE J. Quantum Electron.*, vol. 47, no. 11, pp. 1391–1395, Nov. 2011, doi: 10.1109/JQE.2011.2165051.

[154] J. Xie, S. Xie, R. C. Tozer, and C. H. Tan, ‘Excess Noise Characteristics of Thin AlAsSb APDs’, *IEEE Trans. Electron Devices*, vol. 59, no. 5, pp. 1475–1479, May 2012, doi: 10.1109/TED.2012.2187211.

[155] X. Zhou, S. Zhang, J. P. R. David, J. S. Ng, and C. H. Tan, ‘Avalanche Breakdown Characteristics of Al1–xGaxAs0.56Sb0.44 Quaternary Alloys’, *IEEE Photonics Technol. Lett.*, vol. 28, no. 22, pp. 2495–2498, Nov. 2016, doi: 10.1109/LPT.2016.2601651.

[156] X. Zhou, L. L. G. Pinel, S. J. Dimler, S. Zhang, J. S. Ng, and C. H. Tan, ‘Thin $Al_xGa_{1-x}As_{0.56}Sb_{0.44}$ Diodes With Low Excess Noise’, *IEEE J. Sel. Top. Quantum Electron.*, vol. 24, no. 2, pp. 1–5, Mar. 2018, doi: 10.1109/JSTQE.2017.2725441.

[157] X. Zhou, S. Xie, S. Zhang, J. S. Ng, and C. H. Tan, ‘InGaAs/AlGaAsSb APD with over 200 GHz gain-bandwidth product’, in *2016 Compound Semiconductor Week (CSW) [Includes 28th International Conference on Indium Phosphide Related Materials (IPRM) 43rd International Symposium on Compound Semiconductors (ISCS)*, Jun. 2016, pp. 1–2. doi: 10.1109/ICIPRM.2016.7528782.

[158] B. Guo *et al.*, ‘Optical constants of Al0.85Ga0.15As0.56Sb0.44 and Al0.79In0.21As0.74Sb0.26’, *Appl. Phys. Lett.*, vol. 119, no. 17, p. 171109, Oct. 2021, doi: 10.1063/5.0062035.

[159] S. Lee *et al.*, ‘Random alloy thick AlGaAsSb avalanche photodiodes on InP substrates’, *Appl. Phys. Lett.*, vol. 120, no. 7, p. 071101, Feb. 2022, doi: 10.1063/5.0067408.

[160] K. Onabe, ‘Unstable Regions in Type A1-x-yBxCyD III-V Quaternary Solid Solutions Calculated with Strictly Regular Solution Approximation’, *Jpn. J. Appl. Phys.*, vol. 22, no. 2R, p. 287, Feb. 1983, doi: 10.1143/JJAP.22.287.

[161] J. R. Pessetto and G. B. Stringfellow, ‘AlxGa1−xAsySb1−y phase diagram’, *J. Cryst. Growth*, vol. 62, no. 1, pp. 1–6, Jun. 1983, doi: 10.1016/0022-0248(83)90002-7.

[162] M. Losurdo, P. Capezzuto, G. Bruno, A. S. Brown, T. Brown, and G. May, ‘Fundamental reactions controlling anion exchange during mixed anion heterojunction formation: Chemistry of As-for-Sb and Sb-for-As exchange reactions’, *J. Appl. Phys.*, vol. 100, no. 1, p. 013531, Jul. 2006, doi: 10.1063/1.2216049.

[163] Y. Hu, M. C. Tam, and Z. R. Wasilewski, ‘Unintentional As incorporation into AlSb and interfacial layers within InAs/AlSb superlattices’, *J. Vac. Sci. Technol. B*, vol. 37, no. 3, p. 032902, May 2019, doi: 10.1116/1.5088974.

[164] S. Lee *et al.*, ‘Investigation of carrier localization in InAs/AlSb type-II superlattice material system’, *Appl. Phys. Lett.*, vol. 115, no. 21, p. 211601, Nov. 2019, doi: 10.1063/1.5127198.

[165] S. Tomasulo *et al.*, ‘Effect of molecular beam epitaxy growth conditions on phase separation in wide-bandgap InAlAsSb lattice-matched to InP’, *J. Cryst. Growth*, vol. 548, p. 125826, Oct. 2020, doi: 10.1016/j.jcrysgro.2020.125826.

[166] A. G. Chynoweth, ‘Ionization Rates for Electrons and Holes in Silicon’, *Phys. Rev.*, vol. 109, no. 5, pp. 1537–1540, Mar. 1958, doi: 10.1103/PhysRev.109.1537.

[167] Y. L. Goh *et al.*, ‘Avalanche Multiplication in InAlAs’, *IEEE Trans. Electron Devices*, vol. 54, no. 1, pp. 11–16, Jan. 2007, doi: 10.1109/TED.2006.887229.

[168] S. Ramo, ‘Currents Induced by Electron Motion’, *Proc. IRE*, vol. 27, no. 9, pp. 584–585, Sep. 1939, doi: 10.1109/JRPROC.1939.228757.

[169] Y. Yuan *et al.*, ‘Temperature dependence of the ionization coefficients of InAlAs and AlGaAs digital alloys’, *Photonics Res.*, vol. 6, no. 8, pp. 794–799, Aug. 2018, doi: 10.1364/PRJ.6.000794.

[170] Z. Deng *et al.*, ‘Optical properties of beryllium-doped GaSb epilayers grown on GaAs substrate’, *Infrared Phys. Technol.*, vol. 90, pp. 115–121, May 2018, doi: 10.1016/j.infrared.2018.03.004.

Appendix I: Modelling of device region widths and dopings from capacitance-voltage characteristics

This appendix describes the method used to extract the region widths and dopings of a three-region PIN or NIP diode structure from the capacitance-voltage characteristics. This method approximates the depletion width as related to the device capacitance by equation I.1:

$$C = \frac{\varepsilon_0 \varepsilon_r A_D}{W_T} \quad \text{(I.1)}$$

Where ε_0 is the permittivity of free space, ε_r is the relative permittivity of the semiconductor material, A_D is the area of the diode, and W_T is the depletion width. This method also assumes that the doping in each region is uniform and that the junctions between them are abrupt.

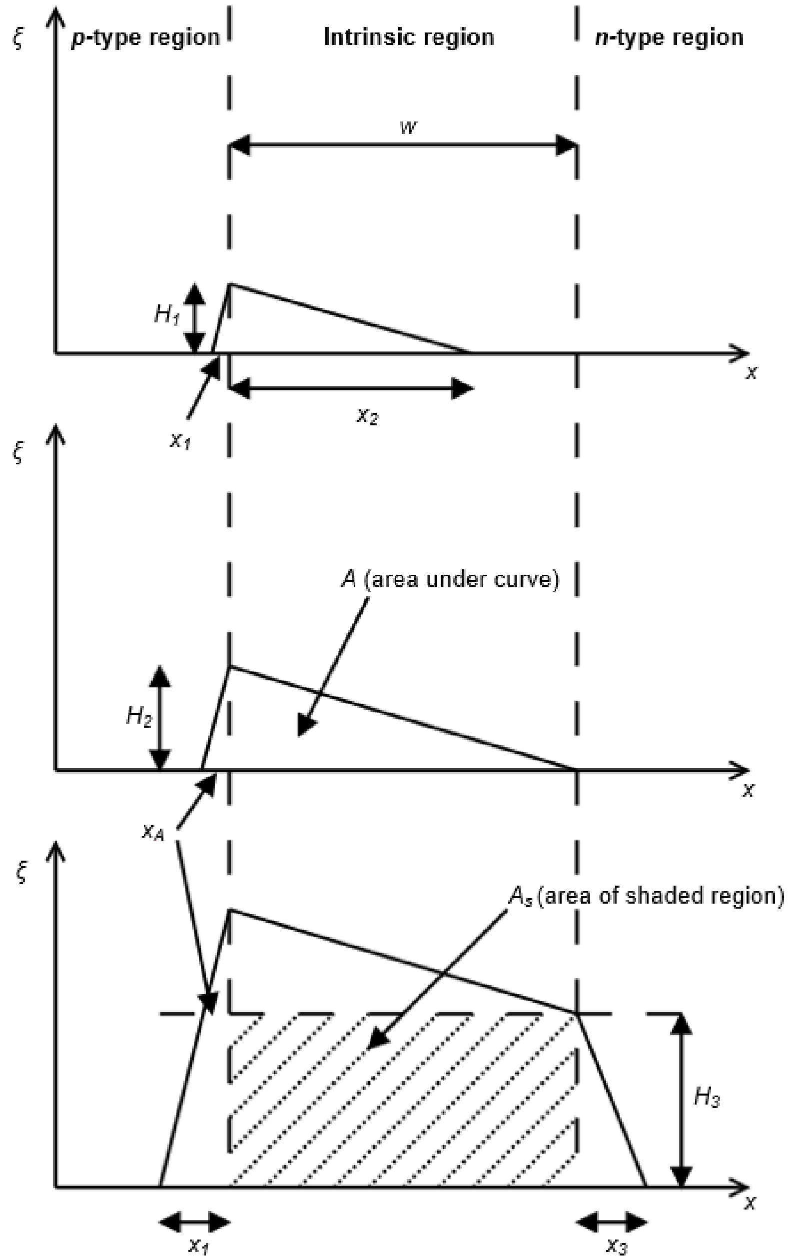

Figure I.1: Diagram showing electric field profiles for a PIN device at varying stages of depletion

The electric field gradient in each region can be calculated using Poisson's equation and is given in equations I.2, I.3, and I.4 for the *p*-type, intrinsic, and *n*-type regions respectively. The background doping in the intrinsic regions is here considered to be *n*-type.

$$G_p = \left(\frac{d\xi}{dx}\right)_p = \frac{qN_p}{\varepsilon_0 \varepsilon_r} \text{ (I.2)}$$

$$G_i = \left(\frac{d\xi}{dx}\right)_i = \frac{qN_i}{\varepsilon_0 \varepsilon_r} \text{ (I.3)}$$

$$G_n = \left(\frac{d\xi}{dx}\right)_n = \frac{qN_n}{\varepsilon_0 \varepsilon_r} \text{ (I.4)}$$

Where N_p, N_i, and N_n are the dopings in the *p*-type, intrinsic, and *n*-type regions respectively and q is the electronic charge.

In the presence of an electric field across the device one of three cases will occur depending on its magnitude: the intrinsic region can be partially depleted, fully depleted but with no further depletion into the *n*-type cladding, or fully depleted with further depletion into the *n*-type cladding. For an applied reverse bias voltage of V_a, the total reverse bias voltage across the device is given by equation I.5:

$$V_T = V_a + V_{bi} \text{ (I.5)}$$

Where V_{bi} is the built-in voltage of the device.

Figure I.1 shows electric field profiles for a PIN device at each of the above stages of depletion. At the minimum bias voltage for which the intrinsic region is fully depleted, the area under the electric field profile is A, which is given by equation I.6:

$$A = 0.5H_2(x_A + w) \text{ (I.6)}$$

Where w is the width of the intrinsic region, $H_2 = wG_i$ and $x_A = \frac{H_2}{G_p}$. These expressions can be substituted to give equation I.7:

$$A = 0.5wG_i\left(w\frac{G_i}{G_p} + w\right) = 0.5w^2G_i\left(\frac{G_i}{G_p} + 1\right) \text{ (I.7)}$$

For $V_T \leq A$, there is depletion in the *p*-type and intrinsic regions only and the total deletion width, W_T, is given by equation I.8:

$$W_T = x_1 + x_2 \quad \text{(I.8)}$$

Where x_1 is the width of the depletion in the p-type region and x_2 is the width of the depletion in the intrinsic region. In this case V_T is given by equation I.9:

$$V_T = 0.5H_1(x_1 + x_2) \quad \text{(I.9)}$$

Where $H_1 = x_1G_p = x_2G_i$. Rearrangement and substitution gives equations I.10 and I.11:

$$x_1 = \sqrt{\frac{2V_T}{G_p\left(1+\frac{G_p}{G_i}\right)}} \quad \text{(I.10)}$$

$$x_2 = x_1\frac{G_p}{G_i} \quad \text{(I.11)}$$

For $V_T > A$, there is depletion in all three regions of the device. The area of the region labelled A_s in figure I.1 is given by equation I.12:

$$A_s = V_T - A = 0.5H_3(2w + x_1 + x_3 + x_A) \quad \text{(I.12)}$$

Where $x_1 = \frac{H_3}{G_p} + x_A$ is the depletion into the p-type region, x_A is the depletion into the p-type layer at the minimum bias voltage for which the intrinsic region is fully depleted, and $x_3 = \frac{H_3}{G_n}$ is the depletion into the n-type region. Substitution gives equation I.13:

$$0.5\left(\frac{1}{G_p} + \frac{1}{G_n}\right){H_3}^2 + (w + x_A)H_3 + (A - V_T) = 0 \quad \text{(I.13)}$$

The quadratic formula, which in this case has one solution only as H_3 cannot be negative, is applied to give equation I.14:

$$H_3 = \frac{-(w+x_A)+\sqrt{(w+x_A)^2+2\left(\frac{1}{G_p}+\frac{1}{G_n}\right)(V_T-A)}}{\left(\frac{1}{G_p}+\frac{1}{G_n}\right)} \quad \text{(I.14)}$$

The total depletion width in the device is therefore given by equation I.15:

$$W_T = w + x_A + H_3\left(\frac{1}{G_p} + \frac{1}{G_n}\right) \quad \text{(I.15)}$$

Projected region widths and dopings are used to calculate the depletion width in a structure as a function of reverse bias voltage using these equations. This can be used to calculate simulated capacitance-voltage data, which is compared to measured data to find the actual region widths and dopings of the structure.